Small Molecule Modulators of β-arrestins

Alem W. Kahsai[1,#,*], Natalia Pakharukova[1,#], Henry Y. Kwon[1,7], Kunal S. Shah[1,5,8], Jason G. Liang-Lin[1], Caroline T. del Real[1], Paul J. Shim[1.9,10], Mason A. Lee[1], Van A. Ngo[11], Bowie N. Shreiber[1], Samuel Liu[1], Allison M. Schwalb[1,5], Emmanuel F. Espinoza[12], Brittany N. Thomas[1], Cal A. Kunzle[1], Jeffrey S. Smith[1,10,13], Jialu Wang[1,3], Jihee Kim[1], Xingdong Zhang[1], Howard A. Rockman[1,3], Alex R. B. Thomsen[12], Lindsay A.M. Rein[1], Lei Shi[14], Seungkirl Ahn[1], Ali Masoudi[1], Robert J. Lefkowitz[1,2,4,6,15,*]

Departments of [1]Medicine, [2]Biochemistry, [3]Cell Biology, and [4]Chemistry, and [5]Duke University School of Medicine and the [6]Howard Hughes Medical Institute, Duke University Medical Center, Durham, NC, 27710, USA.

[7] Department of Surgery, Henry Ford Hospital, Detroit, MI, 48202, USA.

[8]Cedars-Sinai Medical Center, Internal Medicine, Los Angeles, CA 90048, USA.

[9]Department of Medicine, Beth Israel Deaconess Medical Center, Boston, MA 02215, USA.

[10]Harvard Medical School, Boston, MA, 02115, USA.

[11]U.S. Department of Energy, National Center for Computational Sciences, Oak Ridge National Laboratory, Oak Ridge, TN 37830, USA.

[12]Department of Molecular Pathobiology, New York University School of Dentistry, New York, NY, 10010, USA.

[13]Department of Dermatology, Massachusetts General Hospital, Boston, MA, 02114,

[14]Computational Chemistry and Molecular Biophysics Section, Molecular Targets and Medications Discovery Branch, National Institute on Drug Abuse – Intramural Research Program, National Institutes of Health, Baltimore, MD 21224, USA.

[#] These authors contributed equally to this work.

[15]Lead contact

*Correspondence: lefko001@receptor-biol.duke.edu (R.J.L.), alem@receptor-biol.duke.edu (A.W.K.)

Summary

β-arrestins (βarrs) are key regulators of G protein-coupled receptors (GPCRs), essential for modulating signaling pathways and physiological processes. While current pharmacological strategies target GPCR orthosteric and allosteric sites, as well as G protein transducers, comparable tools for studying βarrs are lacking. Here, we present the discovery and characterization of novel small-molecule allosteric inhibitors of βarrs through comprehensive biophysical, biochemical, pharmacological, and structural analyses. These inhibitors disrupt βarr interactions with agonist-activated GPCRs, impairing receptor internalization, desensitization, and βarr-mediated physiological functions. A cryo-EM structure of βarr1 in complex with the allosteric inhibitor Cmpd-5, complemented by molecular dynamics simulations and mutagenesis studies, reveals that Cmpd-5 binds within a cryptic cleft formed by the middle, C-, and lariat loops–a critical site for βarr activation and recruitment to GPCRs. Thus, Cmpd-5 acts as a molecular lock, hindering βarr1 activation via an allosteric mechanism. These findings introduce novel strategies and tools for probing βarr functions.

Highlights

- Small molecule strategies for modulating βarr functions in both GPCR-dependent and independent contexts.
- Modulators disrupt βarr interaction with GPCRs, impairing their critical functions.
- Cryo-EM structures reveal the allosteric inhibitor Cmpd-5 binding to a cryptic pocket between the N and C domains in the central crest of βarr1, inhibiting its activation.
- Structural analyses, including cryo-EM, MD simulations, and mutagenesis, reveal a unique βarr1 conformation induced by Cmpd-5, shedding light on its mechanism of allosteric inhibition.

INTRODUCTION

β-arrestins (βarrs) are essential protein communication hubs that regulate ligand activation, signaling, and trafficking of G protein-coupled receptors (GPCRs) (Lefkowitz, 2013b; Lohse et al., 1990; Peterson and Luttrell, 2017; Pierce et al., 2002). GPCRs represent the most prominent family of transmembrane receptors in humans, encompassing over 800 genes, and are the target of approximately one-third of all FDA-approved drugs (Hauser et al., 2017; Sriram and Insel, 2018). As versatile adapter protein scaffolds, βarrs play a crucial role in GPCR desensitization, endocytosis, and modulation of signaling pathways (Gurevich and Gurevich, 2014; Kahsai et al., 2023; Peterson and Luttrell, 2017). The mammalian arrestin family includes two widely expressed isoforms, βarr1 and βarr2 (also known as arrestin-2 and -3, respectively), along with two visual arrestins, arrestin-1 and -4, which are specialized for rod and cone photoreceptors (Gurevich and Gurevich, 2014; Kahsai et al., 2018; Lefkowitz, 2013b; Peterson and Luttrell, 2017). Upon agonist activation, GPCRs undergo conformational changes that facilitate their interaction with and activation of heterotrimeric G proteins, triggering the production of second messenger molecules and modulation of downstream effectors (Lefkowitz, 2013b; Pierce *et al.*, 2002). Subsequent phosphorylation of the agonist-activated receptors by GPCR kinases (GRKs), primarily within the carboxy-terminal tail, enables βarrs to bind to the receptor (Benovic et al., 1987; Lefkowitz, 2013b; Lohse *et al.*, 1990; Pitcher et al., 1998). This binding sterically hinders further G protein interaction, leading to receptor desensitization, attenuation of G protein-mediated downstream signaling pathways, and receptor internalization via clathrin-coated pits (Ferguson, 2001; Grady et al., 1997; Laporte et al., 1999; Wolfe and Trejo, 2007).

Beyond their traditional role in signaling termination, βarrs also function as versatile signal transduction units, participating independently or in concert with G proteins in diverse signaling cascades (Lefkowitz and Shenoy, 2005; Peterson and Luttrell, 2017; Smith et al., 2021; Thomsen et al., 2016). βarrs scaffold and facilitate interactions with various signaling mediators, including Mitogen-Activated Protein Kinases (MAPKs), the proto-oncogene kinase Src, Nuclear Factor kappa B (NF-kB), AKT (also known as

Protein Kinase B), and Mouse Double Minute 2 Homolog (Mdm2)/p53, among others, as well as various components of the endocytic machinery (Ahn et al., 2020; Kahsai *et al.*, 2023; Lefkowitz and Shenoy, 2005; Pakharukova et al., 2020; Peterson and Luttrell, 2017; Xiao et al., 2007; Xiao et al., 2010). Their involvement spans many biological processes, encompassing gene expression, metabolism, immune function, motility, and apoptosis (Peterson and Luttrell, 2017; Wess et al., 2023b). Consequently, dysregulated βarr signaling is implicated in a broad spectrum of diseases, including cancer, inflammatory and autoimmune disorders, metabolic syndromes, cardiovascular conditions, and neurological disorders (Bagnato and Rosano, 2019; Bond et al., 2019; Fereshteh et al., 2012; Freedman and Shenoy, 2018; Peterson and Luttrell, 2017; Rein et al., 2017; Thathiah et al., 2013; Wess *et al.*, 2023b). Despite their diverse roles, to date, no pharmacological agents directly target βarrs, unlike GPCR transducers such as G proteins and GRKs for which numerous modulators exist (Bouley et al., 2020; Dai et al., 2022; Ferrero and Koch, 2022; Schlegel et al., 2021; Schrage et al., 2015; Thal et al., 2011; Xiong et al., 2019), necessitating reliance on cumbersome animal models and genetic techniques for their study (Gurevich and Gurevich, 2019; Luttrell et al., 2018; Wess *et al.*, 2023b). This underscores the critical need for innovative chemical approaches to explore βarr biology. Here, we report the discovery of the first small molecules that bind βarr, inhibit their function, and provide structural insights into their inhibitory mechanism. These advances open new avenues for studying and manipulating important GPCR signaling pathways.

RESULTS

Discovery of Small Molecule β-arrestin Modulators

To identify small molecules that modulate receptor-dependent and independent βarr activity, we employed a multi-tiered approach, beginning with a biophysical platform to screen for compounds against purified βarr proteins. The primary *in vitro* affinity-based high-throughput screening (HTS) method utilizes differential scanning fluorimetry (DSF), also known as the fluorescence-based protein thermal shift assay (Niesen et al., 2007; Renaud et al., 2016; Vedadi et al., 2006) (**Figure S1**). DSF allows us to measure protein–ligand interactions–in this case, small molecule binding to βarrs–by assessing

changes in the thermal stability of the protein. Specifically, the presence of a ligand can either increase or decrease the thermal stability of the protein. This is indicated by a shift in the melting temperature (T_m) of the protein, referred to as T_m shift (ΔT_m). One of the critical challenges in biochemical screening is achieving meaningful quality control and hit selection from large-scale experimental datasets. To validate the sensitivity and throughput of the DSF assay, we initially used three known βarr1/2 binding ligands as positive controls. These included inositol hexakisphosphate (IP_6) and heparin, which are highly charged natural ligands, as well as a synthetic phosphopeptide (pp) corresponding to the C-terminal portion of the GPCR vasopressin-2 receptor (V_2R), known as V_2Rpp, which activates βarrs. Incubating purified βarr1 or βarr2 with IP_6, heparin, or V_2Rpp resulted in significant T_m shifts compared to βarr1 or βarr2 alone, demonstrating the validity of the DSF assay as a sensitive and robust HTS platform (**Figure S2**).

Using DSF against purified βarr1 or βarr2, we screened a library of 3,500 chemically diverse, drug-like compounds, representing approximately 250,000 compounds from the National Cancer Institute (NCI) database (**Figure S3**). The primary DSF screen identified 56 hits that caused a notable change in the melting temperature (T_m) of βarr1/2 by ≥1.8 °C (ΔT_m) compared to vehicle-treated controls (**Figures S4, 1A,** and **1B**). This ΔT_m threshold was chosen as an arbitrary reference point based on data from the three βarr binding positive control ligands (**Figure S2**), guiding our initial selection process. Compounds were selected if this ΔT_m change was observed for at least one βarr subtype. Hits were then refined through confirmatory DSF assays, two βarr functional activity assessments at a single dose, toxicity evaluations, and intuitive chemical property assessments based on their chemical structure.

This process highlighted compounds with favorable profiles while excluding cytotoxic ones, narrowing the selection to 26 putative βarr inhibitors (**Figures S5, S6,** and **S7**). Among the βarr activity assays, the PathHunter™ βarr recruitment assay employed β-galactosidase (β-gal)-based enzyme fragment complementation (EFC) technology to measure βarr recruitment to an agonist-stimulated receptor (**Figures 1C** and **S6**). In this

assay, U2OS cells co-express a chimeric β_2V_2R receptor, which combines the β_2-adrenergic receptor (β_2AR) with a C-terminal tail replaced by the V_2R tail, along with βarr2, with each protein fused to complementary β-gal fragments. Specifically, the receptor is tagged with the ProLink (PK) portion of β-gal, while βarr2 is tagged with the Enzyme Acceptor (EA) portion (**Figure 1C,** upper panel). Upon agonist-induced recruitment of βarr2 to the β_2V_2R, the β-gal fragments complement, generating a chemiluminescent signal. Importantly, the β_2V_2R chimeric receptor retains pharmacological properties similar to the native β_2AR while offering a more stable interaction with βarrs (Oakley et al., 2000; Shukla et al., 2013; Shukla et al., 2014). The second assay measures βarr activity by evaluating the high-affinity binding state formed with the radio-labeled agonist–[^{3}H](R,R′)-4-methoxyfenoterol (referred to as ^{3}H-Fen hereafter); (Ahn et al., 2017; Toll et al., 2012) and phosphorylated β_2V_2R ($p\beta_2V_2R$) in membranes (**Figures S7** and **1D**). This assay quantifies β_2AR in its active conformation, where βarr coupling reciprocally enhances the binding affinities of both the agonist (^{3}H-Fen) and βarr (Ahn *et al.*, 2017; DeLean and Lefkowitz, 1980; Gurevich et al., 1997). Nearly all 26 small molecules inhibited βarr1/2 activities–both βarr recruitment and the formation of the high-affinity agonist binding state–by ≥30% for one of the βarr isoforms (**Figures S6** and **S7**). Four compounds were selected for extensive characterization as βarr inhibitors, as they each inhibited βarr activity by approximately 40% in both agonist-stimulated βarr recruitment to β_2V_2R and in promoting the βarr-induced high-affinity agonist state of $p\beta_2V_2R$ (**Figures 1C** and **1D**). The selection of these compounds was guided by their efficacy in inhibiting βarr1/2 activity and favorable chemical properties, such as aqueous solubility and permeability. These four compounds, designated as Cmpd-5, Cmpd-30, Cmpd-46, and Cmpd-64 (see Methods for chemical names), are depicted in **Figure 1E**. Subsequently, we used isothermal titration calorimetry (ITC) to measure the binding affinity of the compounds by evaluating their direct physical interactions with βarr1/2. All four modulators exhibited favorable binding to both βarr1 and βarr2, with dissociation constant (K_D) values ranging from high nanomolar to low micromolar, indicating substantial binding interactions (**Figures 1F** and **S8**). These results indicate that while Cmpd-5 is non-selective between the two isoforms, Cmpd-30

and Cmpd-46 exhibit slight selectivity for βarr2, and Cmpd-64 shows ~6-fold selectivity for βarr2 over βarr1.

β-arrestin Modulators Inhibit β-arrestin Recruitment to Agonist-Activated GPCRs

To quantitatively evaluate the effects of these modulators on βarr recruitment to GPCRs in a dose-response manner, we employed the DiscoveRx PathHunter™ βarr recruitment assay system (Ahn *et al.*, 2017). In alignment with previous single-dose results (**Figures 1D** and **S6**), all four modulators exhibited a dose-dependent inhibition of isoproterenol (ISO)-induced βarr2 recruitment to the β_2V_2R (**Figures 2A-2D**). Each modulator effectively reduced the maximal ISO-induced βarr2 recruitment (E_{max} reductions at 50 μM: 77.0% [Cmpd-5], 85.5% [Cmpd-30], 77.0% [Cmpd-46], and 75.0% [Cmpd-64]). These results highlight a robust inhibition of βarr2 recruitment across all tested modulators. Moreover, using the same assay system, we observed similar inhibitory effects of the modulators on angiotensin II (Ang-II)-induced βarr2 recruitment to the angiotensin II type-1 receptor (AT_1R), indicating that the modulators exhibit comparable efficacy across different receptor systems (**Figure 2E**). Motivated by the observed effects on βarr2 recruitment across two receptor systems, and given the similarity yet sometimes opposing effects of the βarr isoforms, we next investigated the impact of these modulators on the recruitment of both βarr1 and βarr2 to an agonist-activated V_2R using NanoBiT βarr recruitment technology (**Figure 2F**). This method employs a split luciferase protein complementation approach, with one part of the split NanoLuciferase (LgBiT) fused to V_2R and the other part (SmBiT) fused to βarr1 or βarr2. The principle relies on the functional complementation of these split luciferase components, generating a chemiluminescence signal that enables the detection of βarr recruitment (Daly et al., 2023; Dixon et al., 2016; Pandey et al., 2021). Specifically, we examined βarr1 and βarr2 recruitment to V_2R using this NanoBiT sensor system. Co-expression of SmBiT-fused βarr1 or βarr2 and LgBiT-fused V_2R in βarr1/2-deficient HEK293 cells allowed us to measure luminescence kinetics following pretreatment with the modulators and stimulation with arginine vasopressin (AVP), the V_2R agonist. The NanoBiT assay confirmed that the modulators consistently inhibited βarr recruitment, with comparable levels of inhibition observed for both βarr1 and βarr2 (**Figures 2G** and

2H). This further demonstrates the effects of the modulators on βarr coupling to the agonist-activated receptor. These findings complement the ^{3}H-Fen binding results for βarr1/2 coupling to β_2V_2R presented in **Figure S7**. Furthermore, we assessed the effects of these modulators on βarr recruitment to a phosphorylated receptor *in vitro*. Using $p\beta_2V_2R$ derived from insect cells, we formed a complex with βarr1, stabilized with the Fab30 antibody fragment specific to V_2Rpp-bound active βarr1 (Shukla *et al.*, 2013; Shukla *et al.*, 2014), which enhances receptor-βarr1 interactions to a nanomolar level (Asher et al., 2022). Given this robust interaction, the results showed attenuation of agonist-induced β_2V_2R–βarr1 complex formation (**Figure S9**). Collectively, these results demonstrate that the modulators effectively bind to βarrs and attenuate agonist-induced GPCR–βarr interactions, indicating broad-spectrum functional modulation.

β-arrestin Modulators Reduce Agonist-Stimulated Receptor Desensitization

Prolonged activation of GPCRs results in a diminished response to agonists, partly due to βarr binding to phosphorylated receptors, leading to receptor–G protein uncoupling (Ferguson, 2001; Lefkowitz, 2013a; Lohse *et al.*, 1990; Peterson and Luttrell, 2017). Consequently, this desensitization process results in the internalization and subsequent loss of receptors from the cell surface. To investigate the effects of βarr modulators on agonist-induced receptor desensitization, we employed two fluorescence sensor-based assays to monitor the real-time kinetics of second messenger generation, specifically cAMP and Ca^{2+}. The first assay enabled real-time measurement of cAMP production using a fluorescence resonance energy transfer (FRET)-based biosensor reporter, ICUE2 (Violin et al., 2008) (**Figure 3A**). HEK293 cells, which endogenously express both βarr1 and βarr2 at high levels (Kahsai *et al.*, 2023; Menard et al., 1997) and stably express the cAMP biosensor (ICUE2: CFP-Epac2-YFP), were used. Cells were incubated with individual βarr modulators, followed by stimulation of the $G\alpha_s$-coupled β_2AR with ISO, and the levels of cAMP production were measured. Pretreatment with the modulators markedly inhibited agonist-stimulated β_2AR desensitization, as evidenced by elevated and prolonged cAMP levels compared to the control (**Figures 3B** and **3C**). All four modulators led to a marked increase in agonist-induced cAMP accumulation in ICUE2 cells, with cAMP levels rising to 191% for Cmpd-5, 211% for

Cmpd-30, 207% for Cmpd-46, and 282% for Cmpd-64, compared to the baseline 100% observed in the DMSO control. We next investigated the impact of modulators on desensitization of the $G\alpha_q$-coupled GPCR, AT_1R, by measuring agonist (Ang-II)-induced calcium mobilization in HEK293 cells stably expressing AT_1R (**Figure 3D**) (Li et al., 2023). Similar to our β_2AR findings, modulators significantly inhibited Ang-II-stimulated AT1R desensitization, enhancing calcium signaling through $G\alpha_q$ activity (**Figures 3E** and **3F**). Importantly, Ca^{2+} mobilization increased significantly relative to DMSO control, with Ca^{2+} levels of 279% for Cmpd-5, 590% for Cmpd-30, 356% for Cmpd-46, and 490% for Cmpd-64, compared to 100% for the control. To confirm modulator specificity for βarr-mediated desensitization inhibition, we conducted a similar calcium signaling assay in parental HEK293 cells and CRISPR/Cas9-induced βarr1/2 knockouts, each with transient AT_1R expression (**Figures 3G-3J**). In parental cells, treatment with modulators led to a significant reduction in desensitization, resulting in a 4- to 5-fold increase in Ang-II-stimulated calcium mobilization (**Figures 3G-3H**). In knockout cells lacking both βarr1 and 2, Ang-II-stimulated Ca^{2+} mobilization was five times higher than in parental cells, and modulators did not lead to a further significant increase (**Figures 3I-3J**). These findings highlight the dependence of the modulator-mediated inhibition of receptor desensitization on βarrs, further confirming the specificity of their effects. Biochemical binding tests further support this, revealing minimal interaction of the modulators with non-target proteins, such as kinases including ERK2, c-Src, and p38α (**Figure S10**), suggesting limited off-target activity. Collectively, these results suggest that the modulators inhibit βarrs likely by inducing conformational changes that prevent βarr coupling to GPCRs, thereby downregulating receptor desensitization.

β-arrestin Modulators Inhibit Agonist Promoted GPCR–β-arrestin Endocytosis

Agonist-induced βarr recruitment to GPCRs promotes receptor endocytosis (Ferguson, 2001; Laporte et al., 2000; Oakley *et al.*, 2000). Given that all four modulators inhibited βarr recruitment, we evaluated their effect on agonist-promoted receptor internalization to understand the downstream impact. Specifically, we tested the effect of the four modulators on the agonist-promoted internalization of chimeric β_2V_2R with βarr2, using

the PathHunter β-gal reporter fragment complementation assay. This assay was conducted in U2OS cells, stably expressing split β-gal fragments targeted to βarr2 and endosomes (**Figure 4A**). Treatment with increasing concentrations of the modulators significantly reduced the maximal ISO-induced receptor/βarr2 internalization response in a dose-dependent manner (% reduction in E_{max} with 25 μM modulator [Cmpd-5, -30, -46, and -64]: 93%, 93.5%, 88%, and 87%, respectively) (**Figures 4B-4E**). To verify that the modulators inhibit agonist-induced receptor endocytosis, we employed a "bystander" bioluminescence energy transfer (BRET)-based assay to quantify V_2R-RlucII endocytosis (Smith et al., 2017) (**Figure 4F**). This assay measures the association of GPCR tagged with RlucII with the early endosomal marker 2xFYVE-mVenus. Stimulation with AVP resulted in a concentration-dependent increase in the net BRET ratio, indicating increased V_2R endocytosis (**Figures 4G** and **4H**). As expected, treatment with all βarr modulators significantly decreased the AVP-induced signal, confirming the inhibition of receptor internalization to early endosomes, which is a βarr-dependent event. Collectively, these results support the notion that the modulators directly bind to βarrs, preventing receptor–βarr interaction and profoundly altering their functions.

Effect of Modulators on β-arrestin-Mediated ERK Activation Downstream of GPCRs

GPCR-stimulated ERK1/2 activation has been shown to occur through a βarr-dependent mechanism (Luttrell et al., 1999; Luttrell *et al.*, 2018; Noma et al., 2007; Peterson and Luttrell, 2017; Wisler et al., 2007). We directly tested the effect of modulators on the response of GPCR-stimulated βarr-dependent ERK1/2 activation by using carvedilol, a biased agonist and clinically useful β-blocker known to antagonize stimulation of $G\alpha_s$ while inducing moderate ERK activation in a βarr1/2-dependent way (Kim et al., 2008; Luttrell *et al.*, 2018; Wang et al., 2017; Wisler *et al.*, 2007) (**Figure 5A**). This approach allowed us to evaluate the impact of the modulators on βarr1/2-dependent ERK activation. We observed that three of the modulators (Cmpd-5, -46, and -64), as expected, attenuated the GPCR, β_2AR-mediated βarr1/2-dependent ERK activation, as shown in **Figure 5B**. In contrast, Cmpd-30 uniquely promoted ERK

phosphorylation while consistently inhibiting βarr recruitment, desensitization, and internalization of receptors, among others (**Figures 5B, S11,** and **S12A**). The βarr dependence of Cmpd-30-induced ERK activation was confirmed by siRNA-induced reduction of βarr1/2 levels, which significantly impaired ERK activation compared to control cells (**Figure S12A**). Similarly, Cmpd-30 activated p38α, another βarr-scaffolded effector, with this effect being abolished in βarr1/2 knockout cells, indicating that both ERK and p38α activation depend on βarr1/2 (**Figure S12B**). Given that these results may suggest a potential alternative βarr-mediated mechanism for effector activation that diverges from the typical GPCR–βarr pathway, the precise details of this mechanism warrant further investigation. In addition, to further confirm the specificity of the effects of the four modulators on βarr-mediated ERK activation within GPCR pathways, we assessed their impact on EGF-induced ERK phosphorylation. It is noteworthy that pretreatment with Cmpd-5, -30, -46, and -64 did not affect EGF-induced ERK phosphorylation, suggesting that the modulators specifically target βarr-mediated pathways. (**Figure S13**). In this context, it is also important to add that in many experiments, we used higher concentrations of the modulators than their binding affinities required to ensure maximal cellular effects. The observed effects in cell-based assays do not appear to directly correlate with their measured affinities, likely due to differences in cell permeability and metabolic stability affecting intracellular concentrations.

β-arrestin Modulators Impair Chemokine-Induced T-Cell Migration

βarrs scaffold multiple proteins that control cell polarity and influence cellular migration downstream of GPCRs, including chemokine receptors (Cheung et al., 2009; McGovern and DeFea, 2014; Smith et al., 2018b). To investigate whether compounds 5, 30, 46, and 64 affect this complex, βarr-dependent cellular function, we examined their effect on the chemotaxis of wild-type mouse T cells (**Figures 5C-5E** and **S14**). We focused on chemokine receptor 7 (CCR7), as it is widely expressed in various T cell populations and is integral to the T cell chemotaxis (Comerford et al., 2013). All four βarr modulators significantly disrupted T cell chemotaxis, affecting both $CD4^+$ (helper) and $CD8^+$ (cytotoxic) T cell populations (**Figures 5C-5E** and **S14**). The extent of inhibition of T cell

chemotaxis by each compound was similar across each cell subpopulation (average % inhibition of total T cell chemotaxis [total, helper, and cytotoxic T cells] by 20 μM Cmpd-5, Cmpd-30, Cmpd-46, and Cmpd-64: [95%, 88%, 99%, and 97%], respectively).

Structural Determination and Analysis of Cmpd-5-Bound βarr1 Complex

To elucidate the mechanisms underlying βarr1 inhibition by modulators, we utilized single-particle cryo-EM to investigate the βarr1–Cmpd-5 complex. We selected Cmpd-5 for this analysis in part due to its relatively non-selective behavior between the two βarr isoforms (**Figures 1F** and **S8**) and its qualitatively better aqueous stability compared to other inhibitors, which contributed to improved sample quality for cryo-EM studies. To facilitate particle alignment in cryo-EM reconstructions, we inserted a BRIL domain at the hinge region of βarr1 and employed the anti-BRIL Fab, BAG2 (Mukherjee et al., 2020), along with an anti-Fab nanobody (aFabNb) (Ereno-Orbea et al., 2018) as fiducial markers (**Figure S15A**). Importantly, the BRIL insertion did not impair the ability of βarr1 to bind Cmpd-5 and V_2Rpp or to promote the high-affinity agonist state of pβ_2V_2R (**Figures S15B, S15C,** and **S15D**), indicating that βarr1-BRIL remained fully functional. This approach thus increased the complex size, aiding in 3D classification and reconstruction (**Figure S16; Table S1**). Cryo-EM analysis resolved the complex structure at 3.47 Å, revealing distinct densities for βarr1 and Cmpd-5 (**Figures 6A** and **S17**). The density attributable to Cmpd-5 is located in a pocket within the central crest region of βarr1, positioned between the N and C domains.The pocket is formed by the middle loop (residues 129-140), the C-loop (residues 241-249, including β-strand XVII), and the lariat loop (residues 274-300). Hereafter, we refer to these collectively as the MCL loops, which together form the MCL site (**Figures 6A-6C** and **S17**). Unlike the native binding pocket in the N domain groove of βarrs, where GPCR C-tails typically bind (Shukla *et al.*, 2013), this MCL site may represent a previously unrecognized allosteric site.

Molecular Basis for Cmpd-5-Mediated Allosteric Inhibition of βarr1.

To validate the binding of Cmpd-5 within the MCL site, we determined the cryo-EM structure of apo-state βarr1-BRIL at a resolution of 3.52 Å (**Figure S18**). The apo-state

map supported the presence of Cmpd-5 within the MCL site, as indicated by the absence of density near the binding site in the apo-state, contrasted with the distinct and clear density observed for Cmpd-5 in the Cmpd-5-bound βarr1 structure (**Figures S18A** and **S18B**). To further substantiate this finding, we generated a difference map by subtracting the apo-βarr1 density from the Cmpd-5-bound βarr1 (Joseph et al., 2020), which revealed additional clear density near the MCL cleft, further confirming Cmpd-5 binding (**Figure S18C**). While the observed density was sufficient to confirm Cmpd-5 binding within the MCL cleft, modeling the compound in a specific conformation was challenging due to its greater conformational flexibility and relatively peripheral location. This flexibility, further observed through molecular dynamics (MD) simulations described in the following sections, suggests that while the density maps confirm binding, they may not fully represent the range of conformations for the compound. The resulting model demonstrates that Cmpd-5 interacts with both hydrophilic and hydrophobic residues at the βarr1–Cmpd-5 interface (**Figures 6C** and **6D**). The hydrophobic regions of Cmpd-5, particularly the four cyclic hydrocarbon rings, align with hydrophobic areas within the C-loop of βarr1, including Y249 and C251, reinforcing the interaction. Additionally, polar interactions may be facilitated by E134 (middle loop), K250 (C-loop), and potentially R285 (lariat loop), which appear to engage with the oxygen atoms of Cmpd-5. Although the density for the side chain of R285 is not observed, likely due to its flexibility resulting from compound binding, it appears to accommodate the hydroxyl oxygen atoms of Cmpd-5. These hydrophobic and polar interactions are crucial for effective binding at the MCL site, suggesting that the full binding dynamics extend beyond what the density maps represent (**Figures 6D** and **S18C**).

To gain deeper insights into the allosteric inhibition of βarr1 by Cmpd-5 and to assess its dynamics within the βarr1 complex, we performed extensive MD simulations (**Figure 6E; Table S2**). These simulations provided detailed insights into how Cmpd-5 interacts with the MCL site and its behavior over time. Consistent with the cryo-EM structural results, the simulations revealed that Cmpd-5 stably occupies the MCL cleft, nestling into the pocket and maintaining stable poses despite the inherent flexibility of the MCL loops (**Figures 6E** and **S19**). Additionally, Cmpd-5 was observed forming polar

interactions, particularly with R285, and establishing hydrophobic contacts with Y249, C251, and L129.

To further validate the structural observations of Cmpd-5 binding within the MCL cleft of βarr1 and to better understand its inhibitory mechanism, we conducted targeted mutagenesis. Building on insights from cryo-EM data, we introduced specific point mutations at key residues within the Cmpd-5 binding site. Subsequently, we evaluated how these mutations affected Cmpd-5 inhibition by analyzing changes in βarr coupling to the high-affinity agonist state of $p\beta_2V_2R$ using ^{3}H-Fen binding experiments. In addition, we measured the binding affinity of Cmpd-5 for both wild-type and mutant forms of βarr1 using ITC (**Figures 6F, 6G, S20, S21,** and **S22).** Remarkably, mutations in βarr1, such as L129G, P133A, E134A, Y249A, C251A, K284A, and R285A, caused substantial reductions in the ability of Cmpd-5 to inhibit βarr1 coupling to the receptor, by 5.5-, 3.8-, 2.6-, 3.2-, 4-, 3.8-, and 2.4-fold, respectively, compared to wild-type βarr1 (**Figures 6F** and **S21**). In contrast, mutations such as P131A, D135A, K138A, C140A, and E283A had minimal effects on Cmpd-5 inhibition. Building on these observations, ITC analysis provided additional insights into Cmpd-5 binding within the MCL cleft, complementing the βarr1-coupling experiments conducted with ^{3}H-Fen binding $p\beta_2V_2R$ (**Figures 6G** and **S22**). By focusing on selected residues with marked effects as well as those with lesser impact, we obtained a more comprehensive understanding of the binding characteristics of Cmpd-5 in the MCL cleft. The ITC results revealed reductions of 5.5, 2.8, 7.3, 2.7, 10.6, 8.3, and 46.5-fold for L129G, P133A, E134A, K138A, Y249A, C251A, and R285A, respectively, relative to βarr1-WT. Mutations E134A and R285A led to significant reductions in both binding affinity and inhibitory activity, highlighting their crucial roles in polar interactions with Cmpd-5. The substantial reduction in binding affinity for the R285A mutant, accompanied by an enthalpic change (ΔH shifting from approximately −13.4 kcal/mol in wild-type to -1.5 kcal/mol in R285A), points to a significant loss of polar interactions **(Figure S22)**. This could involve hydrogen bonding or other polar contacts between Cmpd-5 and the binding site, potentially extending beyond the effects of the R285A mutation. Similarly, mutations Y249A and C251A also resulted in reduced binding affinity, likely due to the disruption of essential hydrophobic

interactions and other potentially weaker polar interactions with Cmpd-5. It is also important to note that while residues L129 and P133 are not in direct proximity to Cmpd-5 in the cryo-EM structure, mutations L129G and P133A still impact Cmpd-5 binding. This observation suggests that these residues may be involved in stabilizing favorable conformations for the interaction between Cmpd-5 and βarr1. Together, cryo-EM, MD simulations, and mutagenesis studies reveal that Cmpd-5 binds to βarr1 through a combination of hydrophobic and hydrophilic interactions, with ITC data confirming that the binding involves both enthalpic and entropic factors (**Figure S22A**). Interestingly, sequence alignment of the Cmpd-5 binding pocket within the MCL site between βarr1 and βarr2 (*Rattus norvegicus*) reveals identical residues, suggesting a conserved binding mode across these two βarr variants (**Figure 6H**) with similar affinities (**Figures S8A** and **S8B**).

Distinct Conformational State Induced by Cmpd-5 in βarr1

To elucidate the conformational changes underlying the allosteric inhibition of βarr1 by Cmpd-5, we compared the Cmpd-5-bound and apo-state structures (**Figures 7A-7C**). This comparison revealed substantial conformational rearrangements induced by Cmpd-5 binding, while the overall protein architecture remained largely preserved. The most pronounced changes were observed in key loops within the central crest region, accompanied by an 8° interdomain rotation between the N and C domains (**Figure 7A**). Notably, the difference density map showed distinct density around the N domain (**Figure S18C**), likely reflecting this interdomain rotation. In addition to this interdomain twist, Cmpd-5 binding induced bending of the middle loop, reorienting its tip toward the Cmpd-5 binding site and the C-domain, effectively capping the pocket and reducing its volume. As a result of this shift, the bent portion of the middle loop moved closer to the finger loop (**Figure 7B**). This rearrangement likely contributes to the increased flexibility of the finger loop, which may explain its weaker density in the Cmpd-5-bound structure. Supporting this, MD simulation analyses show that while the finger loop does not directly interact with Cmpd-5, it frequently engages with the N domain groove. Additionally, Cmpd-5 binding caused a substantial shift in the C-loop and promoted a helix-to-loop transition within the lariat loop (residues 282-285) (**Figure 7C**).

Superposition of the βarr1–Cmpd-5-bound structure with the βarr1–V_2Rpp active-state structure (Shukla *et al.*, 2013) revealed, on the other hand, key structural differences in the central crest region of βarr1 (**Figure 7D**). In the active state, the MCL pocket is relativley larger, primarily due to the middle loop shifting toward the N domain, which expands the cleft to accommodate key receptor components such as ICL2, as observed in multiple active GPCR–βarr1 complexes (Bous et al., 2022; Cao et al., 2022; Lee et al., 2020; Staus et al., 2020; Wang et al., 2024; Zhou et al., 2017). In contrast, Cmpd-5 binding induces a conformational rearrangement of the middle loop, reorienting its tip toward the Cmpd-5 binding site and the C-domain, along with changes in the C-loop, lariat loop, and an 8° interdomain twist (**Figures 7A-7D** and **S23A**). These collective rearrangements constrict the MCL cleft in the Cmpd-5-bound structure, preventing it from accommodating GPCR components such as ICL2, unlike the active βarr1 state (**Figures S23B-S23D**). Consequently, the Cmpd-5-stabilized βarr1 conformation becomes distinct from both active and inactive states, as corroborated by MD simulations (**Figures S24**). This allosterically induced conformational change effectively locks βarr1 into a state that precludes engagement with GPCRs and ultimately inhibits βarr and receptor signaling.

DISCUSSION

βarrs play a crucial role in regulating diverse GPCR signaling pathways, profoundly influencing both physiological functions and pathophysiological processes (Gurevich and Gurevich, 2019; Lefkowitz and Shenoy, 2005; Peterson and Luttrell, 2017; Smith and Rajagopal, 2016; Wess *et al.*, 2023b). To date, the study of βarr functions has predominantly relied on genetic manipulation techniques such as knockout, gene silencing, and, more recently, CRISPR/Cas9-mediated editing (Bohn et al., 1999; Conner et al., 1997; Kohout et al., 2001; Luttrell *et al.*, 2018; Peterson and Luttrell, 2017; Wess *et al.*, 2023b). While these methods have provided valuable insights, they are limited by a lack of reversibility and temporal control. Moreover, genetic knockouts, including those achieved with CRISPR/Cas9, can induce compensatory mechanisms that obscure the true function of the targeted gene as cells adjust to the gene loss

(Lefkowitz et al., 2023; Luttrell *et al.*, 2018). Small molecule modulators offer a promising alternative, providing reversible and precise temporal control over βarr activity with the advantage of ease of delivery. Although βarr1 and βarr2 share ~78% sequence identity, they exhibit distinct and sometimes opposing physiological roles in GPCR signaling (Peterson and Luttrell, 2017; Wess et al., 2023a). Despite the demonstrated therapeutic potential of targeting βarr isoforms through knockouts in animal models, effective small molecule modulators for βarrs have been lacking in biomedical research and preclinical development. Herein, we present the discovery of small molecule inhibitors targeting βarr activities, identified through biophysical screening followed by biochemical, pharmacological, functional, and structural analyses. Four βarr-binding compounds–Cmpd-5, Cmpd-30, Cmpd-46, and Cmpd-64–were shown to act as negative βarr modulators. These modulators disrupt βarr interactions with agonist-activated GPCRs, impairing receptor internalization, and desensitization, thereby impacting essential βarr-mediated regulation of GPCR signaling.

By binding to receptors during continuous agonist stimulation, βarrs sterically hinder receptor–Gα interactions, facilitating GPCR desensitization (Benovic *et al.*, 1987; Lefkowitz, 2013b; Lohse *et al.*, 1990; Pitcher *et al.*, 1998). We found that all four βarr-binding modulators delayed agonist-induced receptor desensitization and enhanced second messenger production (cAMP and Ca^{2+}) through β_2AR–Gα_s and AT_1R–Gα_q coupling, respectively, to sustain receptor–Gα signaling. Notably, inhibition of desensitization was minimal in βarr1/2 knockout cells, underscoring the dependence of their effects on βarr activity and strongly suggesting minimal off-target activity within these signaling pathways. Pharmacological studies with radiolabeled β-agonists similarly confirmed that all four modulators inhibit βarr-coupling to high-affinity agonist-bound receptor state. Since receptors such as β_2AR and AT_1R require an active transducer βarr conformation for coupling (Asher *et al.*, 2022; DeLean and Lefkowitz, 1980; Gurevich *et al.*, 1997; Lee *et al.*, 2020), this would imply that modulators act via an allosteric inhibitory mechanism. Our findings also suggest that inhibiting βarr signaling effectively biases the agonist response toward the G protein pathway, thus presenting a strategy with substantial clinical potential.

Many existing GPCR-targeting drugs lack transducer specificity (Hauser *et al.*, 2017; Kahsai et al., 2016; Kahsai et al., 2011; Smith et al., 2018a; Violin et al., 2014; Whalen et al., 2011; Wootten et al., 2018), often impacting both βarr and G protein pathways equally. This can be problematic, as GPCR signaling via βarr or G proteins may lead to different outcomes depending on the receptor context. For example, in asthma, βarr signaling causes desensitization of β_2AR, which worsens bronchospasm and aggravates inflammation, while G protein signaling promotes smooth muscle brochodilation (Ahn et al., 2023; Bond *et al.*, 2019; Walker and DeFea, 2014; Walker et al., 2003). By targeting selective βarr inhibition, it may be possible to enhance G protein signaling, thus sustaining β_2AR stimulation and potentially improving asthma treatments. This 'biased signaling' approach suggests that small molecule βarr modulators could help better direct GPCR responses and optimize therapeutic outcomes.

Beyond their canonical role in GPCR signaling regulation, βarrs also initiate G protein-independent signaling pathways by scaffolding agonist-activated GPCRs to downstream effectors such as the c-Raf–MEK1–ERK1/2 cascade, thus mediating GPCR-stimulated ERK1/2 activation (Kahsai *et al.*, 2023; Lefkowitz and Shenoy, 2005; Luttrell *et al.*, 1999; Luttrell et al., 2001; Luttrell *et al.*, 2018; Peterson and Luttrell, 2017; Smith *et al.*, 2018a; Wisler *et al.*, 2007). We observed that Cmpds-5, -46, and -64 effectively inhibited carvedilol-mediated βarr-dependent ERK activation through β_2AR. In contrast, Cmpd-30 unexpectedly enhanced ERK activation, suggesting a novel mechanism for effector activation that warrants further investigation. In addition to their role in GPCR-mediated ERK signaling, βarrs are also known to orchestrate cell migration in malignancy by scaffolding proteins involved in cell polarity and actin dynamics downstream of GPCRs (McGovern and DeFea, 2014; Peterson and Luttrell, 2017; Zoudilova et al., 2010). Our findings show that Cmpds-5, -30, -46, and -64 inhibit chemokine-induced T-cell migration by blocking βarr activity. This is consistent with previous observations that βarr-deficient cells exhibit reduced CCR4-, CXCR3-, and AT_1R-mediated chemotactic activity (Hunton et al., 2005; Jiang et al., 2013; Lin et al.,

2018; Peterson and Luttrell, 2017; Smith *et al.*, 2018b). Thus, small molecules able to modulate cell migration signals via a βarr target could be a valuable approach for cancers with disrupted βarr function.

The current study not only provides mechanistic insights into βarr1 inhibition but also offers detailed structural and functional analyses of its interaction with the allosteric inhibitor Cmpd-5. Using cryo-EM, we captured the structures of βarr1 in its Cmpd-5-bound and apo states. Furthermore, complementing these structural findings, MD simulations and structure-guided mutational analyses reveal that Cmpd-5 specifically binds to the middle, C, and lariat loops–collectively referred to here as the MCL cleft–within βarr1. This site, located in the central crest between the N and C domains, accommodates intracellular loops, particularly ICL2, of GPCRs in receptor–βarr complexes (Bous *et al.*, 2022; Cao *et al.*, 2022; Lee *et al.*, 2020; Staus *et al.*, 2020; Wang *et al.*, 2024; Zhou *et al.*, 2017). Therefore, it occupies a pocket that plays a key role in βarr activation and its subsequent recruitment to GPCRs.

In the active state of βarr1, whether in complex with phosphopeptides or full-length GPCRs, the MCL cleft adopts a more spatially open conformation. This transition, driven by the movement of the middle loop toward the N domain and the ~20° interdomain twist, increases the pocket volume to accommodate receptor components such as ICL2 and facilitates coupling (Bous *et al.*, 2022; Cao *et al.*, 2022; Lee *et al.*, 2020; Shukla *et al.*, 2013; Staus *et al.*, 2020; Wang *et al.*, 2024; Zhou *et al.*, 2017). In contrast, Cmpd-5 binding induces conformational rearrangements, particularly the reorientation of the middle loop tip toward the Cmpd-5 binding site and the C-domain. Along with conformational changes in the C-loop, lariat loop, and an 8° interdomain twist, these changes ultimately constrict the MCL cleft, reducing its volume. This constriction renders the MCL cleft incompatible with critical GPCR components, such as ICL2, which are essential for receptor coupling. By occupying the cleft, Cmpd-5 restricts the structural flexibility required for βarr1 to transition into an active conformation capable of engaging with the receptor. Thus, Cmpd-5 acts as an effective allosteric inhibitor, stabilizing a distinct conformation of βarr1 that disrupts its functional interaction

with GPCRs. The Cmpd-5-stabilized βarr1 conformation is distinct from both the active and inactive states (Han et al., 2001; Milano et al., 2002), as supported by our MD simulation studies. Through this allosteric mechanism, Cmpd-5 locks βarr1 into a conformation that renders it incapable of engaging with GPCR components like ICL2, ultimately preventing βarr and receptor signaling. Given that βarrs are known to adopt multiple conformations to carry out their functions, it is not surprising that Cmpd-5 stabilizes this unique βarr1 conformation, thereby advancing our understanding of these dynamic and multifaceted proteins (Kahsai *et al.*, 2018; Lee et al., 2016; Nuber et al., 2016; Smith and Rajagopal, 2016). Overall, Cmpd-5 modulates βarr1 function, locking it into a unique inactive-like state. While this study primarily focuses on Cmpd-5, it lays the groundwork for future investigations into the mechanisms of action of other βarr1 modulators and inhibitors. This work could, therefore, potentially offer further insights into their structural basis for inhibition and expand our understanding of βarr1 function. Moreover, this study highlights the potential of the MCL cleft–a previously unexplored pocket–as a novel target for modulating βarr1 functions and influencing GPCR signaling pathways.

In summary, our study introduces innovative small molecule-based strategies to modulate βarr activities by disrupting their interactions with activated GPCRs. This disruption, in turn, influences critical functions within GPCR signaling pathways. Additionally, these βarr-binding compounds represent valuable new tools for investigating both GPCR-dependent and independent aspects of βarr biology. This work not only sheds light on βarr conformational dynamics and elucidates the underlying mechanisms of allosteric inhibition but also lays the groundwork for understanding the structure-function relationships of βarrs. Thus, our findings mark a significant advancement in pharmacological strategies, transitioning from a traditional focus on GPCRs to directly modulating βarr functions.

Limitations of the study

In this study, we characterized small-molecule βarr modulators and investigated the mechanism of allosteric inhibition of βarr1 by Cmpd-5. While key mechanistic insights

were gained, the analysis was limited to a single modulator. Future studies on additional modulators may reveal divergent βarr mechanisms and expand our understanding of βarr signaling. Furthermore, although βarr inhibitors showed potent *in vitro* binding affinities, higher cellular concentrations were required, likely due to limited permeability and stability. Thus, medicinal chemistry optimization is needed to enhance potency. Additionally, this study focused on general βarr inhibition as a proof of concept, with limited exploration of isoform-specific effects. Given the distinct roles of βarr1/2 in signaling and disease, further investigation using a broader GPCR panel, including class A and B receptors, is needed to better understand their functions. We used βarr1/2 knockout cells to assess modulator specificity, showing effects on βarr-mediated desensitization in parental but not knockout cells. ITC assays for βarr1/2 and binding tests with ERK2, c-Src, and p38α indicated minimal off-target effects. However, given the quite large range of cellular signaling molecules, further testing with additional proteins, such as G proteins and cellular systems, including βarr1/2 reintroduction, is needed to confirm specificity and generalizability. Although cryo-EM analysis allowed us to confidently assign the Cmpd-5 binding site, the conformational flexibility of this complex natural product–with multiple chiral centers, rotatable bonds, and rings–posed challenges in precisely defining its orientation within the binding site. Finally, our structural studies relied on a BRIL-tagged βarr1 rather than native βarr1 (~46 kDa) to facilitate particle alignment during cryo-EM analysis.

FIGURE LEGENDS

Figure 1. Generation of Small Molecule Modulators of βarrestins. (**A** and **B**) DSF melting profiles of (A) βarr1 (5 µM) and (B) βarr2 (5 µM) with indicated modulators (100 µM) and controls. Left panels show normalized fluorescence versus temperature DSF profiles; right panels display T_m shifts (Δ T_m in °C) of modulators for βarr1 or 2. (**C**) Top panel, PathHunter βarr2 recruitment assay. U2OS cells co-express GPCR (β_2V_2R) with a small β-gal fragment (ProLinkTM; PK) and βarr2 with a large β-gal fragment (EA). Agonist-induced βarr2 recruitment results in β-gal complementation and chemiluminescence. Lower panel Effect of βarr modulators (50 µM) on βarr2 recruitment to agonist-activated GPCRs, assessed by the PathHunter assay. Cells were treated with the modulator (50 µM for 30 min) and then stimulated with 10 nM β_2AR agonist isoproterenol (ISO). (**D**) Effect of modulators on βarr-promoted high-affinity agonist binding. Top Panel: Schematic illustrating βarr binding increases agonist affinity for phosphorylated GPCR, generating a high-affinity state. Here, this is measured as βarr activity through agonist (^{3}H-Fen; 6 nM) binding. Lower Panel: Adding exogenous βarr2 (black bar; 2 µM) increases high-affinity agonist binding to pβ_2V_2R (light red bar); modulators inhibit this effect (100 µM) (**E**) Chemical structures of four βarr modulators

(Cmpds-5, -30, -46, and -64). (**F**) Isothermal titration calorimetry (ITC) was used to assess the physical interaction and determine the dissociation constants (K_D) for the four modulators binding to βarr1 and βarr2. Data are presented as means ± SEM from at least three experiments. One-way ANOVA with Dunnett's post hoc analysis; ****P < 0.0001. See also S1-S4, S6-S8.

Figure 2. Dose-Dependent Influence of Modulators on Agonist-Promoted β-Arrestin Recruitment to Activated GPCRs. (**A-D**) Dose-dependent inhibition of agonist-promoted βarr2 recruitment to the β_2V_2R following a 30-minute pretreatment with indicated concentratios of compounds (A) 5, (B) 30, (C) 46, and (D) 64. Each compound significantly reduced the maximal βarr2 recruitment response induced by ISO. The percent reductions in maximal efficacy (E_{max}) at 50 μM for each modulator were 77%, 85.5%, 77%, and 75%, respectively. (**E**) PathHunter assay assessing βarr2 recruitment to the AT_1R in CHO-K1 cells overexpressing ProLink-tagged AT_1R and EA-tagged βarr2 similar to the β_2V_2R assay. Cells were pretreated with 50 μM of each βarr2 modulator for 30 minutes prior to stimulation with angiotensin II (AngII) for 1 hour. The left panel presents dose-response curves for AngII stimulation with either modulator or control treatment. The right panel quantifies maximal efficacy (E_{max}) in the presence of each modulator relative to the vehicle control (set at ~100%). (**F**-**H**) NanoBiT luciferase assay of βarr1/2 recruitment to V_2R. (F) Schematic illustration of βarr1/2 recruitment using the NanoBiT luciferase assay. This assay involves the co-expression of SmBiT-fused βarr1/2 and LgBiT-fused V_2R in βarr1/2-deficient HEK293 cells. Recruitment of βarr1/2 in response to AVP (100 nM) ligand stimulation was monitored, with modulators applied at 50 μM 30 minutes before the start point (0 min). (**G** and **H**) Luminescence kinetics (upper panels) and area under the curve (A.U.C) quantifications (lower panels) for NanoBiT-assessed recruitment of (G) βarr1 and (H) βarr2. Data are presented as means ± SEM (n = 3) and normalized to the vehicle control (set at 100%). One-way ANOVA with Dunnett's post hoc analysis; ****P < 0.0001. See also S9.

Figure 3. β-Arrestin Modulators Decrease Agonist-Induced Receptor Desensitization. (**A**) Diagram of the intramolecular EPAC2-FRET-based cAMP

biosensor (CFP-Epac2-YFP), which measures cAMP levels. The binding of cAMP to Epac2 induces a conformational change that increases the distance between CFP and YFP, resulting in a reduced FRET signal. (**B**) Kinetic profiles were obtained from HEK293 cells endogenously expressing the Gs protein-coupled β_2AR and stably expressing the cAMP sensor (CFP-Epac2-YFP). Cells were pre-incubated with 40 μM of the indicated modulator or DMSO (vehicle) for 5 minutes, followed by stimulation with ISO (10 μM). (**C**) Summary of cAMP responses, represented as the area under the curve (A.U.C) of the % ISO FRET reciprocal ratio (set as 100%), demonstrating that βarr modulators enhance cAMP production. (**D**) Schematic of agonist-induced $G\alpha_q$ protein-coupled AT_1R-mediated calcium mobilization from intracellular stores. (**E**-**J**) Real-time measurements of calcium mobilization were conducted as follows: (E) stable expression of AT_1R in HEK293 cells, (G) transient expression of AT_1R in parental HEK293 cells, and (I) transient expression of AT_1R in CRISPR/Cas9 β-arrestin 1/2 knockout HEK293 cells. Cells were pre-incubated with 10 μM of the indicated modulator or vehicle for 30 minutes, followed by AngII stimulation (30 pM in E; 120 pM in G and I). (**F**, **H**, and **I**) Calcium responses (A.U.C) are expressed as a percentage of AngII alone (set as 100%). Red dots indicate the phosphorylated C-terminus of the receptor (A and D). Red dots indicate the phosphorylated C-terminus of the receptor (A and D). Data are shown as means ± SEM (n = 8). One-way ANOVA with Dunnett's post-hoc analysis; ns, not significant; ***$P < 0.001$; ****$P < 0.0001$.

Figure 4. Dose-Dependent Effects of Modulators on Agonist-Induced β-arrestin-Mediated Receptor Internalization. (**A**) Schematic representation of the PathHunter activated receptor endocytosis assay. Agonist stimulation of untagged GPCR promotes recruitment of EA-tagged βarr2, leading to internalization of the GPCR-βarr2-EA complex into PK-tagged endosomes and subsequent complementation of PK and EA. (**B**-**E**) PathHunter U2OS cells were treated with increasing concentrations of each modulator for 30 minutes and then stimulated with ISO. Cmpd-5 (B), Cmpd-30 (C), Cmpd-46 (D), and Cmpd-64 (E) significantly inhibited ISO-induced receptor internalization, with percent reductions in Emax at 25 μM of 93.2 ± 1.0%, 93.4 ± 0.7%, 88.0 ± 0.8%, and 87.1 ± 0.8%, respectively. (**F**) Illustration of the BRET-based assay for

monitoring receptor association with early endosomes. (**G** and **H**) HEK293T cells transiently expressing V_2R-RlucII and 2xFYVE-mVenus were pretreated with βarr modulators (40 μM) for 30 minutes, followed by stimulation with increasing concentrations of AVP. An increase in the net BRET ratio indicates enhanced association of V_2R-RlucII with early-endosome-associated 2xFYVE-mVenus. Modulators reduced receptor association with early endosomes. Red dots denote the phosphorylated C-terminal portion of the receptor (A and F). Data are expressed as mean ± SEM from three independent experiments performed in duplicate. One-way ANOVA with Dunnett's post-hoc test; ***P* < 0.01; ****P* < 0.001; *****P* < 0.0001.

Figure 5. Effects of β-arrestin Modulators on βarr-Mediated Signaling and Physiological Functions. (**A**-**C**) Influence of modulators (30 μM) on βarr-dependent ERK phosphorylation. (**A**) Cartoon model showing βarr scaffolding between the agonist-activated phosphorylated receptor and components of the RAF–MEK–ERK MAPK pathway, leading to ERK activation (Noma *et al.*, 2007; Wisler *et al.*, 2007). Lower panel, βarr-dependent ERK1/2 activation in HEK293 cells stably expressing β_2AR, stimulated with the βarr-biased ligand carvedilol (Carv; 10 μM). (**B**) Effects of indicated modulators (30 μM) on βarr-dependent ERK phosphorylation via β_2AR stimulation with Carv (10 μM). Top panel: Western blot quantification of pERK1/2 as a percentage of maximal activity observed with Carv alone. Bottom panel: Representative western blots showing p-ERK1/2 and t-ERK1/2 signals. (**C**-**E**) βarr modulators impair chemokine-induced T cell migration. Mouse lymphocytes were pre-incubated with vehicle (control) or βarr modulator (10 μM or 20 μM) for 30 minutes at 37°C, then allowed to migrate towards the CCR7 agonist CCL19 (100 nM) for 2 hours. Graphs represent the mean percentage of migrated of (**C**) total T cells ($CD45^+$ and $CD3^+$), (**D**) T helper cells ($CD45^+$, $CD3^+$, and $CD4^+$), or (**E**) cytotoxic T cells ($CD45^+$, $CD3^+$, and $CD8^+$). Experiments were performed at least three times for B, and three times in triplicate for C-E. One-way (in B) and two-way (in C-E) ANOVA with Dunnett's post-hoc test; **P* ≤ 0.05; ****P* < 0.001; *****P* < 0.0001 (ANOVA). See also S11-S14.

Figure 6. Cmpd-5 Binding in the Central Crest Region of βarr1 within the MCL Cleft. (**A**) Cryo-EM density map of βarr1 (green) bound to Cmpd-5 (cyan) post-processed with DeepEMhancer (Sanchez-Garcia et al., 2021). Map contour level: 0.03. The overall density map also includes the BRIL fusion protein (yellow) and anti-BRIL Fab (BAG2, blue) (Mukherjee *et al.*, 2020). (**B**) Cmpd-5 binding site in the central crest of βarr1, formed by the middle loop, C-loop, and lariat loop (MCL cleft). Key residues are shown as sticks. Map contour level: 0.05. (**C**) Close-up view of the Cmpd-5 binding site in the MCL cleft, with key residues labeled. Cmpd-5 is shown in cyan, divided into three moieties for convenience: dimethylcyclohexanol (R1), oxabicyclo[2.2.2]octane-diol (R2), and 8-hydroxy-7-methylenebicyclo[3.2.1]octan-6-one (R3). Adjacent hydrophobic and hydrophilic side chains within the MCL cleft are highlighted. (**D**) Close-up of interactions between βarr1 (orange) and Cmpd-5 (cyan). Probable hydrogen bonds, inferred from structural data, MD simulations, and mutagenesis studies, are indicated by dashed gray lines. (**E**) MD simulation frames at regular intervals showing stable Cmpd-5 binding in the MCL cleft (orange), consistent with the cryo-EM structure. The frames illustrate how Cmpd-5 induces conformational changes in the middle loop, lariat loop, C-loop, and finger loop while remaining stably bound despite the flexibility shown by multiple poses. (**F**) Functional analysis of residues within the Cmpd-5 binding site in the MCL cleft of βarr1. The impact of residue mutations on the inhibition of βarr1 by Cmpd-5 was evaluated using ^{3}H-Fen binding assays *in vitro* as described in methods section. Inhibition of wild-type βarr1 on high-affinity β_2V_2R binding was approximately 40%. Data are presented as mean ± SEM from at least four experiments, with significance determined by one-way ANOVA and Dunnett's test. (**G**) ITC binding measurements for Cmpd-5 with βarr1-WT and mutants. Representative plots of raw injection heats (inset) and binding isotherms for βarr1–Cmpd-5 are shown. Equilibrium dissociation constants (K_D) are presented as mean ± SEM from three independent measurements obtained by fitting the data to a one-site binding model. (**H**) Sequence alignment of MCL cleft residues forming the Cmpd-5 binding site in βarr1 and βarr2 from *Rattus norvegicus*. Residues with potentially strong interactions are colored red, while those with weaker or possibly indirect interactions are colored pink. See also S15-S22.

Figure 7. Structural Insights into Cmpd-5–Mediated Allosteric Inhibition of βarr1. (**A**) Structural comparison of the Cmpd-5-bound βarr1 (orange) cryo-EM structure with the apo-state βarr1 (deep teal), superimposed by their N domains. Cmpd-5 is shown in cyan. While the overall structural fold is similar, Cmpd-5 binding induces an 8° interdomain twist, resulting in a poorly resolved finger loop. This twist locks βarr1 in a unique conformation that cannot further bind the receptor or transition to an active state, effectively creating a dead-end conformation. (**B** and **C**) Comparison of the (B) middle loop and C-loop, and (C) lariat loop in the MCL cleft region of the central crest of βarr1. Cmpd-5 binding induces a conformational rearrangement, shifting the (B) middle loop towards the N domain and causing (C) a helix-to-loop transition in the lariat loop (residues 282-285). These changes are highlighted by black arrows, indicating the direction of the structural shifts. **(D)** Close-up view: Cartoon representation showing an overlay of the cryo-EM structure of βarr1 (orange) bound to Cmpd-5 (cyan) with the V_2Rpp-bound βarr1 complex (magenta, PDB code: 4JQI), highlighting the conformational differences induced by Cmpd-5 binding at the MCL cleft relative to the V_2Rpp-bound state. See also S23 and S24.

STAR Methods

Key Resources Table

Lead Contact and Materials Availability

Requests for resources, reagents, and additional materials should be directed to the lead contact (lefko001@receptor-biol.duke.edu) and will be provided upon execution of a materials transfer agreement.

Experimental Model and Subject Details

Mammalian cells. HEK-293 cells (ATCC), including transient and stable experimental lines, as well as HEK293 CRISPR/Cas9 βarr1/2 knockout (KO) and parental lines (Namkung et al., 2016), were maintained at 37°C with 5% CO_2 and cultured in Eagle's MEM supplemented with 10% FBS and 1% pen–strep. U2OS cell lines (DiscoveRx PathHunter) were cultured in MEM with 2 mM L-glutamine, 1% pen–strep, and 10% FBS, maintained at 37°C in 5% CO_2. U2OS cells used for βarr recruitment or receptor/βarr internalization assays followed the manufacturer's protocol (DiscoveRx,

Fremont, CA). For chemokine-induced cell migration assays, leukocytes were isolated from wild-type mice as described (Namkung *et al.*, 2016; Rein *et al.*, 2017; Smith *et al.*, 2018b).

Bacterial cells. E. coli strains DH5α and BL21 (NEB) were cultured in LB or TB media (Fisher Scientific) at 37°C. DH5α (in LB) was used for plasmid generation and amplification, while BL21 (in TB) was used for protein expression.

Insect cells. *Sf9* (*Spodoptera frugiperda*) cells (Expression Systems, catalog no. 94-001F) were cultured in ESF 921 medium (Expression Systems, Davis, CA) at 27°C. Baculoviruses were generated and amplified in ESF 921 medium according to the manufacturer's instructions.

Cell Culture, Antibodies, and Reagents

For cell starvation experiments, a serum-free medium supplemented with 0.1% BSA, 10 mM HEPES, and 1% penicillin-streptomycin was used. Transient transfections were performed with FuGene 6 (Promega, Madison, WI) and Lipofectamine 3000 (Invitrogen), following the manufacturers' instructions. Monoclonal anti-FLAG M2-HRP (A8592) and monoclonal anti-ERK1/2 (ABS44) antibodies were obtained from Sigma-EMD Millipore. Anti-Rabbit IgG, HRP-linked $F(ab')_2$ fragment (from donkey) NA9340-1ML, and Anti-Mouse IgG, HRP-linked $F(ab')_2$ fragment (from sheep) (NA9310-1ML), Amersham ECL secondary antibodies were obtained from Cytiva. cOmplete^{TM} protease inhibitor tablets (catalog no. 11836153001) and PhosSTOP^{TM} phosphatase inhibitor tablets (catalog no. 4906837001) were purchased from Roche (Basel, Switzerland). The MEK1/2 inhibitor U0126 *(Favata et al., 1998)* was sourced from Selleckchem (catalog no. S1102). Anti–phospho-p44/42 MAPK (ERK1/2) (Thr202/Tyr204) antibody (9101L) was purchased from Cell Signaling Technology. A rabbit polyclonal anti-βarr1/2 antibody (A1CT), which recognizes both βarr1 and βarr2 isoforms, was generated in the laboratory of R. J. Lefkowitz (Duke University, Durham, NC) (Attramadal et al., 1992).

Recombinant Protein Expression and Purification

The expression and purification of βarrs have been described previously (Cahill et al., 2017; Nobles et al., 2007; Shukla *et al.*, 2013; Shukla *et al.*, 2014). Briefly, *E. coli* BL21 (DE3) pLysS cells (New England Biolabs: C2527I) carrying pGEX4T1- *Rattus norvegicus* βarr1 or 2 construct, with their C-terminal truncated (at amino acid 393 or at 394, respectively), were cultured in Terrific Broth (Teknova, Hollister, CA) medium at 37°C. After OD_{600} reached 0.6–0.8, the cells were induced with 0.1 mM isopropyl-β-D-thiogalactopyranoside (IPTG) at 18°C overnight. Bacteria were harvested by centrifugation (4000 RPM), and cell pellets were resuspended in lysis buffer [20 mM HEPES, pH 8, 150 mM NaCl, 10% glycerol, 1 mM EDTA, 0.2 mM dithiothreitol (DTT), 1 mM phenylmethylsulfonyl fluoride, and 1 mM benzamidine] at 4°C for 1 hr. Cell suspensions were sonicated, centrifuged (14,000 RPM, 30 min, 4°C), and the supernatant was loaded onto pre-equilibrated Glutathione-agarose resin (GoldBio). After 3 hours of binding at 4°C, the beads were washed, and thrombin was added for overnight cleavage. The proteins were further purified by anion exchange chromatography followed by size exclusion chromatography (SEC) using a Superdex 200 Increase 10/300 GL column on an ÄKTA FPLC system (GE Healthcare). Eluted fractions were analyzed by SDS–PAGE, pooled, concentrated using 30 kDa MWCO Amicon Ultra-15 Centrifugal Filter devices, flash-frozen in liquid nitrogen, and stored in aliquots at −80°C. The same rat βarr1 constructs with mutations (L129A, L129S, L129G, P131A, P133A, E134A, D135A, K138A, C140A, Y249A, C251A, E283A, K284A, R285A) were generated and purified in a similar manner (**Table S3**). Fab30 was expressed and purified as previously described (Cahill *et al.*, 2017; Rizk et al., 2011). Briefly, Fab30 was expressed in the periplasm of E. coli M55244, extracted, and purified using protein A/G agarose (Pierce). Elution was carried out with 10 mM sodium acetate (pH 3.0) and 100 mM NaCl, then neutralized with lysis buffer [20 mM HEPES, pH 8.2, 150 mM NaCl]. Fab30 was subsequently purified on a Resource S column, followed by dialysis in 20 mM HEPES (pH 7.4) with 100 mM NaCl. Protein concentrations for each protein were determined by ultraviolet absorption at 280 nm and extinction coefficients estimated using the ExPASy ProtParam tool (Wilkins et al., 1999).

Expression and Purification of Chimeric β_2-Adrenergic Receptor.

The N-terminal FLAG-tagged T4 Lysozyme fusion-β_2V_2R chimeric receptor (comprising β_2AR residues 1-341 and V_2 vasopressin receptor residues 328-372), with a tobacco etch virus (TEV) cleavage site, was co-infected with GRK2-CAAX (GRK2 with a membrane-tethering prenylation signal) in Sf9 insect cells using the Baculovirus Expression System, as previously described (Cahill *et al.*, 2017; Kahsai *et al.*, 2016; Kahsai *et al.*, 2011; Shukla *et al.*, 2013; Shukla *et al.*, 2014). At 66 hours post-infection, cells were harvested following stimulation with 20 μM isoproterenol at 37°C for 20 minutes to induce receptor phosphorylation, generating the T_4L fusion phosphorylated-β_2V_2R, referred to as $p\beta_2V_2R$ in this study (Asher *et al.*, 2022; Cahill *et al.*, 2017; Shukla *et al.*, 2014). Cells were extensively washed to remove any residual isoproterenol used for phosphorylation, preparing them for in vitro assembly of GPCR–βarr1 complexes, as described below. For membrane preparation from these cells, briefly, cells were resuspended in cold homogenization buffer (75 mM Tris-HCl, pH 7.4, 2 mM EDTA, and cOmplete™ protease inhibitor) and collected by centrifugation at 500 × g for 5 minutes at 4°C. After two additional rounds of centrifugation at 500 × g for 5 minutes at 4°C, the supernatant was centrifuged at 21,000 × g for 30 minutes at 4°C to collect crude membrane fractions. Pellets were then washed with resuspension buffer (75 mM Tris-HCl, pH 7.4, 2 mM EDTA, 12.5 mM $MgCl_2$, cOmplete™ protease inhibitor, and PhosSTOP™ phosphatase inhibitor), passed through a 0.4 mm gauge needle 30 times using a syringe on ice, aliquoted, flash-frozen in liquid nitrogen, and stored at −80°C.

Small Interfering RNA (siRNA) Silencing of β-arrestin Expression

Knockdown of the expression levels of βarr1/2 was performed as described and functionally validated previously (Luttrell *et al.*, 2018; Wang *et al.*, 2017). A non-silencing siRNA duplex sequence (5′-AAUUCUCCGAACGUGUCACGU-3′) was also used as a negative control. HEK293 cells stably expressing FLAG-tagged β_2AR were seeded into a 10 cm dish on the day before to reach 40–50% confluence at the time of transfection. Transfections of siRNA of βarr1/2 or control siRNA were conducted by using GeneSilencer siRNA Transfection reagent (Genlantis) according to the manufacturer's protocol. In brief, to a 20 μg siRNA and 240 μL siRNA dilution buffer mixture, 180 μL serum-free medium was added. In parallel, 51 μL of transfection

reagent was mixed with 300 μL serum-free medium. Both solutions were allowed to stand for 5 min at room temperature, then combined and incubated for an additional 20 min. The mixture was then added to cells in the 100 mm dish with a 4 mL serum-free medium. After 4 h incubation at 37 °C and 5% CO_2, 5.5 ml of MEM containing 20% FBS and 2% penicillin–streptomycin was added to the dish. About 48 hours later, the cells were split and seeded into 6-well dishes. ERK activation assay was performed 3 days after transfection.

Small Molecule Library and Reagents

A collection of structurally diverse, drug-like small-molecule libraries used in this work was obtained from the NCI/DTP Open Chemical Repository. The compound library comprised approximately 3.5K compounds, representing the structural diversity of over 250K unique small molecules. This DTP library included the NCI Diversity Set, natural products, and FDA-approved oncogenic drugs. Most compounds were certified as >95% pure by the supplier (NCI DTP Discovery Services). Powdered compounds were dissolved in 100% dimethyl sulfoxide (DMSO) and stored at −20°C. Isoproterenol (Sigma, I2760-1G), ICI-118,551, Carvedilol, angiotensin II (AngII; Sigma, A9525), and human epidermal growth factor (EGF) were purchased from Sigma-Aldrich, and [Arg8]-Vasopressin (AVP) was obtained from GenScript. All small molecule compounds, including BI-167107 (Rasmussen et al., 2011), were dissolved in DMSO and stored at −20°C as 100 mM stock solutions. The C-terminal peptide of the GPCR vasopressin-2 receptor (V_2R), known as V_2Rpp, was synthesized by the Tufts University Analytical Core Facility. Cellular agonist stimulations were performed at 37°C, as described in the figure legends.

Differential Scanning Fluorimetry (DSF)

A high-throughput differential scanning fluorimetry (DSF) assay was performed to identify βarr-binding small molecules from the drug-like compound library (DDLC) described above. The screen was conducted using the StepOnePlus™ Real-Time PCR System (Applied Biosystems) with the fluorescent reporter probe SYPRO Orange (Thermo Fisher Scientific) in a 96-well format. Proteins were buffered in 20 mM HEPES

(pH 7.5) with 100 mM NaCl. Small molecules (100 μM) were screened with either βarr1 or βarr2 (5 μM). DMSO was used as a vehicle control, while V_2Rpp (50 μM) served as a positive control.

For DSF experiments involving the three positive control ligands (V_2Rpp, IP_6, and Heparin, each at 50 μM) binding to βarrs, HEPES buffer was used as the vehicle control. Excitation and emission filters for SYPRO Orange were set to 475 nm and 580 nm, respectively. The temperature was increased by 0.5°C every 30 seconds, from 25°C to 99°C, with fluorescence readings taken at each interval. Raw DSF data were analyzed using Applied Biosystems® Protein Thermal Shift™ Software. Fluorescence intensities were plotted as a function of temperature, and the midpoint of transition, or melting temperature (T_m), was calculated by plotting the first derivative of fluorescence emission as a function of temperature (dF/dT). The difference between the Tm of the protein-ligand complex and that of the protein alone represents the thermal shift (ΔT_m), which indicates ligand binding to the protein of interest. For statistical analysis, experiments were conducted with at least three independent replicates per condition. The final selection of compounds for this study was guided by their efficacy in inhibiting βarr1/2 activity, along with favorable chemical properties, such as aqueous solubility and permeability, as described in the Results section. Four compounds were selected as candidate inhibitors: Cmpd-5 (NSC250682), (1S,4aR,5S,6S,6aR,9S,11aS,11bS,14R)-1,5,6,14-tetrahydroxy-4,4-dimethyl-8-methylenedecahydro-1H-6,11b-(epoxymethano)-6a,9-methanocyclohepta[a]naphthalen-7(8H)-one (Cayman Chemical; 25665); Cmpd-30 (NSC622608), (Z)-3-((furan-2-ylmethyl)imino)-N,N-dimethyl-3H-1,2,4-dithiazol-5-amine, hydrobromide; Cmpd-46 (NSC302979), (Z)-3-ethoxy-6-hydroxy-4,4,13a-trimethyl-9-methylene-1,2,3,4,4a,5,6,9,10,11,12,13a-dodecahydro-7,10-(metheno)benzo[11]annulene-8,13-dione; and Cmpd-64 (NSC22070), (Z)-4,10a-dimethyl-7-methylene-8-oxo-1a,2,3,6,6a,7,8,9a,10,10a decahydrooxireno[2',3':8,9]cyclodeca[1,2-b]furan-6-yl acetate.

Measurement of β-arrestin Recruitment Using the PathHunter Assay

βarr recruitment to the agonist-activated receptor (β_2V_2R) was measured using the DiscoveRx PathHunter β-arrestin assay (Ahn *et al.*, 2017), which employs enzyme

fragment complementation. In this assay, the β_2V_2R is fused to an inactive portion of β-galactosidase (ProLink™ tag), and βarr2 is fused to the complementary Enzyme Acceptor (EA) portion, each stably expressed in U2OS cells. Upon agonist-induced recruitment of βarr2 to β_2V_2R, the β-gal fragments complement to form a functional enzyme, generating a measurable chemiluminescent signal. The signal intensity correlates directly with the extent of βarr2 recruitment. U2OS cells co-expressing β_2V_2R and βarr2 were plated at a density of 25,000 cells per well in white, clear-bottom 96-well plates 24 hours before treatment. On the day of the experiment, cells were treated with either a single dose (50 μM) or varying concentrations of a specific βarr modulator or vehicle control in Hanks' balanced salt solution (Sigma-Aldrich) with 20 mM HEPES (pH 7.4) and 0.05% BSA. Cells were incubated at 37°C, 5% CO_2, and ~100% relative humidity for ~30 minutes, followed by stimulation with either 10 nM isoproterenol (ISO) or a serial dilution of ISO for 60 minutes at 37°C. After agonist stimulation, PathHunter reagents were added, and cells were incubated for another 60 minutes at ambient temperature. Luminescence signals were measured using a CLARIOstar microplate reader (BMG Labtech).

Measurement of β-arrestin Recruitment Using the NanoBiT Assay

To elucidate the effects of compounds on the individual interactions of βarr1 and βarr2 with the receptor, NanoLuc Binary Technology (NanoBiT) assays were performed using HEK293 CRISPR/Cas9 βarr1/2 knockout (KO) cells transiently transfected with pcDNA 3.1 V_2R-LgBiT for the receptor and either pcDNA 3.1 βarr1-SmBiT or pcDNA 3.1 βarr2-SmBiT constructs. In this NanoBiT βarr recruitment assay, the SmBiT tag was placed on the N-terminus of human βarr1/2, and the LgBiT tag was fused to the N-terminal region of human V_2R, which also included an HA signal sequence and a FLAG tag (DYKDDDDK) on the N-terminus of V_2R, as previously described (Daly *et al.*, 2023; Dixon *et al.*, 2016; Pandey *et al.*, 2021). Cells were plated at a density of 100,000 cells per well in a white, clear-bottom 96-well plate one day before transfection. The transfection solution was prepared by combining V_2R-LgBiT and either βarr1-SmBiT or βarr2-SmBiT constructs in a 1:5 ratio (25 ng of receptor and 125 ng of βarr1/2). Transfections were performed using Lipofectamine 3000 (Invitrogen, catalog

#L3000015) according to the manufacturer's instructions. Forty-eight hours post-transfection, cells were washed and incubated in Opti-MEM™ for 60 minutes at 37°C before conducting NanoBiT assays. Coelenterazine-h and one of the modulators (compounds 5, 30, 46, or 64) were added to cells at a final concentration of 50 μM, approximately 30 minutes prior to measurement. After establishing a baseline response for 2 minutes, cells were stimulated with 100 nM AVP or vehicle, and luminescence was measured for an additional 20 minutes. The complemented (SmBiT + LgBiT) NanoLuc signals were detected at 550 nm using a PHERAstar FSX instrument (BMG LabTech). Ligand-induced changes in luminescent units were normalized to baseline and vehicle, and the area under the curve (AUC) for the entire time course was calculated to determine the cumulative agonist-induced response and modulator effects. This approach allowed for a robust determination of the maximal effect of modulators on βarr1/2 recruitment to AVP-activated V_2R.

Pull-Down of *In Vitro* GPCR–βarr Complexes

The effect of the modulators on the assembly of receptor–βarr complex *in vitro* was assessed by pull-down assay using the T_4L-pβ_2V_2R–βarr1–Fab30 complex as described previously (Shukla *et al.*, 2014). Briefly, Sf9 cells expressing FLAG-tagged phosphorylated T_4L-β_2V_2R (phosphorylated via agonist stimulation and co-expressed GRK2-CAAX) were lysed by Dounce homogenizer. Subsequently, Fab30 (1 μM) and βarr1 (500 nM), pre-equilibrated with βarr modulators (50 μM), IP_6 (50 μM), or vehicle, were added to the homogenate. The pβ_2V_2R–βarr1–Fab30 complex was solubilized in buffer containing 20 mM HEPES, 150 mM NaCl, pH 7.4, 0.5% MNG, 2.5 μM BI-167107. After removal of insoluble material by centrifugation, the supernatants were added to 30 μL of anti-FLAG M1 agarose beads. After an additional one hour of incubation at room temperature, the beads were washed three times with wash buffer (20 mM HEPES, 150 mM NaCl, pH 7.4, 0.01% MNG, 1 μM BI-167107) and eluted with buffer containing 0.5 mg/mL FLAG peptide. Finally, FLAG-pβ_2V_2R and associated βarr1 in the complex of pβ_2V_2R–βarr1–Fab30 were analyzed by western blotting using HRP-conjugated anti-FLAG M2 antibody (Sigma, 1:4000) and anti-βarr1/2 A1CT antibody (1:2,500).

FRET-Based cAMP Accumulation Measurement

To measure cellular cAMP production in live cells mediated by stimulatory G protein, Gαs-coupled β_2AR activation, FRET-based Epac sensors were used as described previously (Violin et al., 2008). The Epac2 (ICUE2) sensor contains a CFP and YFP FRET pair. HEK293 cells stably expressing ICUE2 were plated in poly-D-lysine-coated, black, clear-bottom 96-well plates (Corning) at a density of 50,000 cells per well. At least 16 hours after plating, cells were washed with PBS and incubated in HEPES-buffered saline solution (10 mM HEPES, 150 mM NaCl, 5 mM KCl, 1.5 mM $MgCl_2$, 1.5 mM $CaCl_2$, 10 mM glucose, 0.2% BSA, pH 7.4) for one hour at 37°C. Cells were then treated with either βarr small-molecule modulators (40 μM) or DMSO for 5 minutes, and baseline fluorescence was monitored. Real-time cAMP measurement was initiated by stimulating cells with 10 μM isoproterenol (ISO) at 37°C. FRET changes corresponding to cAMP accumulation were measured as changes in the background-subtracted 480 nm/535 nm fluorescence emission ratio (CFP/YFP), reflecting changes in cAMP levels. The entire cAMP accumulation profile was quantified by calculating the area under the curve (AUC) for the time course. To assess the effect of modulators on the agonist-induced cAMP response, AUC values were expressed as a percentage of the response to ISO in the presence of DMSO (set as 100%), enabling comparison of the effect of each modulator relative to this agonist-alone control.

Intracellular Calcium Measurement

Intracellular [Ca^{2+}] release was measured using the FLIPR Calcium 6 assay kit with a FlexStation 3 microplate reader, following the manufacturer's instructions (Molecular Devices, LLC) and as describer previously (Li *et al.*, 2023). Briefly, HEK293 cells stably expressing human Angiotensin II type 1 receptor (AT_1R), parental HEK293 cells transiently expressing AT_1R, or HEK293 CRISPR/Cas9 βarr1/2 KO cells transiently expressing AT_1R were seeded in poly-D-lysine-coated, black 96-well assay plates at a density of 40,000 cells per well and incubated for 24 hours. On the day of the experiment, cell plates were loaded with FLIPR Calcium 6 reagents and treated with βarr small-molecule modulators (10 μM) or vehicle (DMSO) for 30 minutes. After

establishing basal fluorescence (F_0), the cells were treated with the agonist AngII (30 pM for stably expressing AT1R or 120 pM for transiently expressing AT_1R) while fluorescence (F) intensity was monitored in real time. The entire calcium transient profile was quantified by calculating the area under the curve (AUC) for the time course. To assess the effect of modulators on the agonist-induced Ca^{2+} responses, AUC values were expressed as a percentage of the response to AngII in the presence of buffer alone (set as 100%), enabling comparison of each modulator's effect relative to this agonist-alone control.

Measurement of Receptor Internalization by PathHunter Assay

βarr-mediated receptor internalization was measured using the DiscoveRx PathHunter active receptor endocytosis assay according to the manufacturer's protocol (DiscoveRx, Fremont, CA) and as previously described (Ahn *et al.*, 2017). Briefly, β_2V_2R was transiently transfected into U2OS cells stably expressing an Enzyme Acceptor (EA)-tagged βarr2 and an endosome-localized ProLink-tagged protein. The next day, cells were seeded at 25,000 cells per well in white, clear-bottom 96-well assay plates and incubated for 24 hours before the experiment. On the day of the experiment, cells were treated with varying concentrations of a specific βarr modulator or vehicle control in Hanks' balanced salt solution (Sigma-Aldrich) with 20 mM HEPES (pH 7.4) and 0.05% BSA. Cells were incubated at 37°C, 5% CO_2, and ~100% relative humidity for ~30 minutes, followed by stimulation with a series of concentrations of agonist (ISO) for 60 minutes at 37°C. After agonist stimulation, PathHunter reagents were added, and cells were incubated for another 60 minutes at ambient temperature. Receptor–βarr complex internalization was detected as luminescence resulting from the complementation of β-gal fragments (Enzyme Acceptor and ProLink) within endosomes. Luminescence signals were measured using a CLARIOstar microplate reader (BMG Labtech).

BRET Based Receptor Internalization Assay

BRET-based assays were conducted to measure receptor internalization using a bystander BRET format as previously described (Smith *et al.*, 2017). Briefly, HEK293 cells transiently expressing V_2R-RLucII (BRET donor) and the early endosome marker

2xFYVE-mVenus (BRET acceptor) were pretreated with vehicle or βarr modulator (40 μM) for 30 minutes. Receptor association with the endosome marker was measured as a BRET signal after stimulation with a range of AVP concentrations. BRET measurements were performed using the Synergy2 (BioTek®) microplate reader with filter sets of 410/80 nm and 515/30 nm to detect RLucII (donor) and mVenus (acceptor) emissions, respectively. The BRET signal was calculated as the ratio of light intensity emitted by the acceptor over the donor, and the 'net BRET' ratio was determined by subtracting the vehicle control ratio from the corresponding AVP-treated ratio.

Chemotaxis Assays

Chemotaxis assays were performed similarly to previously described protocols (Smith *et al.*, 2018b). Briefly, murine T cells were isolated from the spleens of wild-type mice, subjected to erythrocyte lysis, and filtered through a 70-μm filter. The cells were then suspended in RPMI 1640 medium containing 0.5% BSA and treated for 30 minutes with βarr modulators or vehicle. A total of 1 × 10□ cells in 100 μL of medium were added to the upper chamber of 6.5-mm diameter, 5-μm pore polycarbonate Transwell filters (Corning Costar), and cells migrated toward 100 nM CCL19 in the lower chamber for 2 hours at 37°C. T cells that migrated to the lower chamber were collected, resuspended, washed, and stained for flow cytometry analysis using a Live/Dead marker (Aqua Dead, ThermoFisher) and antibodies for cell surface markers ($CD45^+$, $CD3^+$, $CD4^+$, and $CD8^+$) prior to paraformaldehyde fixation. The total live T cell population (CD45+ and CD3+) and subset populations ($CD45^+$, $CD3^+$, and $CD4^+$, or $CD45^+$, $CD3^+$, and $CD8^+$) were measured using a BD LSR Fortessa machine from the Flow Cytometry Shared Resource (FCSR) at the Duke Cancer Institute (Durham, NC). CountBright beads (ThermoFisher) were added immediately after resuspension of the lower chamber contents to correct for volume differences and any cell loss during wash steps. Percent migration was calculated by determining the percentage of migrated cells treated with compounds relative to control wells, with migration in CCL19-treated wells alone set as 100%. A representative gating tree is shown in **Figure S14**.

Isothermal Titration Calorimetry

Isothermal Titration Calorimetry (ITC) measurements were performed on a MicroCal iTC200 system (Malvern, PA) at 25°C. Prior to ITC experiments, all proteins (βarr1, βarr2, or βarr1 mutants) were extensively dialyzed against 20 mM HEPES (pH 7.4), 100 mM NaCl, and 3 μM TCEP. Protein concentrations were determined by spectrophotometry at 280 nm, using extinction coefficients calculated from each protein sequence via the ProtParam program (Wilkins *et al.*, 1999). The dialysis buffer was used to dilute DMSO stock solutions of βarr small molecule modulators to their final concentrations for measurements. For each ITC experiment, βarr modulators (Cmpd-5 at 350 μM, Cmpd-30 at 200 μM, Cmpd-46 at 450 μM, and Cmpd-64 at 450 μM) were loaded into the syringe and titrated into the calorimetric cell containing βarr1, βarr1 mutants, or βarr2 (at approximately 30 μM, 20 μM, 40 μM, and 40 μM respectively, for each modulator). The reference cell was filled with distilled water. In all experiments, the titration sequence typically consisted of an initial 0.4 μl injection, followed by 19 injections of the βarr modulator compound at 2 μl each, with a 180-second interval between injections to allow thermal power to return to baseline. During the experiment, the reference power was set to 7 $\mu cal \cdot s^{-1}$, and the sample cell was stirred continuously at 750 rpm. Raw data, excluding the peak from the first injection, were baseline-corrected, integrated, and normalized. Data were analyzed and fit using a one-site independent-binding model to obtain the equilibrium dissociation constant, K_D (from the association constant $K_A=1/K_D$), stoichiometry (N), and thermodynamic parameters such as enthalpy (ΔH) and entropy (-TΔS) of binding. Data were analyzed using MicroCal PEAQ-ITC analysis software (version 1.1.0.1262, Malvern, PA).

Radioligand Binding Experiments

To determine the influence of small-molecule βarr modulators on βarr-promoted high-affinity agonist binding receptor state *in vitro*, [^{3}H]-methoxyfenoterol (^{3}H-Fen) binding experiments were performed using phosphorylated β_2V_2R ($p\beta_2V_2R$) in Sf9 insect cell membranes (Ahn *et al.*, 2017). Membranes were prepared following the procedures described above. The reaction mixture (100 μL) included $p\beta_2V_2R$ membranes, with ^{3}H-Fen (12.6 Ci/mmol) at a concentration of 6 nM, βarr1/2 or a βarr1 mutant (2 μM), and either βarr modulators (100 μM) or vehicle. Nonspecific radioligand binding was

determined in reactions that contained the antagonist propranolol (25 µM). Following a 90 min incubation at room temperature, binding assays were terminated by harvesting the reaction mixture onto PEI-soaked GF/B filters and washing three times with cold buffer (Brandel Harvester, Gaithersburg, MD). Bound ^{3}H-Fen was extracted overnight with 5 mL of scintillation fluid, quantified, and expressed as specific binding.

Cytotoxicity Assay

MTT assay was performed according to the manufacturer's instructions (Roche Diagnostics GmbH, Germany). HEK293 and U2OS cells were seeded in 96-well plates. The following day, cells were treated with the indicated concentration of modulator or vehicle for 8 h. To evaluate the cytotoxic effects of the compounds, cells were incubated with 3-(4,5-dimethylthiazol-2-yl)-2,5-diphenyltetrazolium bromide (MTT) reagent at 37 °C for 4 h. The optical density (OD) was measured at 595 nm (the absorbance of each sample was measured at 560 and 670 nm). The optical density values of blue formazan formed in live cells based on the reduction of MTT were determined at 595 nm. Cell viability was expressed as the percentage of MTT reduction in compound-treated cells compared to vehicle-treated cells.

Live Cell MAPK Activation Assay

To assess the effect(s) of small-molecule modulators on receptor-stimulated βarr dependent ERK1/2 and p38α MAPK activation, HEK293 cells stably expressing β_2AR were starved for 6 hours in serum-free medium prior to stimulation (Wang *et al.*, 2017; Wisler *et al.*, 2007). Cells were pretreated with βarr small-molecule modulators (30 µM) or vehicle, then incubated for 15 min at 37°C. The cell lysates were sonicated for 15 sec and clarified by centrifugation 14,000 x g (4°C, 15 min). Proteins were resolved on an SDS-PAGE gel, transferred to nitrocellulose membranes, and immunoblotted using rabbit polyclonal anti-phospho-p44/42 MAPK (ERK1/2) antibody (1:2000; Cell Signaling), anti-MAPK1/2 (ERK1/2) antibody (1:10,000; Millipore-Sigma), anti-p38 alpha/beta MAPK antibody (1:1,000; Santa Cruz Biotechnology), anti-phospho-p38 MAPK antibody (1:1,000; Cell Signaling), and anti-βarr1 antibody (A1CT; 1:3000). Protein bands on the membrane were detected with SuperSignal West Pico enhanced

chemiluminescent substrate (Thermo Fisher) and captured using a ChemiDoc-XRS charge-coupled device camera system (Bio-Rad Laboratories). Bands were quantified by densitometry using Image Lab (Bio-Rad, Hercules, CA), and GraphPad Prism software was used for data analyses.

For experiments involving siRNA transfection and knockdown βarrs, after stimulation, cells were lysed in ice-cold 1% NP-40 lysis buffer [20 mM tris-HCl (pH 7.4), 137 mM NaCl, 20% glycerol, 1% NP-40, 2 mM sodium orthovanadate, 1 mM phenylmethylsulfonyl fluoride, 10 mM sodium fluoride, aprotinin (10 µg/ml), leupeptin (5 µg/ml), and phosphatase inhibitors (PhosSTOP™; Roche)], rotated for 45 min, and cleared of insoluble debris by centrifugation at 14,000 x g (4 °C, 15 min). After which the supernatant was collected, protein concentration determined, and equal amounts of cell lysate were mixed with 6× Laemmli sample buffer. Samples were analyzed afterwards essentially as described above.

Cryo-EM Sample Preparation and Data Acquisition

The expression construct for βarr1-BRIL was designed by inserting the thermostabilized apocytochrome b562 (M7W, H102I, K106L) from *Escherichia coli* (BRIL) between residues 176-182 at the hinge region of rat βarr1 (Nobles *et al.*, 2007) truncated at residue 393 (**Figure S15A**) and purified as wild-type βarr1. βarr1-BRIL was incubated with 1.5-fold molar excess of anti-BRIL Fab (BAG2) (Mukherjee *et al.*, 2020) and 2-fold molar excess of anti-Fab-Nb (aFabNb) (Ereno-Orbea *et al.*, 2018) for 1 hour at room temperature. The complex was subjected to SEC on a Superdex 200 Increase column (Cytiva Life Sciences) in 20 mM HEPES 7.5, 150 mM NaCl buffer. Peak fractions were concentrated to 2 mg/ml using Vivaspin® 6 column with molecular weight cut-off of 30,000 kDa (Sartorius). The complex was incubated for 2 hours on ice with 50-fold molar excess of Cmpd-5 solubilized in DMSO (βarr1-BRIL–BAG2–aFabNB–Cmpd-5) or equivalent amount of DMSO (βarr1-BRIL–BAG2–aFabNB–Apo), and then concentrated to 7-8 mg/ml. The sample was applied to glow-discharged 300-mesh holey-carbon grids (Quantifoil R1.2/1.3, Electron Microscopy Sciences) using a Vitrobot Mark IV (Thermo Fisher Scientific) at 4 °C and 100% humidity. The data were collected on a Titan Krios

transmission electron microscope (Thermo Fisher) operating at 300 kV equipped with a K3 direct electron detector (Gatan) in counting mode with a BioQuantum GIF energy filter (slit width of 20 eV) at a magnification of ×81,000 corresponding to a pixel size of 1.08 Å at the specimen level. 60-frame movies with a dose rate of ~15 electrons per pixel per second and a total accumulated dose of ~54-60 electrons per $Å^2$ were collected using the *Latitude-S* (Gatan) single-particle data acquisition program. The nominal defocus values were set from −0.8 to −2.5 µm.

Cryo-EM Data Processing

Movies were subjected to beam-induced motion correction using Patch Motion Correction in CryoSPARC v4.0.1 (Punjani et al., 2017) followed by determination of Contrast transfer function (CTF) parameters in Patch CTF. Micrographs with CTF fit better than 3.5 Å were used for further analysis. Particles manually selected from 15 micrographs were used to train a model in the particle picking tool Topaz v0.2.5a (Bepler et al., 2019). The trained model was used to pick particles in all micrographs generating 1,572,529 particle projections for βarr1-BRIL–BAG2–aFabNB–Cmpd-5 and 1,307,318 particle projections for βarr1-BRIL–BAG2–aFabNB–Apo. The particles were rescaled to the pixel size of 1.3824 Å for further processing. A subset of particles (500,000) was subjected to Ab Initio model generation with 5 classes. All particles were then subjected to five rounds of heterogeneous refinement. The resulting particle stacks (396,911 particles for βarr1-BRIL–BAG2–aFabNB–Cmpd-5 and 650,376 particles for βarr1-BRIL–BAG2–aFabNB–Apo) were used in non-uniform refinement and local refinement with a mask excluding aFabNb and the constant region of BAG2. Then particles were subjected to 3D classification without alignment in CryoSPARC with a mask excluding aFabNb and the constant region of BAG2. Finally, the best classes with 177,430 particles (βarr1-BRIL–BAG2–aFabNB–Cmpd-5) and 479,224 particles (βarr1-BRIL–BAG2–aFabNB–Apo) were subjected to another round of local refinement in CryoSPARC, generating a map with a global resolution of 3.47 Å and 3.52 Å, respectively. The Cryo-EM maps were post-processed using DeepEMhancer with highRes deep learning model (Sanchez-Garcia *et al.*, 2021) (**Figure S16, Figure S17, Figure S21**).

Model Building and Refinement

The initial models were built manually by fitting the crystal structure of βarr1 (PDB: 1G4M) (Han *et al.*, 2001) into the experimental electron densities using UCSF Chimera v1.15 (Pettersen et al., 2004). The BRIL-BAG2-aFabNb part of the model was derived from the Cryo-EM structure of Frizzled5-BRIL-BAG2-aFabNb (PDB: 6WW2) (Tsutsumi et al., 2020). The structures were refined by combining manual adjustments in Coot v0.9.8.3 (Emsley et al., 2010) and ISOLDE (Croll, 2018) in UCSF ChimeraX 1.6.1 (Pettersen *et al.*, 2004), followed by real-space refinement in PHENIX v1.20.1-4487 (Adams et al., 2011) with Ramachandran, rotamer, torsion, and secondary structure restraints enforced. The models were validated with MolProbity v4.5.1 (Chen et al., 2010). Refinement statistics are given in **Table S1**.

Molecular modeling and simulations

The apo βarr1 model in the basal state and the β_2V_2R–βarr1 complex (PDB code: 6TKO)(Lee *et al.*, 2020) model were built and simulated as described previously (Asher *et al.*, 2022). Due to a significant number of missing residues in the Cmpd5-bound βarr1 cryo-EM structure, we constructed a Cmpd5-bound βarr1 model by placing Cmpd5 in the MCL cleft of an equilibrated basal βarr1 model according to the experimentally derived location of the bound Cmpd5. A βarr1 model in the active state was constructed by homology modeling with Modeller (v10.0) (Webb and Sali, 2016) using the crystal structure of the V_2Rpp-bound βarr1 in the active state (PDB code: 4JQI) (Shukla *et al.*, 2013) as the template. Parts without any template, i.e., residues 1 to 5 and 307 to 311 were *ab initio* modeled with Modeller. The resulting model with the lowest DOPE score was selected for the following steps. The selected βarr1 models were processed by the Protein Preparation Wizard of Schrodinger Suite (version 2023-1). The first and last residues of this model are in positively and negatively charged states, respectively, without capping, as assumed in their natural condition. The prepared model was then immersed in a simulation water box using the System Builder of Schrodinger Suite (version 2023-1). A simple point charge (SPC) water model was used to solvate the system, and $Na^{+,}$ and Cl^- ions were added to neutralize the system and the salt

concentration of the system was increased to 0.15 M. The total system size was ~148,000 atoms.

MD simulations were carried out using Desmond MD System (version 6.1; D.E. Shaw Research, New York, NY) (Bowers et al., 2006) with the OPLS4 force field (Lu et al., 2021). The simulation systems were minimized and equilibrated with restraints on the ligand heavy atoms and the protein backbone. For both the equilibrations and the following production runs, the constant temperature 310 K was maintained by Langevin dynamics, 1 atm constant pressure was achieved with the Langevin piston method (Feller et al., 1995). A cutoff distance of 9 Å was used for the nonbonded interactions, and the particle-mesh Ewald summation method was used for the electrostatics interactions. The integration timestep was set to 2.5 fs. The isothermal-isobaric (NPT) ensemble was used in a periodic boundary condition. The production runs of βarr simulations are without any restraints. The analysis and visualization were performed with VMD (Humphrey et al., 1996) and PyMol (Schrodinger).

Graphing and Statistical Analyses

All graphs were generated and analyzed using GraphPad Prism 10.0 (GraphPad Software, Inc., La Jolla, CA). Dose-response curves were fitted to a log(agonist) versus response model with parameters for span, baseline, and EC_{50}, and minimum baseline was corrected to zero. For statistical comparisons, one-way ANOVA with Dunnett's post hoc test was generally used for comparisons across more than two groups, and two-way ANOVA with Sidak's post hoc test or similar was used for comparisons involving multiple conditions, as specified in the figure legends. Most experiments were conducted with three biological replicates, and additional replicates served as controls. Replicates in the figure legends refer to biological replicates, with technical replicates included in some experiments for intra-replicate variation. Differences with *P*-values < 0.05 were considered significant. Further statistical details and replicate information are provided in the figure legends.

Data and Materials Availability: The coordinates and corresponding cryo-EM maps have been deposited in the Protein Data Bank and the EMDB with accession codes 9DNM and EMD-47042 for βarr1–Cmpd-5, and 9DNG and EMD-47040 for βarr1 (apo). All data are available within the main text or supplementary materials.

ACKNOWLEDGMENTS

R.J.L. is an investigator with the Howard Hughes Medical Institute (HHMI). This work was supported in part by the U.S. National Institutes of Health, National Heart, Lung, and Blood Institute (Grant HL16037 to R.J.L.; Grants T32HL007101 and HL16037-45S1 to A.W.K.; and Grants R35GM147088 and R21CA243052 to A.R.B.T.), the National Institute on Drug Abuse – Intramural Research Program (Z1A DA000606 to L.S.), and the St. Jude Children's Research Hospital Collaborative Research Consortium on G protein-coupled receptors (GPCRs). We thank the National Cancer Institute (NCI) Developmental Therapeutics Program (DTP) Open Chemical Repository for providing compound libraries and additional compounds for this research. Cryo-EM data were screened and collected using the Krios at Duke University's Shared Materials Instrumentation Facility (SMIF), a member of the North Carolina Research Triangle Nanotechnology Network (RTNN), supported by the National Science Foundation (award number ECCS-2025064) as part of the National Nanotechnology Coordinated Infrastructure (NNCI). We are grateful to Dr. Nilakshee Bhattacharya at SMIF for assistance with microscope operation and data collection. This work utilized the computational resources of the NIH HPC Biowulf cluster (http://hpc.nih.gov). We also acknowledge the Flow Cytometry Shared Resource at Duke Cancer Institute. We thank Dr. Stéphane Laporte (McGill University, Montreal, Quebec, Canada) for the generous gift of CRISPR/Cas9 βarr1/2-knockout (KO) HEK293 cell lines and Dr. Irving Wainer (Laboratory of Clinical Investigation, National Institute on Aging Intramural Research Program, Baltimore, MD) for providing [^{3}H] (R,R′)-4-methoxyfenoterol. N.P. is supported by postdoctoral fellowships from the Human Frontier Science Program (LT000174/2018) and the European Molecular Biology Organization (ALTF 1071-2017). P.J.S. and H.Y.K. are supported by Research Fellowships from the Sarnoff Cardiovascular Research Foundation. Our gratitude also goes to Icee (Yangyang) Li for

her diligent secretarial support, as well as to Dr. Li-Yin Huang, Stephanie Martin, Xinrong Jiang, and William Capel for generously sharing their technical expertise.

AUTHOR CONTRIBUTIONS

A.W.K. and R.J.L. conceived the study. A.W.K., H.Y.K., K.S.S., J.G.L., C.T.dR., P.J.S., M.A.L., B.N.S., S.L., A.M.S., E.F.E., C.A.K., J.W., and S.A. designed, conducted, and analyzed drug screening, biophysical assays, *in vitro* binding studies, and biochemical and cellular functional assays. A.W.K., N.P., K.S.S., J.G.L., C.T.dR., P.J.S., B.N.S., B.N.T., J.K., and X.Z. contributed to construct design, reagent preparation, protein purification, and quality control. L.A.M.R. and J.S.S. conducted T cell migration assay. N.P., with assistance from B.N.T., prepared cryo-EM samples and performed data acquisition. N.P. performed data processing, model building, and refinement. V.A.G. and L.S. conducted MD simulations and data analysis. A.W.K., N.P., L.S., A.M., and R.J.L. analyzed and interpreted the structural data. A.W.K., H.A.R., A.R.B.T., L.A.M.R., L.S., S.A., and R.J.L coordinated and supervised research**.** A.W.K. and R.J.L. drafted the original manuscript, with A.W.K., N.P., A.M., and R.J.L. finalizing the paper with input from all authors.

DECLARATION OF INTERESTS

A.W.K. and R.J.L. are co-inventors of a patent application (PCT/US2020/044403) on β-arrestin-modulating compounds and methods of use, filed by Duke University. A.W.K., L.A.M.R., and R.J.L. are also co-inventors of a patent application (PCT/US2020/044474) on compositions and methods for treating intracranial diseases, also filed by Duke University. R.J.L. is a co-founder of Septerna, Inc., a company focused on the discovery and development of novel GPCR-targeted therapeutics and serves on the board of Lexicon Pharmaceuticals. H.A.R. and R.J.L. are co-founders of Trevena, Inc. A.R.B.T. is a scientific co-founder of Unco Therapeutics LLC. The other authors declare no competing financial interests.

REFERENCES

Adams, P.D., Afonine, P.V., Bunkoczi, G., Chen, V.B., Echols, N., Headd, J.J., Hung, L.W., Jain, S., Kapral, G.J., Grosse Kunstleve, R.W., et al. (2011). The Phenix software for automated determination of macromolecular structures. Methods *55*, 94-106. 10.1016/j.ymeth.2011.07.005.

Ahn, S., Kahsai, A.W., Pani, B., Wang, Q.T., Zhao, S., Wall, A.L., Strachan, R.T., Staus, D.P., Wingler, L.M., Sun, L.D., et al. (2017). Allosteric "beta-blocker" isolated from a DNA-encoded small molecule library. Proc Natl Acad Sci U S A *114*, 1708-1713. 10.1073/pnas.1620645114.

Ahn, S., Maarsingh, H., Walker, J.K., Liu, S., Hegde, A., Sumajit, H.C., Kahsai, A.W., and Lefkowitz, R.J. (2023). Allosteric modulator potentiates beta2AR agonist-promoted bronchoprotection in asthma models. J Clin Invest *133*. 10.1172/JCI167337.

Ahn, S., Shenoy, S.K., Luttrell, L.M., and Lefkowitz, R.J. (2020). SnapShot: beta-Arrestin Functions. Cell *182*, 1362-1362 e1361. 10.1016/j.cell.2020.07.034.

Asher, W.B., Terry, D.S., Gregorio, G.G.A., Kahsai, A.W., Borgia, A., Xie, B., Modak, A., Zhu, Y., Jang, W., Govindaraju, A., et al. (2022). GPCR-mediated beta-arrestin activation deconvoluted with single-molecule precision. Cell *185*, 1661-1675 e1616. 10.1016/j.cell.2022.03.042.

Attramadal, H., Arriza, J.L., Aoki, C., Dawson, T.M., Codina, J., Kwatra, M.M., Snyder, S.H., Caron, M.G., and Lefkowitz, R.J. (1992). Beta-arrestin2, a novel member of the arrestin/beta-arrestin gene family. J Biol Chem *267*, 17882-17890.

Bagnato, A., and Rosano, L. (2019). New Routes in GPCR/beta-Arrestin-Driven Signaling in Cancer Progression and Metastasis. Front Pharmacol *10*, 114. 10.3389/fphar.2019.00114.

Benovic, J.L., Kuhn, H., Weyand, I., Codina, J., Caron, M.G., and Lefkowitz, R.J. (1987). Functional desensitization of the isolated beta-adrenergic receptor by the beta-adrenergic receptor kinase: potential role of an analog of the retinal protein arrestin (48-kDa protein). Proc Natl Acad Sci U S A *84*, 8879-8882. 10.1073/pnas.84.24.8879.

Bepler, T., Morin, A., Rapp, M., Brasch, J., Shapiro, L., Noble, A.J., and Berger, B. (2019). Positive-unlabeled convolutional neural networks for particle picking in cryo-electron micrographs. Nat Methods *16*, 1153-1160. 10.1038/s41592-019-0575-8.

Bohn, L.M., Lefkowitz, R.J., Gainetdinov, R.R., Peppel, K., Caron, M.G., and Lin, F.T. (1999). Enhanced morphine analgesia in mice lacking beta-arrestin 2. Science *286*, 2495-2498. 10.1126/science.286.5449.2495.

Bond, R.A., Lucero Garcia-Rojas, E.Y., Hegde, A., and Walker, J.K.L. (2019). Therapeutic Potential of Targeting ss-Arrestin. Front Pharmacol *10*, 124. 10.3389/fphar.2019.00124.

Bouley, R.A., Weinberg, Z.Y., Waldschmidt, H.V., Yen, Y.C., Larsen, S.D., Puthenveedu, M.A., and Tesmer, J.J.G. (2020). A New Paroxetine-Based GRK2 Inhibitor Reduces Internalization of the mu-Opioid Receptor. Mol Pharmacol *97*, 392-401. 10.1124/mol.119.118661.

Bous, J., Fouillen, A., Orcel, H., Trapani, S., Cong, X., Fontanel, S., Saint-Paul, J., Lai-Kee-Him, J., Urbach, S., Sibille, N., et al. (2022). Structure of the vasopressin hormone-V2 receptor-beta-arrestin1 ternary complex. Sci Adv *8*, eabo7761. 10.1126/sciadv.abo7761.

Bowers, K.J., Chow, E., Xu, H., Dror, R.O., Eastwood, M.P., Gregersen, B.A., Klepeis, J.L., Kolossvary, I., Moraes, M.A., Sacerdoti, F.D., et al. (2006). Scalable Algorithms for Molecular Dynamics Simulations on Commodity Clusters. pp. 43.

Cahill, T.J., 3rd, Thomsen, A.R., Tarrasch, J.T., Plouffe, B., Nguyen, A.H., Yang, F., Huang, L.Y., Kahsai, A.W., Bassoni, D.L., Gavino, B.J., et al. (2017). Distinct conformations of GPCR-beta-arrestin complexes mediate desensitization, signaling, and endocytosis. Proc Natl Acad Sci U S A *114*, 2562-2567. 10.1073/pnas.1701529114.

Cao, C., Barros-Alvarez, X., Zhang, S., Kim, K., Damgen, M.A., Panova, O., Suomivuori, C.M., Fay, J.F., Zhong, X., Krumm, B.E., et al. (2022). Signaling snapshots of a serotonin receptor activated by the prototypical psychedelic LSD. Neuron *110*, 3154-3167 e3157. 10.1016/j.neuron.2022.08.006.

Chen, V.B., Arendall, W.B., 3rd, Headd, J.J., Keedy, D.A., Immormino, R.M., Kapral, G.J., Murray, L.W., Richardson, J.S., and Richardson, D.C. (2010). MolProbity: all-atom structure validation for macromolecular crystallography. Acta Crystallogr D Biol Crystallogr *66*, 12-21. 10.1107/S0907444909042073.

Cheung, R., Malik, M., Ravyn, V., Tomkowicz, B., Ptasznik, A., and Collman, R.G. (2009). An arrestin-dependent multi-kinase signaling complex mediates MIP-1beta/CCL4 signaling and chemotaxis of primary human macrophages. J Leukoc Biol *86*, 833-845. 10.1189/jlb.0908551.

Comerford, I., Harata-Lee, Y., Bunting, M.D., Gregor, C., Kara, E.E., and McColl, S.R. (2013). A myriad of functions and complex regulation of the CCR7/CCL19/CCL21 chemokine axis in the adaptive immune system. Cytokine Growth Factor Rev *24*, 269-283. 10.1016/j.cytogfr.2013.03.001.

Conner, D.A., Mathier, M.A., Mortensen, R.M., Christe, M., Vatner, S.F., Seidman, C.E., and Seidman, J.G. (1997). beta-Arrestin1 knockout mice appear normal but demonstrate altered cardiac responses to beta-adrenergic stimulation. Circ Res *81*, 1021-1026. 10.1161/01.res.81.6.1021.

Croll, T.I. (2018). ISOLDE: a physically realistic environment for model building into low-resolution electron-density maps. Acta Crystallogr D Struct Biol *74*, 519-530. 10.1107/S2059798318002425.

Dai, S.A., Hu, Q., Gao, R., Blythe, E.E., Touhara, K.K., Peacock, H., Zhang, Z., von Zastrow, M., Suga, H., and Shokat, K.M. (2022). State-selective modulation of heterotrimeric Galphas signaling with macrocyclic peptides. Cell *185*, 3950-3965 e3925. 10.1016/j.cell.2022.09.019.

Daly, C., Guseinov, A.A., Hahn, H., Wright, A., Tikhonova, I.G., Thomsen, A.R.B., and Plouffe, B. (2023). beta-Arrestin-dependent and -independent endosomal G protein activation by the vasopressin type 2 receptor. Elife *12*. 10.7554/eLife.87754.

DeLean, A., and Lefkowitz, R.J. (1980). Dihydroergocryptine binding and alpha-adrenoreceptors in smooth muscle. Nature *283*, 109-110. 10.1038/283109a0.

Dixon, A.S., Schwinn, M.K., Hall, M.P., Zimmerman, K., Otto, P., Lubben, T.H., Butler, B.L., Binkowski, B.F., Machleidt, T., Kirkland, T.A., et al. (2016). NanoLuc Complementation Reporter Optimized for Accurate Measurement of Protein Interactions in Cells. ACS Chem Biol *11*, 400-408. 10.1021/acschembio.5b00753.

Emsley, P., Lohkamp, B., Scott, W.G., and Cowtan, K. (2010). Features and development of Coot. Acta Crystallogr D Biol Crystallogr *66*, 486-501. 10.1107/S0907444910007493.

Ereno-Orbea, J., Sicard, T., Cui, H., Carson, J., Hermans, P., and Julien, J.P. (2018). Structural Basis of Enhanced Crystallizability Induced by a Molecular Chaperone for Antibody Antigen-Binding Fragments. J Mol Biol *430*, 322-336. 10.1016/j.jmb.2017.12.010.

Favata, M.F., Horiuchi, K.Y., Manos, E.J., Daulerio, A.J., Stradley, D.A., Feeser, W.S., Van Dyk, D.E., Pitts, W.J., Earl, R.A., Hobbs, F., et al. (1998). Identification of a novel inhibitor of mitogen-activated protein kinase kinase. J Biol Chem *273*, 18623-18632. 10.1074/jbc.273.29.18623.

Feller, S.E., Zhang, Y.H., Pastor, R.W., and Brooks, B.R. (1995). Constant-Pressure Molecular-Dynamics Simulation - the Langevin Piston Method. J Chem Phys *103*, 4613-4621. Doi 10.1063/1.470648.

Fereshteh, M., Ito, T., Kovacs, J.J., Zhao, C., Kwon, H.Y., Tornini, V., Konuma, T., Chen, M., Lefkowitz, R.J., and Reya, T. (2012). beta-Arrestin2 mediates the initiation and progression of myeloid leukemia. Proc Natl Acad Sci U S A *109*, 12532-12537. 10.1073/pnas.1209815109.

Ferguson, S.S. (2001). Evolving concepts in G protein-coupled receptor endocytosis: the role in receptor desensitization and signaling. Pharmacol Rev *53*, 1-24.

Ferrero, K.M., and Koch, W.J. (2022). GRK2 in cardiovascular disease and its potential as a therapeutic target. J Mol Cell Cardiol *172*, 14-23. 10.1016/j.yjmcc.2022.07.008.

Freedman, N.J., and Shenoy, S.K. (2018). Regulation of inflammation by beta-arrestins: Not just receptor tales. Cell Signal *41*, 41-45. 10.1016/j.cellsig.2017.02.008.

Grady, E.F., Bohm, S.K., and Bunnett, N.W. (1997). Turning off the signal: mechanisms that attenuate signaling by G protein-coupled receptors. Am J Physiol *273*, G586-601. 10.1152/ajpgi.1997.273.3.G586.

Gurevich, V.V., and Gurevich, E.V. (2014). Extensive shape shifting underlies functional versatility of arrestins. Curr Opin Cell Biol *27*, 1-9. 10.1016/j.ceb.2013.10.007.

Gurevich, V.V., and Gurevich, E.V. (2019). Plethora of functions packed into 45 kDa arrestins: biological implications and possible therapeutic strategies. Cell Mol Life Sci *76*, 4413-4421. 10.1007/s00018-019-03272-5.

Gurevich, V.V., Pals-Rylaarsdam, R., Benovic, J.L., Hosey, M.M., and Onorato, J.J. (1997). Agonist-receptor-arrestin, an alternative ternary complex with high agonist affinity. J Biol Chem *272*, 28849-28852. 10.1074/jbc.272.46.28849.

Han, M., Gurevich, V.V., Vishnivetskiy, S.A., Sigler, P.B., and Schubert, C. (2001). Crystal structure of beta-arrestin at 1.9 A: possible mechanism of receptor binding and membrane Translocation. Structure *9*, 869-880. 10.1016/s0969-2126(01)00644-x.

Hauser, A.S., Attwood, M.M., Rask-Andersen, M., Schioth, H.B., and Gloriam, D.E. (2017). Trends in GPCR drug discovery: new agents, targets and indications. Nat Rev Drug Discov *16*, 829-842. 10.1038/nrd.2017.178.

Humphrey, W., Dalke, A., and Schulten, K. (1996). VMD: visual molecular dynamics. J Mol Graph *14*, 33-38, 27-38.

Hunton, D.L., Barnes, W.G., Kim, J., Ren, X.R., Violin, J.D., Reiter, E., Milligan, G., Patel, D.D., and Lefkowitz, R.J. (2005). Beta-arrestin 2-dependent angiotensin II type

1A receptor-mediated pathway of chemotaxis. Mol Pharmacol *67*, 1229-1236. 10.1124/mol.104.006270.

Jiang, D., Xie, T., Liang, J., and Noble, P.W. (2013). beta-Arrestins in the immune system. Prog Mol Biol Transl Sci *118*, 359-393. 10.1016/B978-0-12-394440-5.00014-0.

Joseph, A.P., Lagerstedt, I., Jakobi, A., Burnley, T., Patwardhan, A., Topf, M., and Winn, M. (2020). Comparing Cryo-EM Reconstructions and Validating Atomic Model Fit Using Difference Maps. J Chem Inf Model *60*, 2552-2560. 10.1021/acs.jcim.9b01103.

Kahsai, A.W., Pani, B., and Lefkowitz, R.J. (2018). GPCR signaling: conformational activation of arrestins. Cell Res *28*, 783-784. 10.1038/s41422-018-0067-x.

Kahsai, A.W., Shah, K.S., Shim, P.J., Lee, M.A., Shreiber, B.N., Schwalb, A.M., Zhang, X., Kwon, H.Y., Huang, L.Y., Soderblom, E.J., et al. (2023). Signal transduction at GPCRs: Allosteric activation of the ERK MAPK by beta-arrestin. Proc Natl Acad Sci U S A *120*, e2303794120. 10.1073/pnas.2303794120.

Kahsai, A.W., Wisler, J.W., Lee, J., Ahn, S., Cahill Iii, T.J., Dennison, S.M., Staus, D.P., Thomsen, A.R., Anasti, K.M., Pani, B., et al. (2016). Conformationally selective RNA aptamers allosterically modulate the beta2-adrenoceptor. Nat Chem Biol *12*, 709-716. 10.1038/nchembio.2126.

Kahsai, A.W., Xiao, K., Rajagopal, S., Ahn, S., Shukla, A.K., Sun, J., Oas, T.G., and Lefkowitz, R.J. (2011). Multiple ligand-specific conformations of the beta2-adrenergic receptor. Nat Chem Biol *7*, 692-700. 10.1038/nchembio.634.

Kim, I.M., Tilley, D.G., Chen, J., Salazar, N.C., Whalen, E.J., Violin, J.D., and Rockman, H.A. (2008). Beta-blockers alprenolol and carvedilol stimulate beta-arrestin-mediated EGFR transactivation. Proc Natl Acad Sci U S A *105*, 14555-14560. 10.1073/pnas.0804745105.

Kohout, T.A., Lin, F.S., Perry, S.J., Conner, D.A., and Lefkowitz, R.J. (2001). beta-Arrestin 1 and 2 differentially regulate heptahelical receptor signaling and trafficking. Proc Natl Acad Sci U S A *98*, 1601-1606. 10.1073/pnas.98.4.1601.

Laporte, S.A., Oakley, R.H., Holt, J.A., Barak, L.S., and Caron, M.G. (2000). The interaction of beta-arrestin with the AP-2 adaptor is required for the clustering of beta 2-adrenergic receptor into clathrin-coated pits. J Biol Chem *275*, 23120-23126. 10.1074/jbc.M002581200.

Laporte, S.A., Oakley, R.H., Zhang, J., Holt, J.A., Ferguson, S.S., Caron, M.G., and Barak, L.S. (1999). The beta2-adrenergic receptor/betaarrestin complex recruits the clathrin adaptor AP-2 during endocytosis. Proc Natl Acad Sci U S A *96*, 3712-3717. 10.1073/pnas.96.7.3712.

Lee, M.H., Appleton, K.M., Strungs, E.G., Kwon, J.Y., Morinelli, T.A., Peterson, Y.K., Laporte, S.A., and Luttrell, L.M. (2016). The conformational signature of beta-arrestin2 predicts its trafficking and signalling functions. Nature *531*, 665-668. 10.1038/nature17154.

Lee, Y., Warne, T., Nehme, R., Pandey, S., Dwivedi-Agnihotri, H., Chaturvedi, M., Edwards, P.C., Garcia-Nafria, J., Leslie, A.G.W., Shukla, A.K., and Tate, C.G. (2020). Molecular basis of beta-arrestin coupling to formoterol-bound beta(1)-adrenoceptor. Nature *583*, 862-866. 10.1038/s41586-020-2419-1.

Lefkowitz, R.J. (2013a). Arrestins come of age: a personal historical perspective. Prog Mol Biol Transl Sci *118*, 3-18. 10.1016/B978-0-12-394440-5.00001-2.

Lefkowitz, R.J. (2013b). A brief history of G-protein coupled receptors (Nobel Lecture). Angew Chem Int Ed Engl *52*, 6366-6378. 10.1002/anie.201301924.

Lefkowitz, R.J., Rockman, H.A., Shim, P.J., Liu, S., Ahn, S., Pani, B., Rajagopal, S., Shenoy, S.K., Bouvier, M., Benovic, J.L., et al. (2023). How carvedilol does not activate beta(2)-adrenoceptors. Nat Commun *14*, 7866. 10.1038/s41467-023-42848-5.

Lefkowitz, R.J., and Shenoy, S.K. (2005). Transduction of receptor signals by beta-arrestins. Science *308*, 512-517. 10.1126/science.1109237.

Li, A., Liu, S., Huang, R., Ahn, S., and Lefkowitz, R.J. (2023). Loss of biased signaling at a G protein-coupled receptor in overexpressed systems. PLoS One *18*, e0283477. 10.1371/journal.pone.0283477.

Lin, R., Choi, Y.H., Zidar, D.A., and Walker, J.K.L. (2018). beta-Arrestin-2-Dependent Signaling Promotes CCR4-mediated Chemotaxis of Murine T-Helper Type 2 Cells. Am J Respir Cell Mol Biol *58*, 745-755. 10.1165/rcmb.2017-0240OC.

Lohse, M.J., Benovic, J.L., Codina, J., Caron, M.G., and Lefkowitz, R.J. (1990). beta-Arrestin: a protein that regulates beta-adrenergic receptor function. Science *248*, 1547-1550. 10.1126/science.2163110.

Lu, C., Wu, C., Ghoreishi, D., Chen, W., Wang, L., Damm, W., Ross, G.A., Dahlgren, M.K., Russell, E., Von Bargen, C.D., et al. (2021). OPLS4: Improving Force Field Accuracy on Challenging Regimes of Chemical Space. J Chem Theory Comput *17*, 4291-4300. 10.1021/acs.jctc.1c00302.

Luttrell, L.M., Ferguson, S.S., Daaka, Y., Miller, W.E., Maudsley, S., Della Rocca, G.J., Lin, F., Kawakatsu, H., Owada, K., Luttrell, D.K., et al. (1999). Beta-arrestin-dependent formation of beta2 adrenergic receptor-Src protein kinase complexes. Science *283*, 655-661. 10.1126/science.283.5402.655.

Luttrell, L.M., Roudabush, F.L., Choy, E.W., Miller, W.E., Field, M.E., Pierce, K.L., and Lefkowitz, R.J. (2001). Activation and targeting of extracellular signal-regulated kinases by beta-arrestin scaffolds. Proc Natl Acad Sci U S A *98*, 2449-2454. 10.1073/pnas.041604898.

Luttrell, L.M., Wang, J., Plouffe, B., Smith, J.S., Yamani, L., Kaur, S., Jean-Charles, P.Y., Gauthier, C., Lee, M.H., Pani, B., et al. (2018). Manifold roles of beta-arrestins in GPCR signaling elucidated with siRNA and CRISPR/Cas9. Sci Signal *11*. 10.1126/scisignal.aat7650.

McGovern, K.W., and DeFea, K.A. (2014). Molecular mechanisms underlying beta-arrestin-dependent chemotaxis and actin-cytoskeletal reorganization. Handb Exp Pharmacol *219*, 341-359. 10.1007/978-3-642-41199-1_17.

Menard, L., Ferguson, S.S., Zhang, J., Lin, F.T., Lefkowitz, R.J., Caron, M.G., and Barak, L.S. (1997). Synergistic regulation of beta2-adrenergic receptor sequestration: intracellular complement of beta-adrenergic receptor kinase and beta-arrestin determine kinetics of internalization. Mol Pharmacol *51*, 800-808.

Milano, S.K., Pace, H.C., Kim, Y.M., Brenner, C., and Benovic, J.L. (2002). Scaffolding functions of arrestin-2 revealed by crystal structure and mutagenesis. Biochemistry *41*, 3321-3328. 10.1021/bi015905j.

Mukherjee, S., Erramilli, S.K., Ammirati, M., Alvarez, F.J.D., Fennell, K.F., Purdy, M.D., Skrobek, B.M., Radziwon, K., Coukos, J., Kang, Y., et al. (2020). Synthetic antibodies against BRIL as universal fiducial marks for single-particle cryoEM structure

determination of membrane proteins. Nat Commun *11*, 1598. 10.1038/s41467-020-15363-0.
Namkung, Y., Le Gouill, C., Lukashova, V., Kobayashi, H., Hogue, M., Khoury, E., Song, M., Bouvier, M., and Laporte, S.A. (2016). Monitoring G protein-coupled receptor and beta-arrestin trafficking in live cells using enhanced bystander BRET. Nat Commun *7*, 12178. 10.1038/ncomms12178.
Niesen, F.H., Berglund, H., and Vedadi, M. (2007). The use of differential scanning fluorimetry to detect ligand interactions that promote protein stability. Nat Protoc *2*, 2212-2221. 10.1038/nprot.2007.321.
Nobles, K.N., Guan, Z., Xiao, K., Oas, T.G., and Lefkowitz, R.J. (2007). The active conformation of beta-arrestin1: direct evidence for the phosphate sensor in the N-domain and conformational differences in the active states of beta-arrestins1 and -2. J Biol Chem *282*, 21370-21381. 10.1074/jbc.M611483200.
Noma, T., Lemaire, A., Naga Prasad, S.V., Barki-Harrington, L., Tilley, D.G., Chen, J., Le Corvoisier, P., Violin, J.D., Wei, H., Lefkowitz, R.J., and Rockman, H.A. (2007). Beta-arrestin-mediated beta1-adrenergic receptor transactivation of the EGFR confers cardioprotection. J Clin Invest *117*, 2445-2458. 10.1172/JCI31901.
Nuber, S., Zabel, U., Lorenz, K., Nuber, A., Milligan, G., Tobin, A.B., Lohse, M.J., and Hoffmann, C. (2016). beta-Arrestin biosensors reveal a rapid, receptor-dependent activation/deactivation cycle. Nature *531*, 661-664. 10.1038/nature17198.
Oakley, R.H., Laporte, S.A., Holt, J.A., Caron, M.G., and Barak, L.S. (2000). Differential affinities of visual arrestin, beta arrestin1, and beta arrestin2 for G protein-coupled receptors delineate two major classes of receptors. J Biol Chem *275*, 17201-17210. 10.1074/jbc.M910348199.
Pakharukova, N., Masoudi, A., Pani, B., Staus, D.P., and Lefkowitz, R.J. (2020). Allosteric activation of proto-oncogene kinase Src by GPCR-beta-arrestin complexes. J Biol Chem *295*, 16773-16784. 10.1074/jbc.RA120.015400.
Pandey, S., Kumari, P., Baidya, M., Kise, R., Cao, Y., Dwivedi-Agnihotri, H., Banerjee, R., Li, X.X., Cui, C.S., Lee, J.D., et al. (2021). Intrinsic bias at non-canonical, beta-arrestin-coupled seven transmembrane receptors. Mol Cell *81*, 4605-4621 e4611. 10.1016/j.molcel.2021.09.007.
Peterson, Y.K., and Luttrell, L.M. (2017). The Diverse Roles of Arrestin Scaffolds in G Protein-Coupled Receptor Signaling. Pharmacol Rev *69*, 256-297. 10.1124/pr.116.013367.
Pettersen, E.F., Goddard, T.D., Huang, C.C., Couch, G.S., Greenblatt, D.M., Meng, E.C., and Ferrin, T.E. (2004). UCSF Chimera--a visualization system for exploratory research and analysis. J Comput Chem *25*, 1605-1612. 10.1002/jcc.20084.
Pierce, K.L., Premont, R.T., and Lefkowitz, R.J. (2002). Seven-transmembrane receptors. Nat Rev Mol Cell Biol *3*, 639-650. 10.1038/nrm908.
Pitcher, J.A., Freedman, N.J., and Lefkowitz, R.J. (1998). G protein-coupled receptor kinases. Annu Rev Biochem *67*, 653-692. 10.1146/annurev.biochem.67.1.653.
Punjani, A., Rubinstein, J.L., Fleet, D.J., and Brubaker, M.A. (2017). cryoSPARC: algorithms for rapid unsupervised cryo-EM structure determination. Nat Methods *14*, 290-296. 10.1038/nmeth.4169.
Rasmussen, S.G., Choi, H.J., Fung, J.J., Pardon, E., Casarosa, P., Chae, P.S., Devree, B.T., Rosenbaum, D.M., Thian, F.S., Kobilka, T.S., et al. (2011). Structure of a

nanobody-stabilized active state of the beta(2) adrenoceptor. Nature *469*, 175-180. 10.1038/nature09648.

Rein, L.A., Wisler, J.W., Kim, J., Theriot, B., Huang, L., Price, T., Yang, H., Chen, M., Chen, W., Sipkins, D., et al. (2017). beta-Arrestin2 mediates progression of murine primary myelofibrosis. JCI Insight *2*. 10.1172/jci.insight.98094.

Renaud, J.P., Chung, C.W., Danielson, U.H., Egner, U., Hennig, M., Hubbard, R.E., and Nar, H. (2016). Biophysics in drug discovery: impact, challenges and opportunities. Nat Rev Drug Discov *15*, 679-698. 10.1038/nrd.2016.123.

Rizk, S.S., Paduch, M., Heithaus, J.H., Duguid, E.M., Sandstrom, A., and Kossiakoff, A.A. (2011). Allosteric control of ligand-binding affinity using engineered conformation-specific effector proteins. Nat Struct Mol Biol *18*, 437-442. 10.1038/nsmb.2002.

Sanchez-Garcia, R., Gomez-Blanco, J., Cuervo, A., Carazo, J.M., Sorzano, C.O.S., and Vargas, J. (2021). DeepEMhancer: a deep learning solution for cryo-EM volume post-processing. Commun Biol *4*, 874. 10.1038/s42003-021-02399-1.

Schlegel, J.G., Tahoun, M., Seidinger, A., Voss, J.H., Kuschak, M., Kehraus, S., Schneider, M., Matthey, M., Fleischmann, B.K., Konig, G.M., et al. (2021). Macrocyclic Gq Protein Inhibitors FR900359 and/or YM-254890-Fit for Translation? ACS Pharmacol Transl Sci *4*, 888-897. 10.1021/acsptsci.1c00021.

Schrage, R., Schmitz, A.L., Gaffal, E., Annala, S., Kehraus, S., Wenzel, D., Bullesbach, K.M., Bald, T., Inoue, A., Shinjo, Y., et al. (2015). The experimental power of FR900359 to study Gq-regulated biological processes. Nat Commun *6*, 10156. 10.1038/ncomms10156.

Shukla, A.K., Manglik, A., Kruse, A.C., Xiao, K., Reis, R.I., Tseng, W.C., Staus, D.P., Hilger, D., Uysal, S., Huang, L.Y., et al. (2013). Structure of active beta-arrestin-1 bound to a G-protein-coupled receptor phosphopeptide. Nature *497*, 137-141. 10.1038/nature12120.

Shukla, A.K., Westfield, G.H., Xiao, K., Reis, R.I., Huang, L.Y., Tripathi-Shukla, P., Qian, J., Li, S., Blanc, A., Oleskie, A.N., et al. (2014). Visualization of arrestin recruitment by a G-protein-coupled receptor. Nature *512*, 218-222. 10.1038/nature13430.

Smith, J.S., Alagesan, P., Desai, N.K., Pack, T.F., Wu, J.H., Inoue, A., Freedman, N.J., and Rajagopal, S. (2017). C-X-C Motif Chemokine Receptor 3 Splice Variants Differentially Activate Beta-Arrestins to Regulate Downstream Signaling Pathways. Mol Pharmacol *92*, 136-150. 10.1124/mol.117.108522.

Smith, J.S., Lefkowitz, R.J., and Rajagopal, S. (2018a). Biased signalling: from simple switches to allosteric microprocessors. Nat Rev Drug Discov *17*, 243-260. 10.1038/nrd.2017.229.

Smith, J.S., Nicholson, L.T., Suwanpradid, J., Glenn, R.A., Knape, N.M., Alagesan, P., Gundry, J.N., Wehrman, T.S., Atwater, A.R., Gunn, M.D., et al. (2018b). Biased agonists of the chemokine receptor CXCR3 differentially control chemotaxis and inflammation. Sci Signal *11*. 10.1126/scisignal.aaq1075.

Smith, J.S., Pack, T.F., Inoue, A., Lee, C., Zheng, K., Choi, I., Eiger, D.S., Warman, A., Xiong, X., Ma, Z., et al. (2021). Noncanonical scaffolding of G(alphai) and beta-arrestin by G protein-coupled receptors. Science *371*. 10.1126/science.aay1833.

Smith, J.S., and Rajagopal, S. (2016). The beta-Arrestins: Multifunctional Regulators of G Protein-coupled Receptors. J Biol Chem *291*, 8969-8977. 10.1074/jbc.R115.713313.

Sriram, K., and Insel, P.A. (2018). G Protein-Coupled Receptors as Targets for Approved Drugs: How Many Targets and How Many Drugs? Mol Pharmacol *93*, 251-258. 10.1124/mol.117.111062.

Staus, D.P., Hu, H., Robertson, M.J., Kleinhenz, A.L.W., Wingler, L.M., Capel, W.D., Latorraca, N.R., Lefkowitz, R.J., and Skiniotis, G. (2020). Structure of the M2 muscarinic receptor-beta-arrestin complex in a lipid nanodisc. Nature *579*, 297-302. 10.1038/s41586-020-1954-0.

Thal, D.M., Yeow, R.Y., Schoenau, C., Huber, J., and Tesmer, J.J. (2011). Molecular mechanism of selectivity among G protein-coupled receptor kinase 2 inhibitors. Mol Pharmacol *80*, 294-303. 10.1124/mol.111.071522.

Thathiah, A., Horre, K., Snellinx, A., Vandewyer, E., Huang, Y., Ciesielska, M., De Kloe, G., Munck, S., and De Strooper, B. (2013). beta-arrestin 2 regulates Abeta generation and gamma-secretase activity in Alzheimer's disease. Nat Med *19*, 43-49. 10.1038/nm.3023.

Thomsen, A.R.B., Plouffe, B., Cahill, T.J., 3rd, Shukla, A.K., Tarrasch, J.T., Dosey, A.M., Kahsai, A.W., Strachan, R.T., Pani, B., Mahoney, J.P., et al. (2016). GPCR-G Protein-beta-Arrestin Super-Complex Mediates Sustained G Protein Signaling. Cell *166*, 907-919. 10.1016/j.cell.2016.07.004.

Toll, L., Pajak, K., Plazinska, A., Jozwiak, K., Jimenez, L., Kozocas, J.A., Tanga, M.J., Bupp, J.E., and Wainer, I.W. (2012). Thermodynamics and docking of agonists to the beta(2)-adrenoceptor determined using [(3)H](R,R')-4-methoxyfenoterol as the marker ligand. Mol Pharmacol *81*, 846-854. 10.1124/mol.111.077347.

Tsutsumi, N., Mukherjee, S., Waghray, D., Janda, C.Y., Jude, K.M., Miao, Y., Burg, J.S., Aduri, N.G., Kossiakoff, A.A., Gati, C., and Garcia, K.C. (2020). Structure of human Frizzled5 by fiducial-assisted cryo-EM supports a heterodimeric mechanism of canonical Wnt signaling. Elife *9*. 10.7554/eLife.58464.

Vedadi, M., Niesen, F.H., Allali-Hassani, A., Fedorov, O.Y., Finerty, P.J., Jr., Wasney, G.A., Yeung, R., Arrowsmith, C., Ball, L.J., Berglund, H., et al. (2006). Chemical screening methods to identify ligands that promote protein stability, protein crystallization, and structure determination. Proc Natl Acad Sci U S A *103*, 15835-15840. 10.1073/pnas.0605224103.

Violin, J.D., Crombie, A.L., Soergel, D.G., and Lark, M.W. (2014). Biased ligands at G-protein-coupled receptors: promise and progress. Trends Pharmacol Sci *35*, 308-316. 10.1016/j.tips.2014.04.007.

Violin, J.D., DiPilato, L.M., Yildirim, N., Elston, T.C., Zhang, J., and Lefkowitz, R.J. (2008). beta2-adrenergic receptor signaling and desensitization elucidated by quantitative modeling of real time cAMP dynamics. J Biol Chem *283*, 2949-2961. 10.1074/jbc.M707009200.

Walker, J.K., and DeFea, K.A. (2014). Role for beta-arrestin in mediating paradoxical beta2AR and PAR2 signaling in asthma. Curr Opin Pharmacol *16*, 142-147. 10.1016/j.coph.2014.03.007.

Walker, J.K., Fong, A.M., Lawson, B.L., Savov, J.D., Patel, D.D., Schwartz, D.A., and Lefkowitz, R.J. (2003). Beta-arrestin-2 regulates the development of allergic asthma. J Clin Invest *112*, 566-574. 10.1172/JCI17265.

Wang, J., Hanada, K., Staus, D.P., Makara, M.A., Dahal, G.R., Chen, Q., Ahles, A., Engelhardt, S., and Rockman, H.A. (2017). Galphai is required for carvedilol-induced

beta1 adrenergic receptor beta-arrestin biased signaling. Nat Commun *8*, 1706. 10.1038/s41467-017-01855-z.

Wang, Y., Wu, L., Wang, T., Liu, J., Li, F., Jiang, L., Fan, Z., Yu, Y., Chen, N., Sun, Q., et al. (2024). Cryo-EM structure of cannabinoid receptor CB1-beta-arrestin complex. Protein Cell *15*, 230-234. 10.1093/procel/pwad055.

Webb, B., and Sali, A. (2016). Comparative Protein Structure Modeling Using MODELLER. Curr Protoc Bioinformatics *54*, 5 6 1-5 6 37. 10.1002/cpbi.3.

Wess, J., Oteng, A.B., Rivera-Gonzalez, O., Gurevich, E.V., and Gurevich, V.V. (2023a). beta- Arrestins: Structure, Function, Physiology, and Pharmacological Perspectives. Pharmacol Rev. 10.1124/pharmrev.121.000302.

Wess, J., Oteng, A.B., Rivera-Gonzalez, O., Gurevich, E.V., and Gurevich, V.V. (2023b). beta-Arrestins: Structure, Function, Physiology, and Pharmacological Perspectives. Pharmacol Rev *75*, 854-884. 10.1124/pharmrev.121.000302.

Whalen, E.J., Rajagopal, S., and Lefkowitz, R.J. (2011). Therapeutic potential of beta-arrestin- and G protein-biased agonists. Trends Mol Med *17*, 126-139. 10.1016/j.molmed.2010.11.004.

Wilkins, M.R., Gasteiger, E., Bairoch, A., Sanchez, J.C., Williams, K.L., Appel, R.D., and Hochstrasser, D.F. (1999). Protein identification and analysis tools in the ExPASy server. Methods Mol Biol *112*, 531-552. 10.1385/1-59259-584-7:531.

Wisler, J.W., DeWire, S.M., Whalen, E.J., Violin, J.D., Drake, M.T., Ahn, S., Shenoy, S.K., and Lefkowitz, R.J. (2007). A unique mechanism of beta-blocker action: carvedilol stimulates beta-arrestin signaling. Proc Natl Acad Sci U S A *104*, 16657-16662. 10.1073/pnas.0707936104.

Wolfe, B.L., and Trejo, J. (2007). Clathrin-dependent mechanisms of G protein-coupled receptor endocytosis. Traffic *8*, 462-470. 10.1111/j.1600-0854.2007.00551.x.

Wootten, D., Christopoulos, A., Marti-Solano, M., Babu, M.M., and Sexton, P.M. (2018). Mechanisms of signalling and biased agonism in G protein-coupled receptors. Nat Rev Mol Cell Biol *19*, 638-653. 10.1038/s41580-018-0049-3.

Xiao, K., McClatchy, D.B., Shukla, A.K., Zhao, Y., Chen, M., Shenoy, S.K., Yates, J.R., 3rd, and Lefkowitz, R.J. (2007). Functional specialization of beta-arrestin interactions revealed by proteomic analysis. Proc Natl Acad Sci U S A *104*, 12011-12016. 10.1073/pnas.0704849104.

Xiao, K., Sun, J., Kim, J., Rajagopal, S., Zhai, B., Villen, J., Haas, W., Kovacs, J.J., Shukla, A.K., Hara, M.R., et al. (2010). Global phosphorylation analysis of beta-arrestin-mediated signaling downstream of a seven transmembrane receptor (7TMR). Proc Natl Acad Sci U S A *107*, 15299-15304. 10.1073/pnas.1008461107.

Xiong, X.F., Zhang, H., Boesgaard, M.W., Underwood, C.R., Brauner-Osborne, H., and Stromgaard, K. (2019). Structure-Activity Relationship Studies of the Natural Product G(q/11) Protein Inhibitor YM-254890. ChemMedChem *14*, 865-870. 10.1002/cmdc.201900018.

Zhou, X.E., He, Y., de Waal, P.W., Gao, X., Kang, Y., Van Eps, N., Yin, Y., Pal, K., Goswami, D., White, T.A., et al. (2017). Identification of Phosphorylation Codes for Arrestin Recruitment by G Protein-Coupled Receptors. Cell *170*, 457-469 e413. 10.1016/j.cell.2017.07.002.

Zoudilova, M., Min, J., Richards, H.L., Carter, D., Huang, T., and DeFea, K.A. (2010). beta-Arrestins scaffold cofilin with chronophin to direct localized actin filament severing

and membrane protrusions downstream of protease-activated receptor-2. J Biol Chem *285*, 14318-14329. 10.1074/jbc.M109.055806.

Figure 1

A.

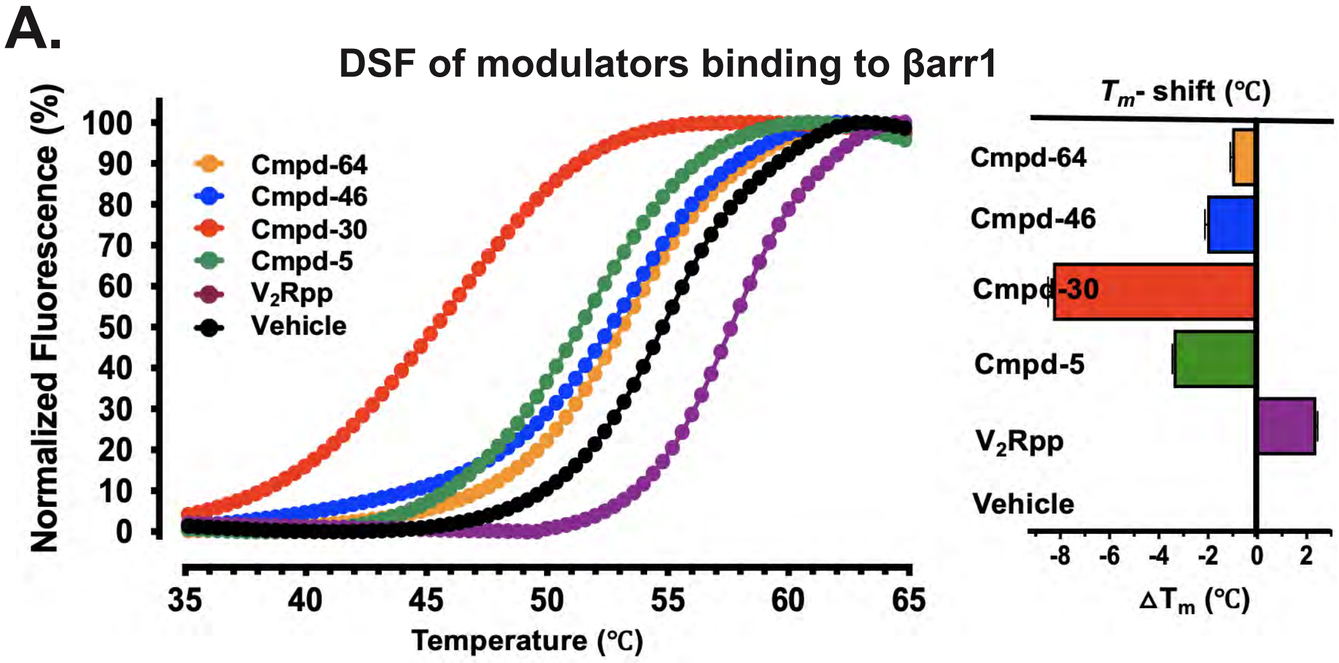

B.

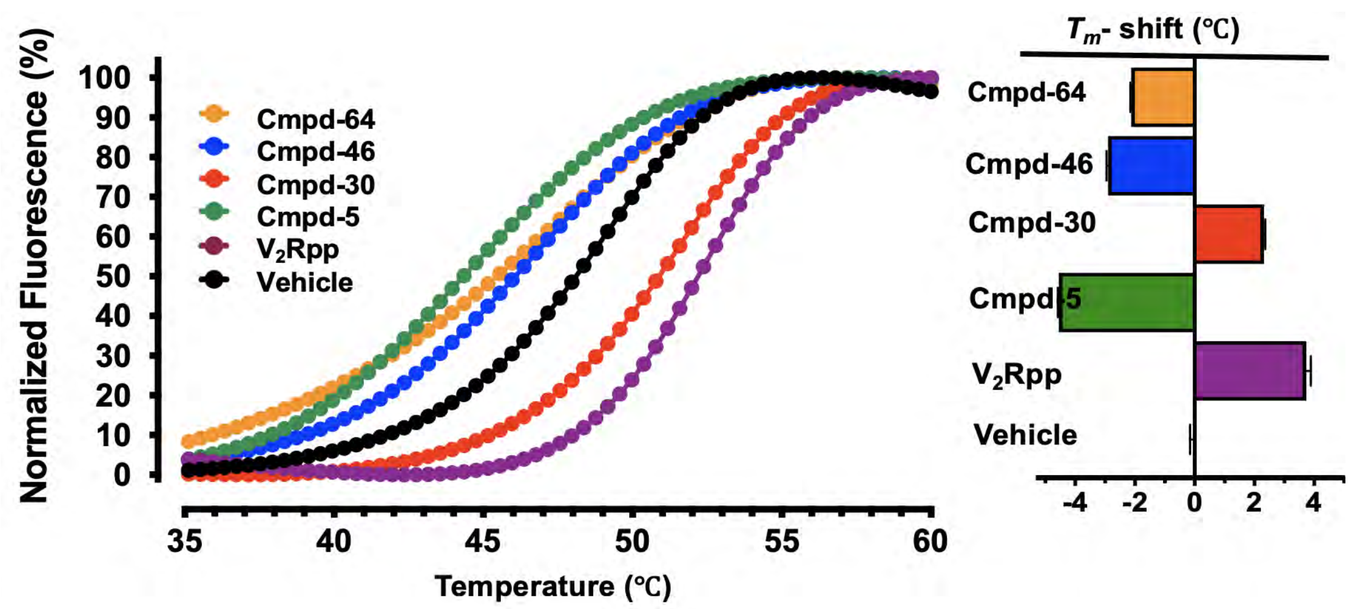

C.

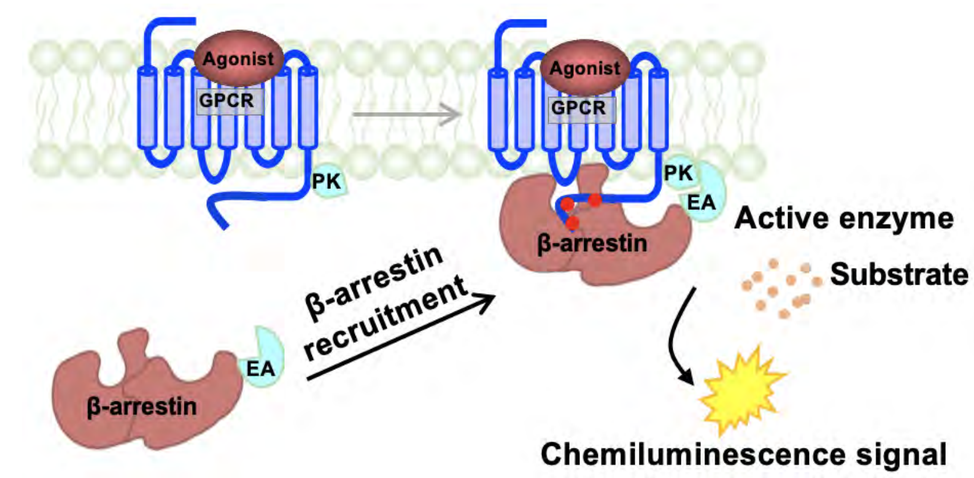

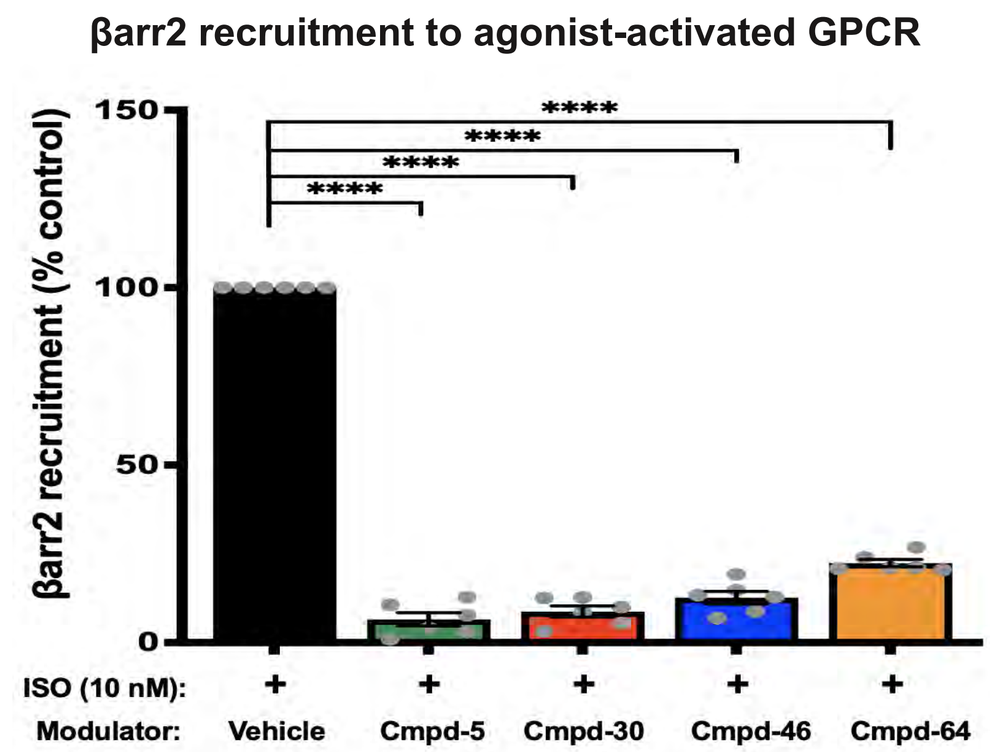

D.

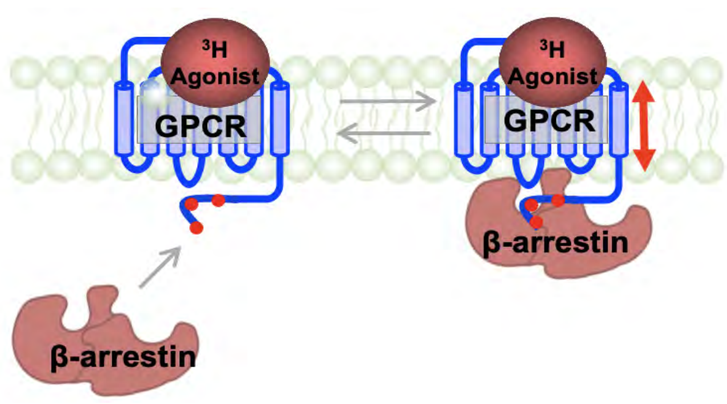

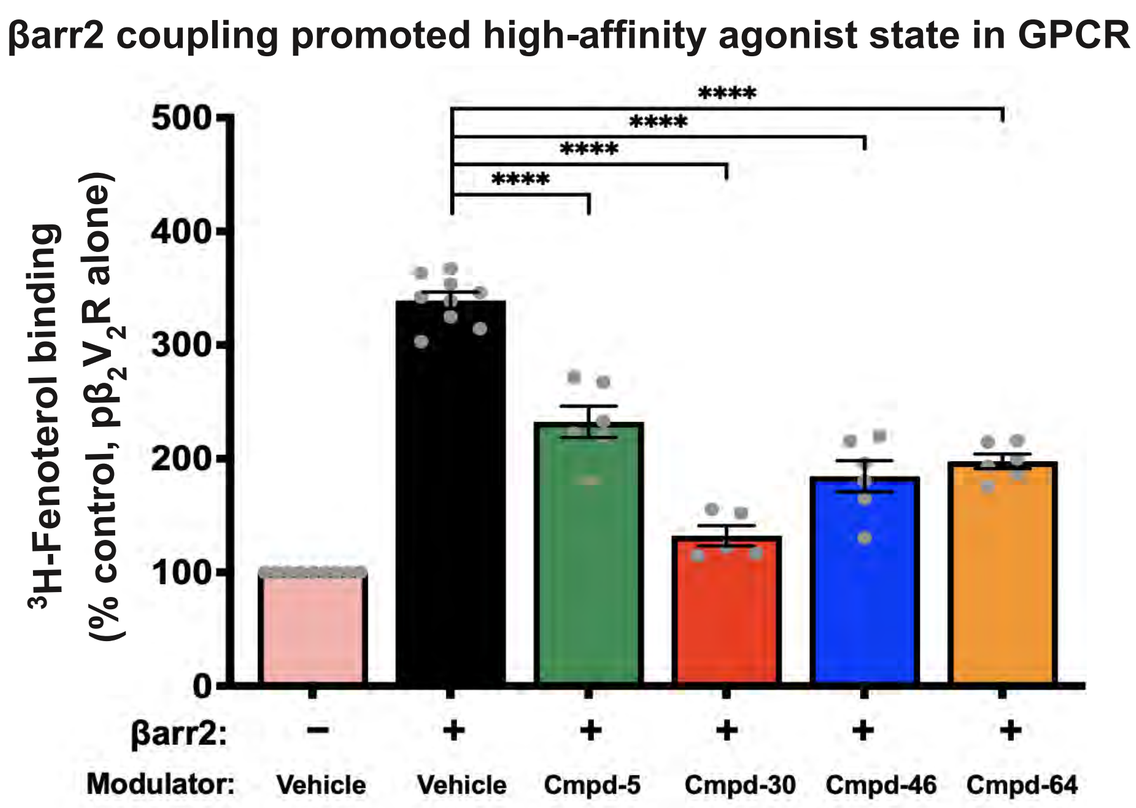

E.

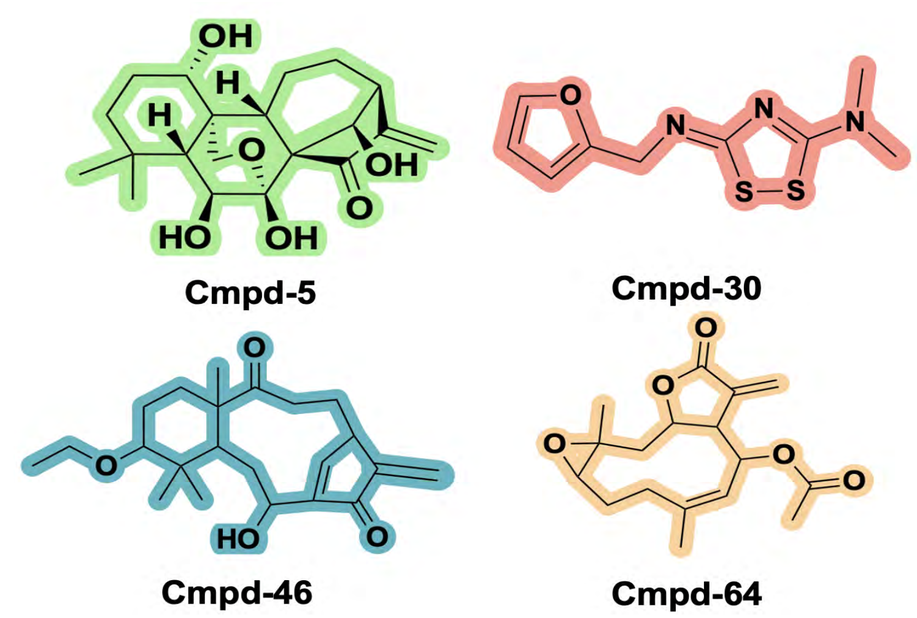

F.

	Dissociation constant (K_d)	
	βarr1	βarr2
Cmpd-5	362 ± 65.1 nM	563 ± 45.0 nM
Cmpd-30	27 ± 49.2 nM	14 ± 30.0 nM
Cmpd-46	1.34 ± 0.74 μM	753 ± 53.8 nM
Cmpd-64	1.42 ± 0.20 μM	207 ± 54.2 nM

Figure 2

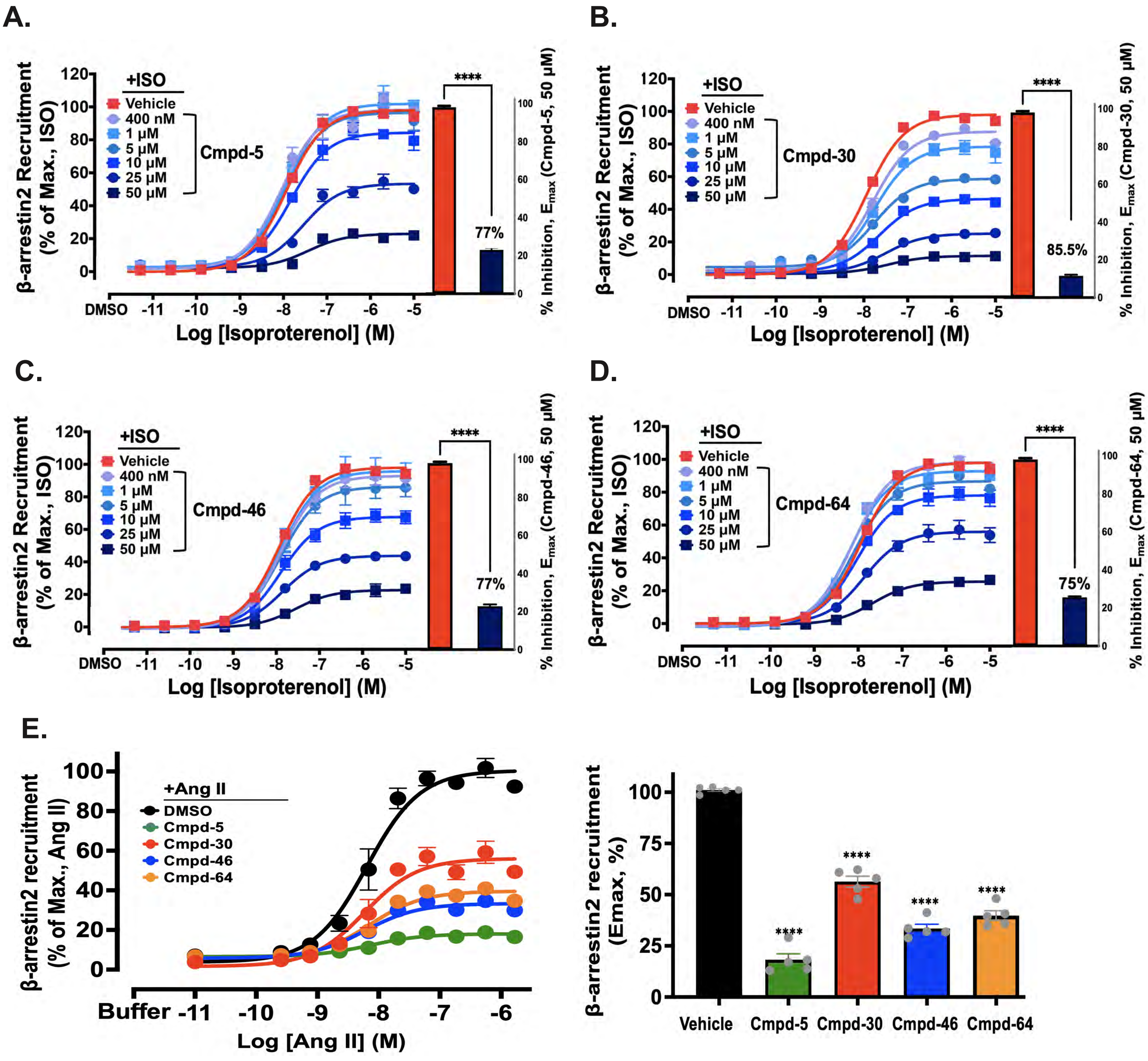
A.
+ISO
Vehicle
400 nM
1 μM
5 μM
10 μM
25 μM
50 μM
Cmpd-5
****
77%
β-arrestin2 Recruitment (% of Max., ISO)
% Inhibition, Emax (Cmpd-5, 50 μM)
DMSO -11 -10 -9 -8 -7 -6 -5
Log [Isoproterenol] (M)
B.
+ISO
Vehicle
400 nM
1 μM
5 μM
10 μM
25 μM
50 μM
Cmpd-30
****
85.5%
β-arrestin2 Recruitment (% of Max., ISO)
% Inhibition, Emax (Cmpd-30, 50 μM)
DMSO -11 -10 -9 -8 -7 -6 -5
Log [Isoproterenol] (M)
C.
+ISO
Vehicle
400 nM
1 μM
5 μM
10 μM
25 μM
50 μM
Cmpd-46
****
77%
β-arrestin2 Recruitment (% of Max., ISO)
% Inhibition, Emax (Cmpd-46, 50 μM)
DMSO -11 -10 -9 -8 -7 -6 -5
Log [Isoproterenol] (M)
D.
+ISO
Vehicle
400 nM
1 μM
5 μM
10 μM
25 μM
50 μM
Cmpd-64
****
75%
β-arrestin2 Recruitment (% of Max., ISO)
% Inhibition, Emax (Cmpd-64, 50 μM)
DMSO -11 -10 -9 -8 -7 -6 -5
Log [Isoproterenol] (M)
E.
+Ang II
DMSO
Cmpd-5
Cmpd-30
Cmpd-46
Cmpd-64
β-arrestin2 recruitment (% of Max., Ang II)
Buffer -11 -10 -9 -8 -7 -6
Log [Ang II] (M)
β-arrestin2 recruitment (Emax, %)
****
Vehicle
Cmpd-5
Cmpd-30
Cmpd-46
Cmpd-64

Figure 2

F.

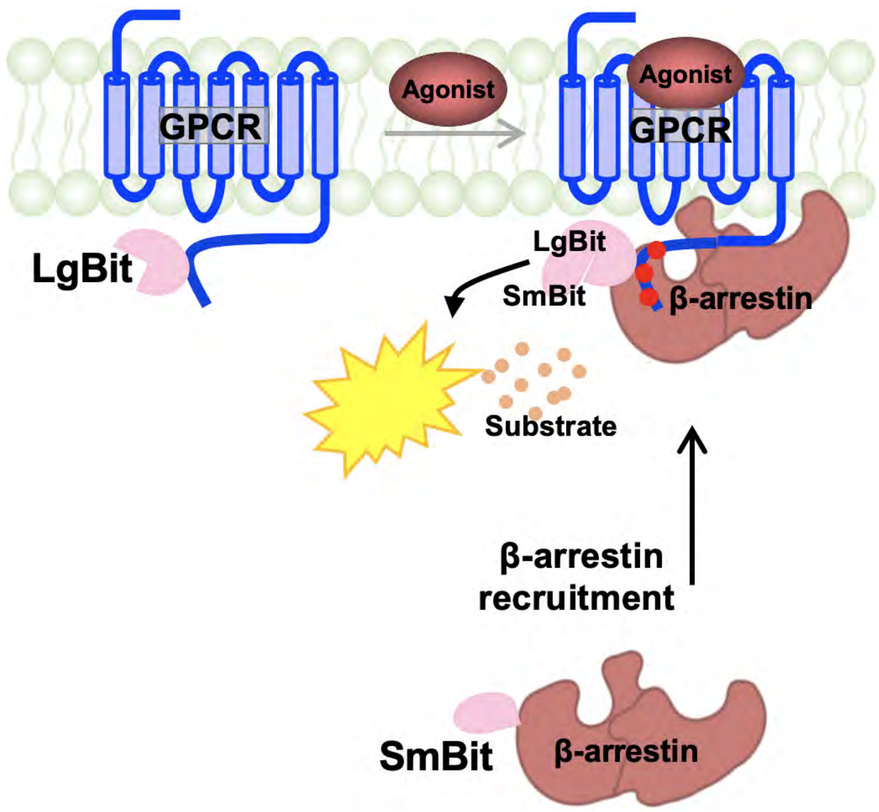
GPCR
Agonist
Agonist
GPCR
LgBit
LgBit
SmBit
β-arrestin
Substrate
β-arrestin
recruitment
SmBit
β-arrestin

G.

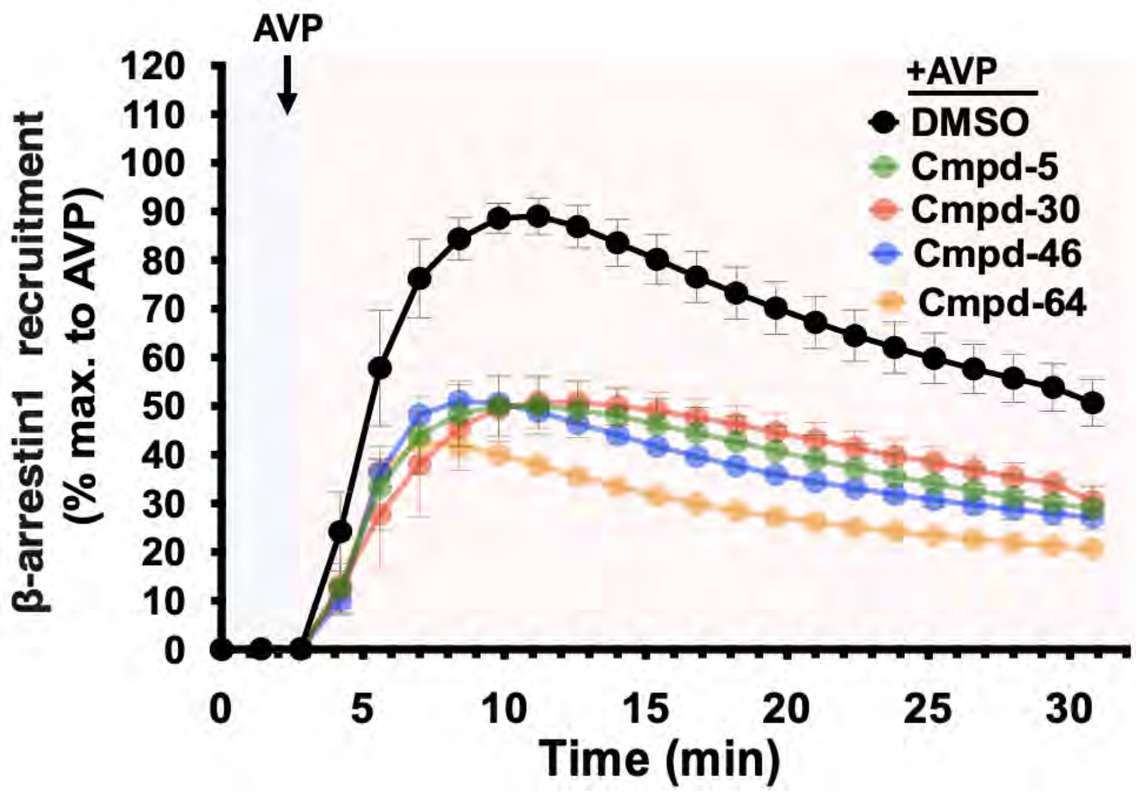
AVP
+AVP
DMSO
Cmpd-5
Cmpd-30
Cmpd-46
Cmpd-64
β-arrestin1 recruitment
(% max. to AVP)
Time (min)
0
5
10
15
20
25
30
0
10
20
30
40
50
60
70
80
90
100
110
120

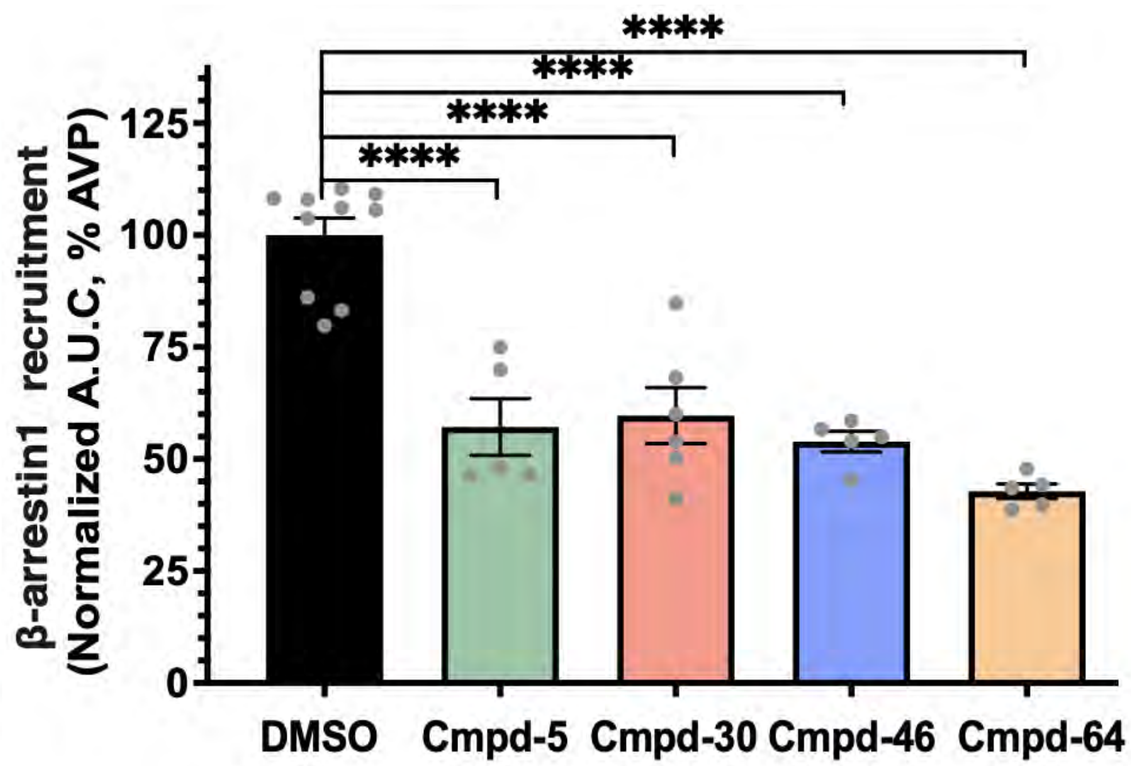
****
****
****
****
β-arrestin1 recruitment
(Normalized A.U.C, % AVP)
0
25
50
75
100
125
DMSO
Cmpd-5
Cmpd-30
Cmpd-46
Cmpd-64

H.

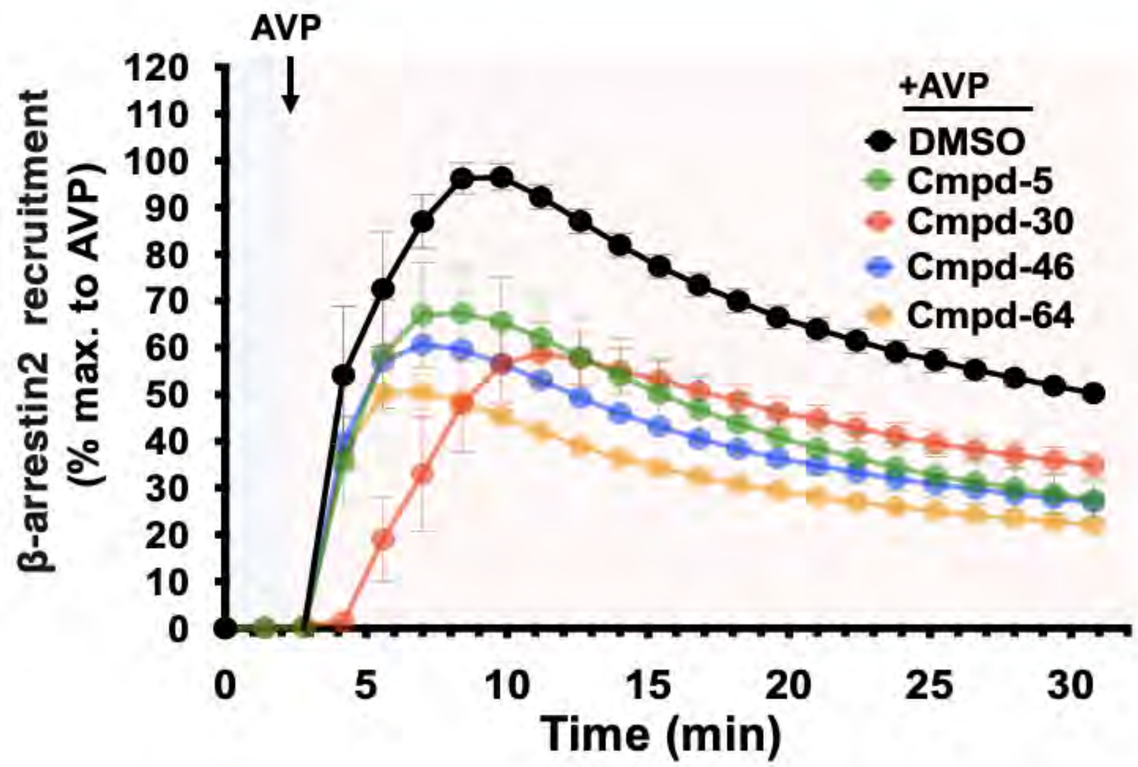
AVP
+AVP
DMSO
Cmpd-5
Cmpd-30
Cmpd-46
Cmpd-64
β-arrestin2 recruitment
(% max. to AVP)
Time (min)
0
5
10
15
20
25
30
0
10
20
30
40
50
60
70
80
90
100
110
120

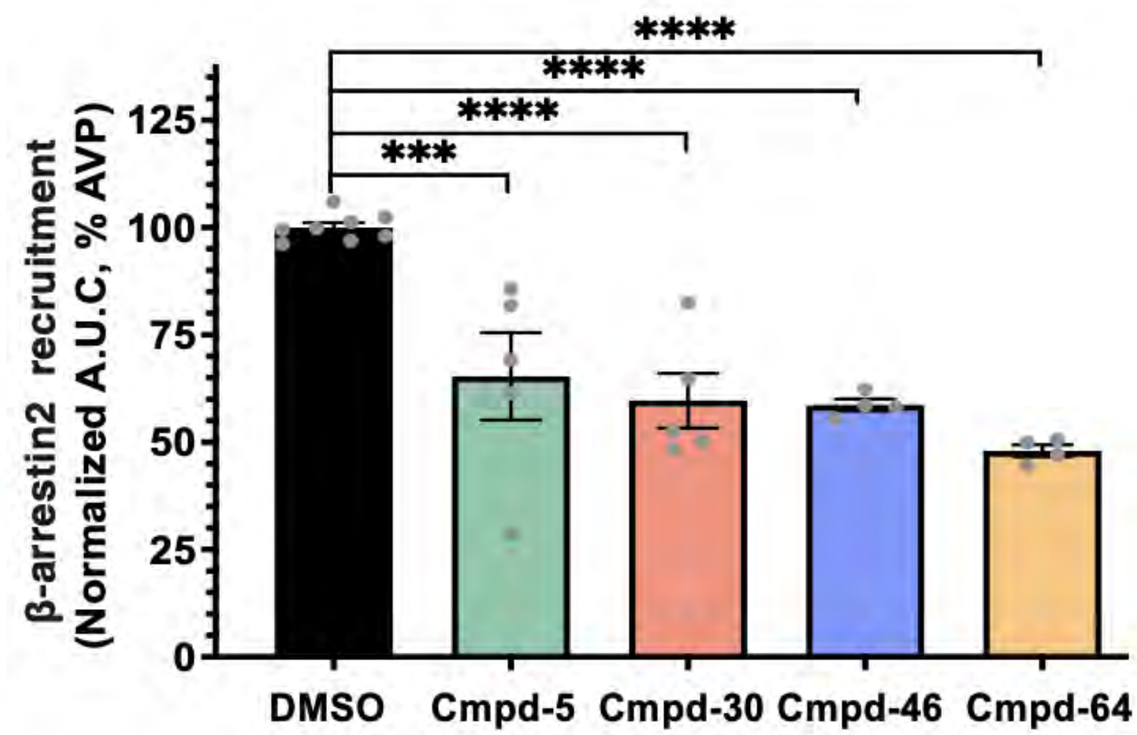
****
****
****
***
β-arrestin2 recruitment
(Normalized A.U.C, % AVP)
0
25
50
75
100
125
DMSO
Cmpd-5
Cmpd-30
Cmpd-46
Cmpd-64

Figure 3

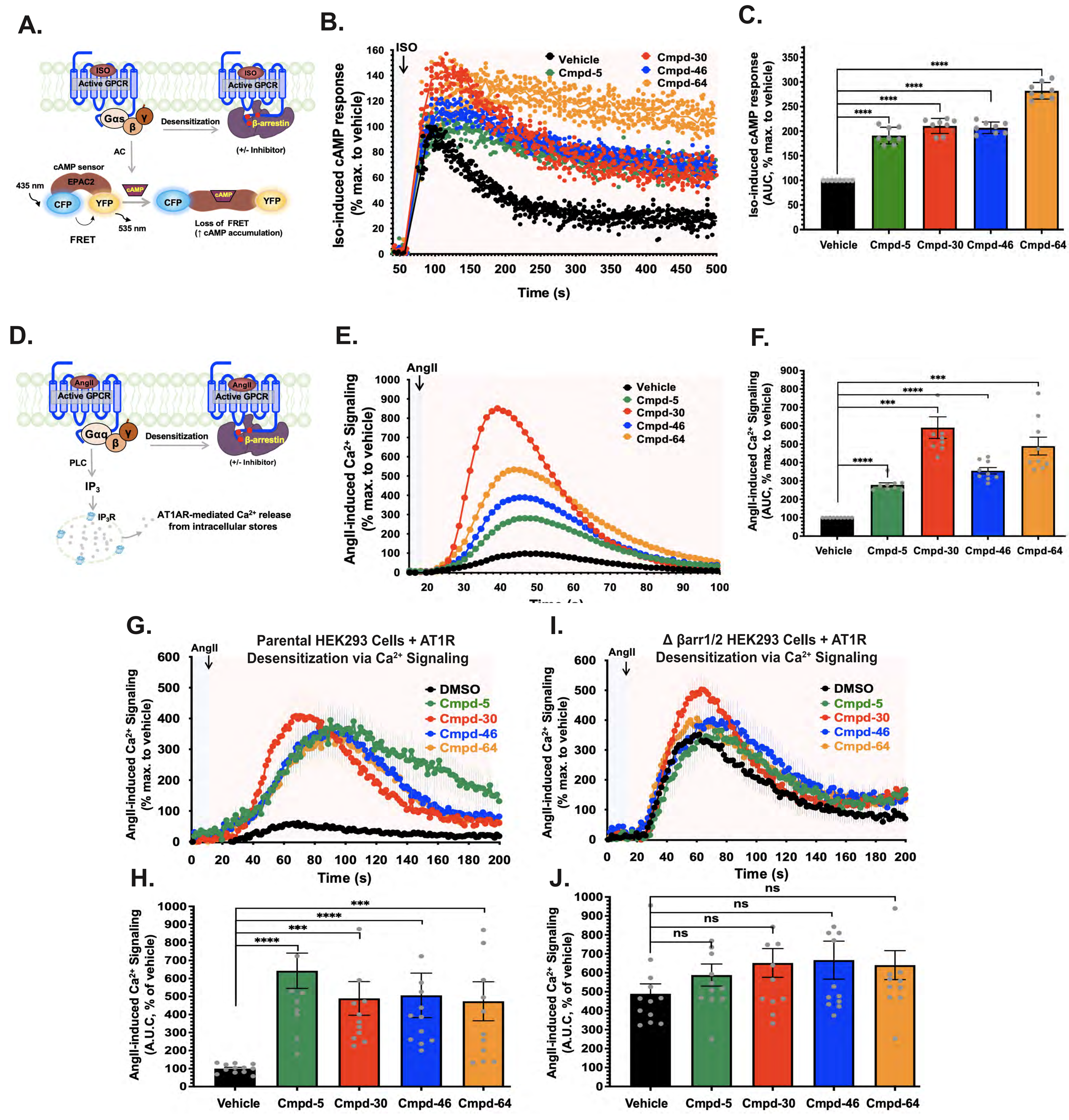
A.
ISO
Active GPCR
Gαs
β
γ
Desensitization
β-arrestin
(+/- Inhibitor)
AC
cAMP sensor
EPAC2
435 nm
CFP
YFP
cAMP
535 nm
FRET
Loss of FRET
(↑ cAMP accumulation)
B.
ISO
Vehicle
Cmpd-5
Cmpd-30
Cmpd-46
Cmpd-64
Iso-induced cAMP response
(% max. to vehicle)
Time (s)
C.
Iso-induced cAMP response
(AUC, % max. to vehicle)
Vehicle
Cmpd-5
Cmpd-30
Cmpd-46
Cmpd-64
D.
AngII
Active GPCR
Gαq
β
γ
Desensitization
β-arrestin
(+/- Inhibitor)
PLC
IP3
IP3R
AT1AR-mediated Ca2+ release
from intracellular stores
E.
AngII
Vehicle
Cmpd-5
Cmpd-30
Cmpd-46
Cmpd-64
AngII-induced Ca2+ Signaling
(% max. to vehicle)
F.
AngII-induced Ca2+ Signaling
(AUC, % max. to vehicle)
Vehicle
Cmpd-5
Cmpd-30
Cmpd-46
Cmpd-64
G.
Parental HEK293 Cells + AT1R
Desensitization via Ca2+ Signaling
AngII
DMSO
Cmpd-5
Cmpd-30
Cmpd-46
Cmpd-64
AngII-induced Ca2+ Signaling
(% max. to vehicle)
Time (s)
I.
Δ βarr1/2 HEK293 Cells + AT1R
Desensitization via Ca2+ Signaling
AngII
DMSO
Cmpd-5
Cmpd-30
Cmpd-46
Cmpd-64
AngII-induced Ca2+ Signaling
(% max. to vehicle)
Time (s)
H.
AngII-induced Ca2+ Signaling
(A.U.C, % of vehicle)
Vehicle
Cmpd-5
Cmpd-30
Cmpd-46
Cmpd-64
J.
AngII-induced Ca2+ Signaling
(A.U.C, % of vehicle)
ns
Vehicle
Cmpd-5
Cmpd-30
Cmpd-46
Cmpd-64

Figure 4

A.

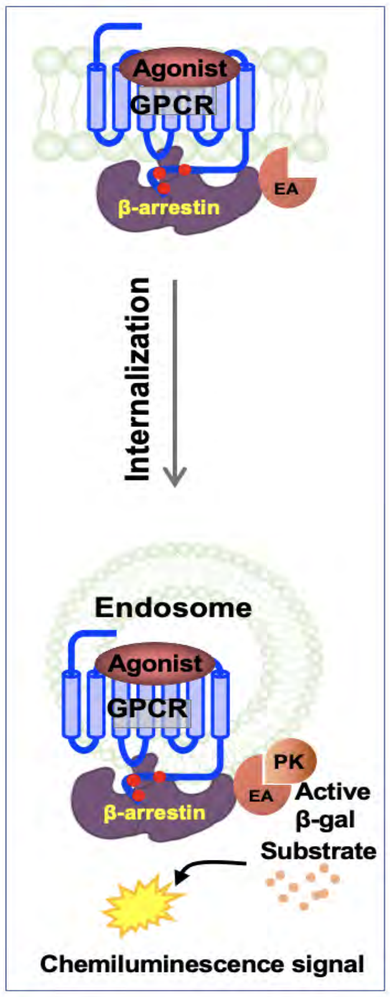

B.

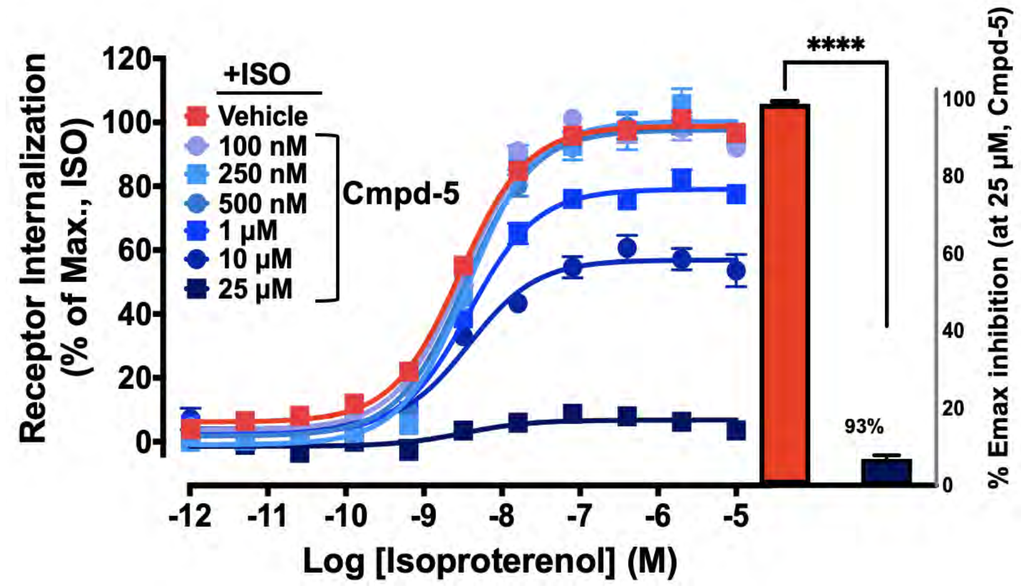

C.

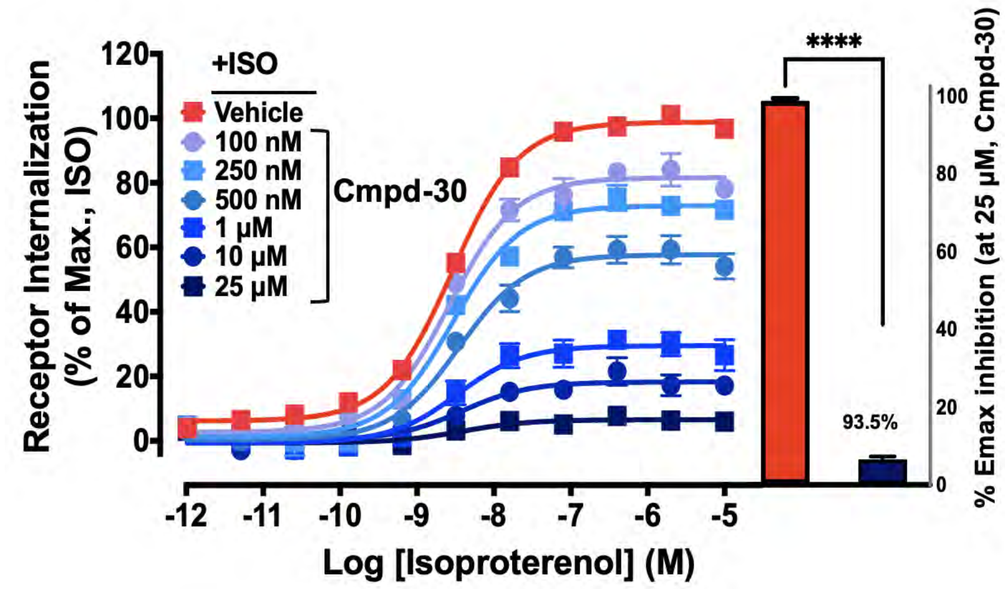

D.

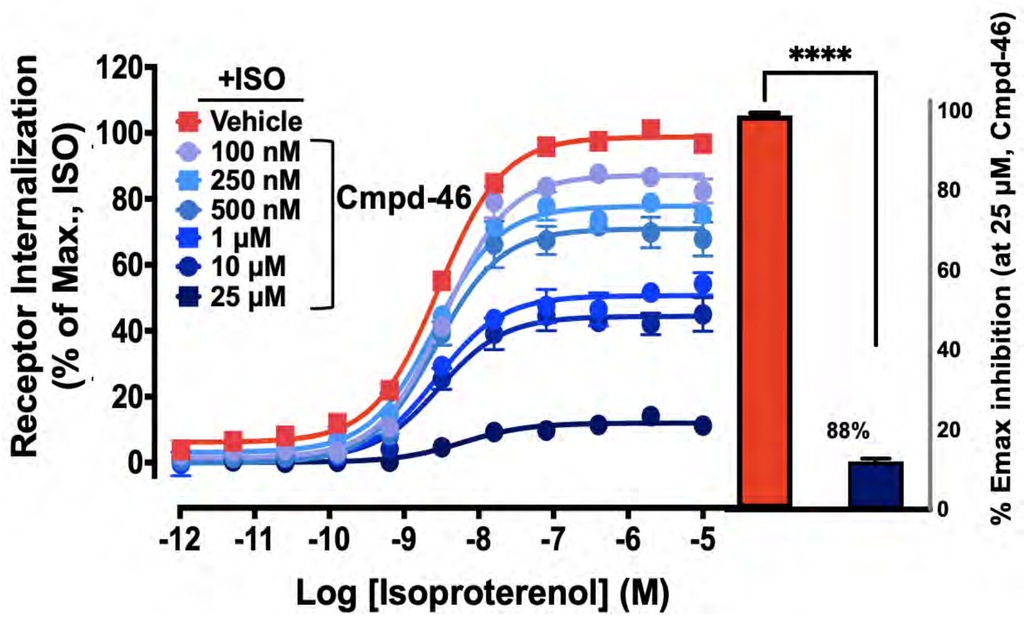

E.

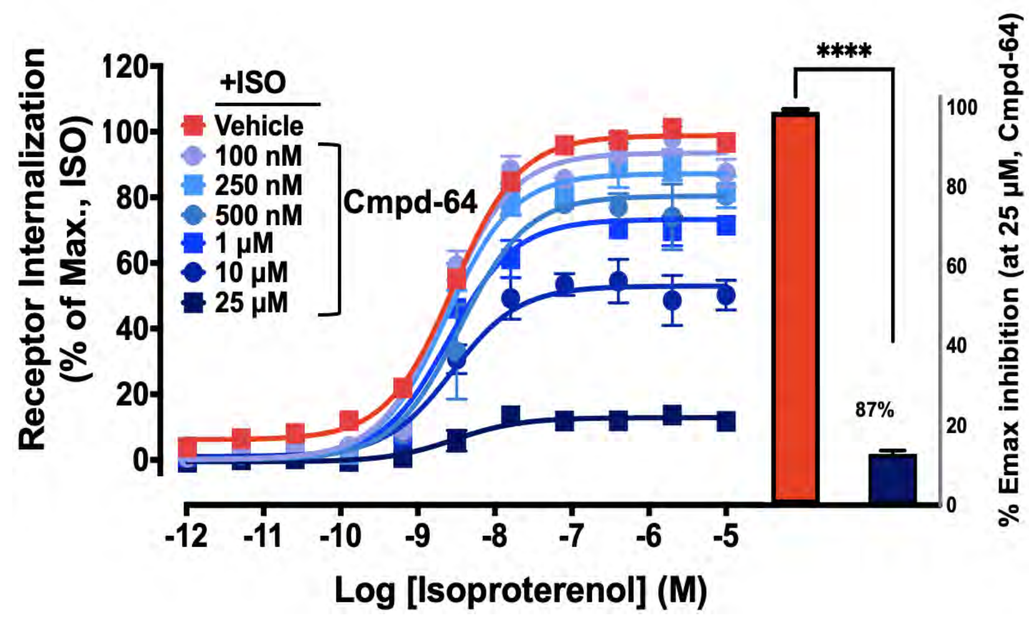

F.

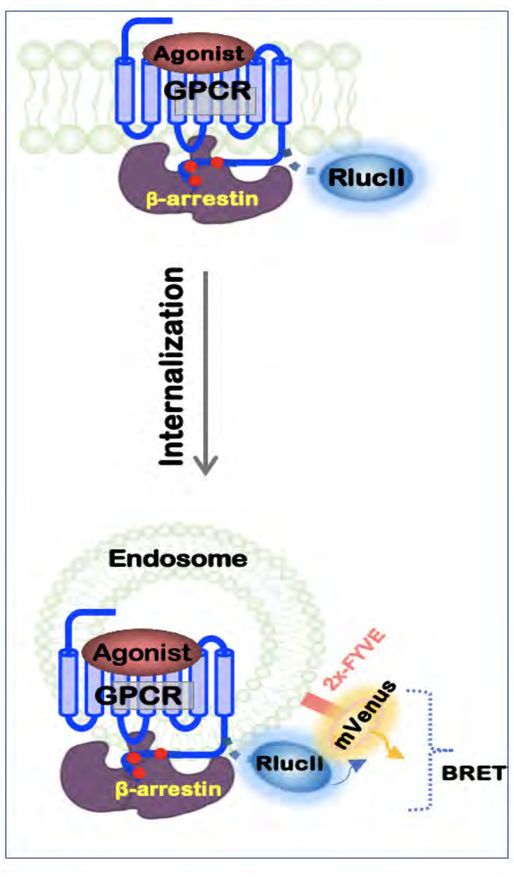

G.

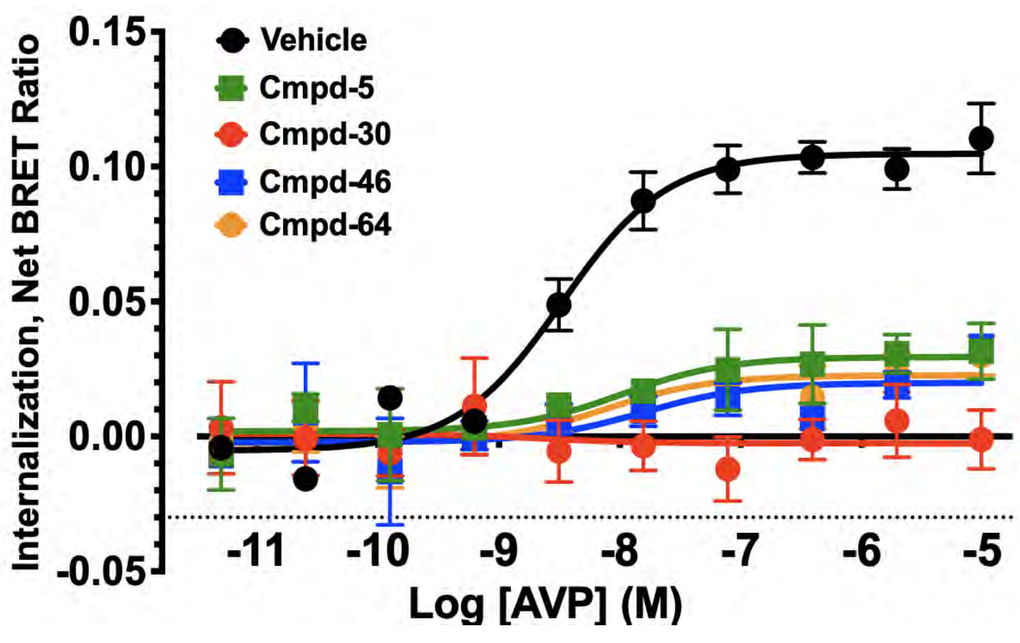

H.

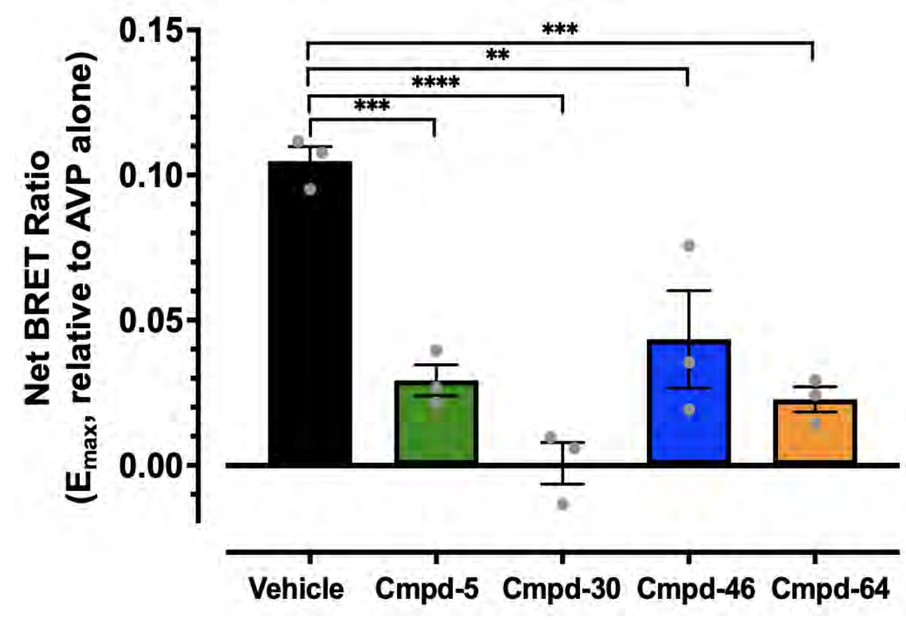

Figure 5

A.

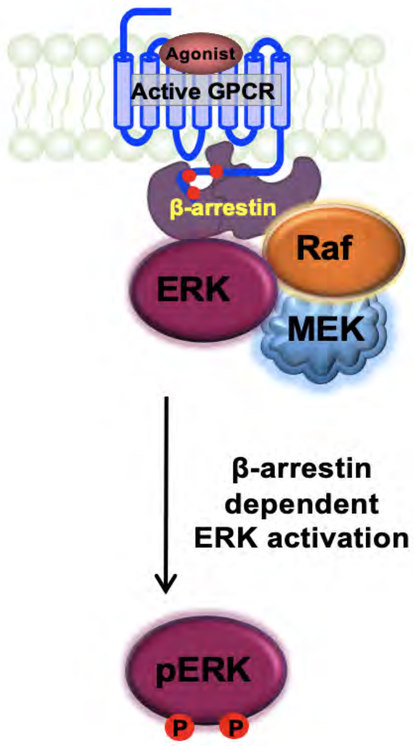

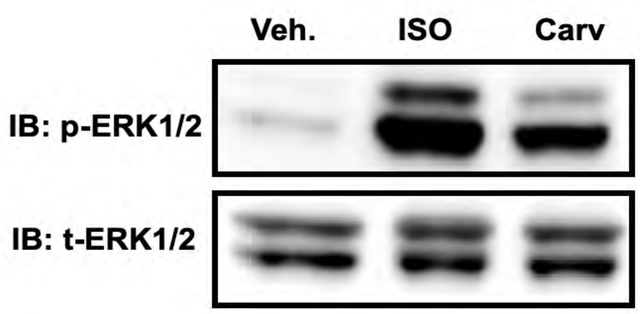

B.

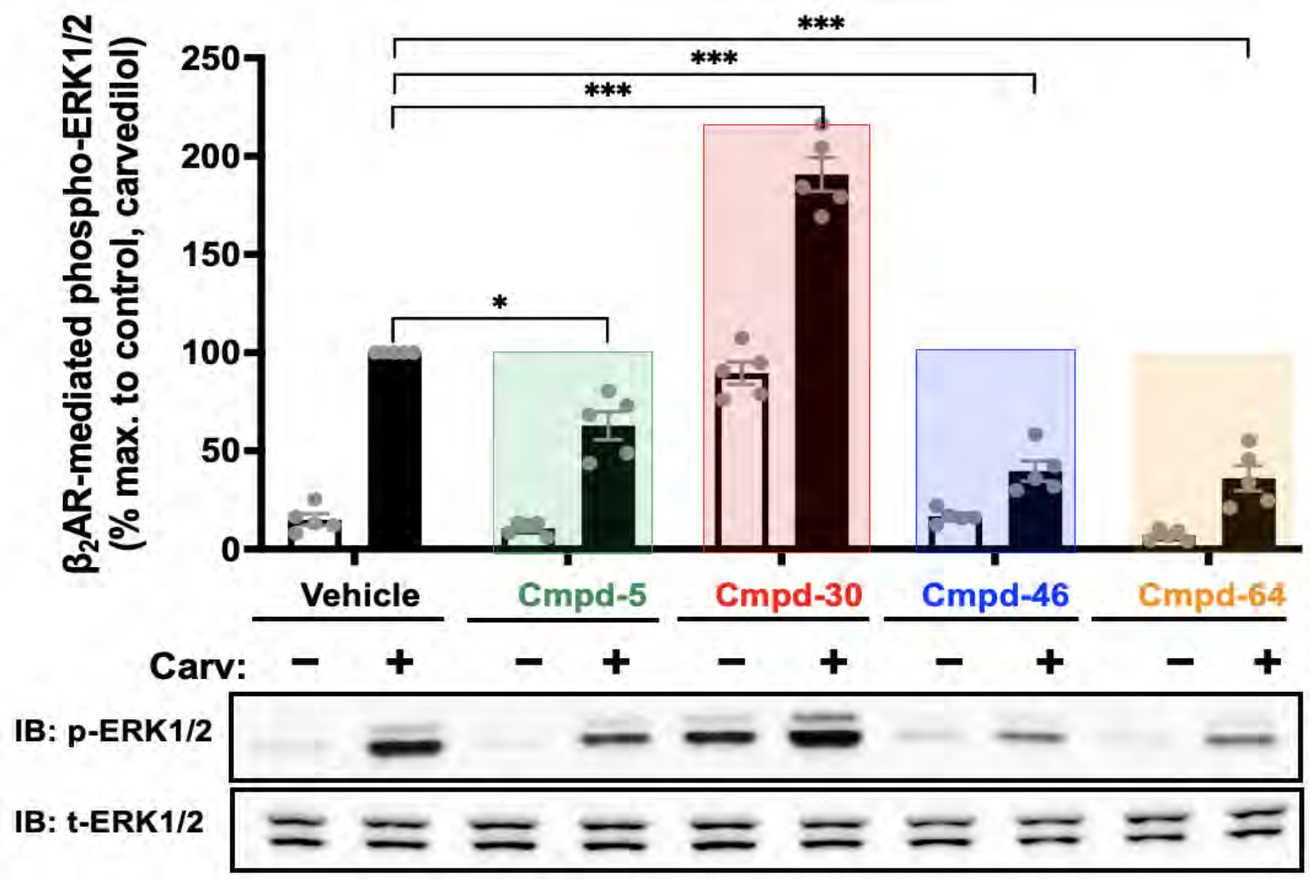

C.

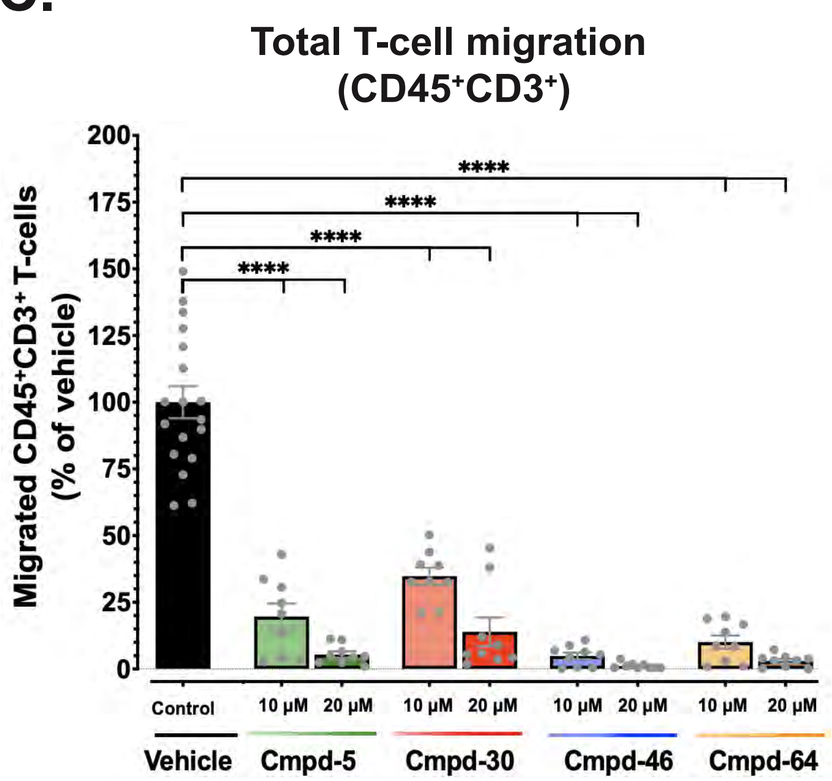

D.

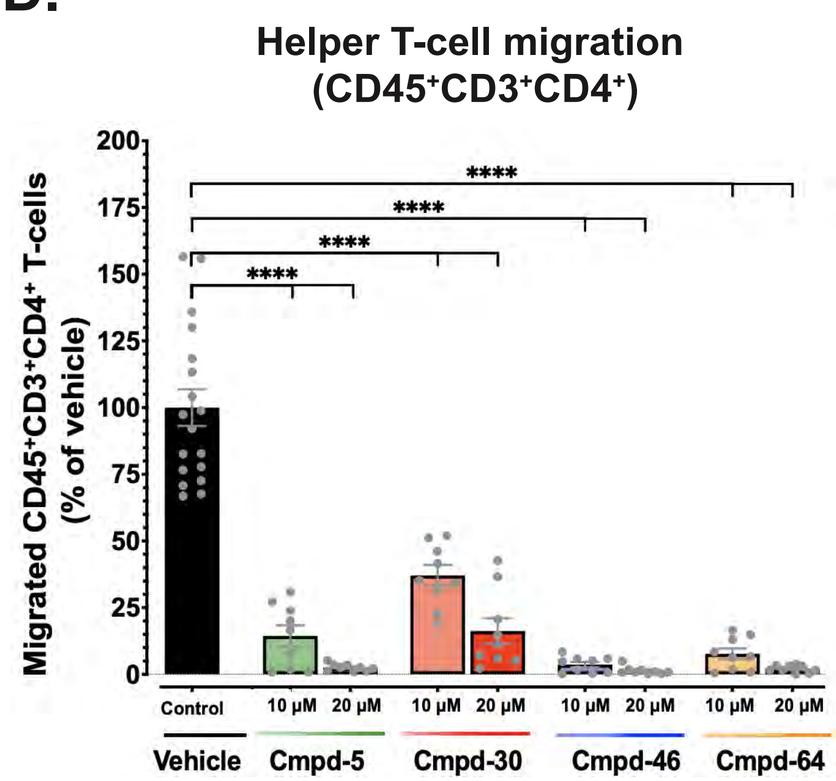

E.

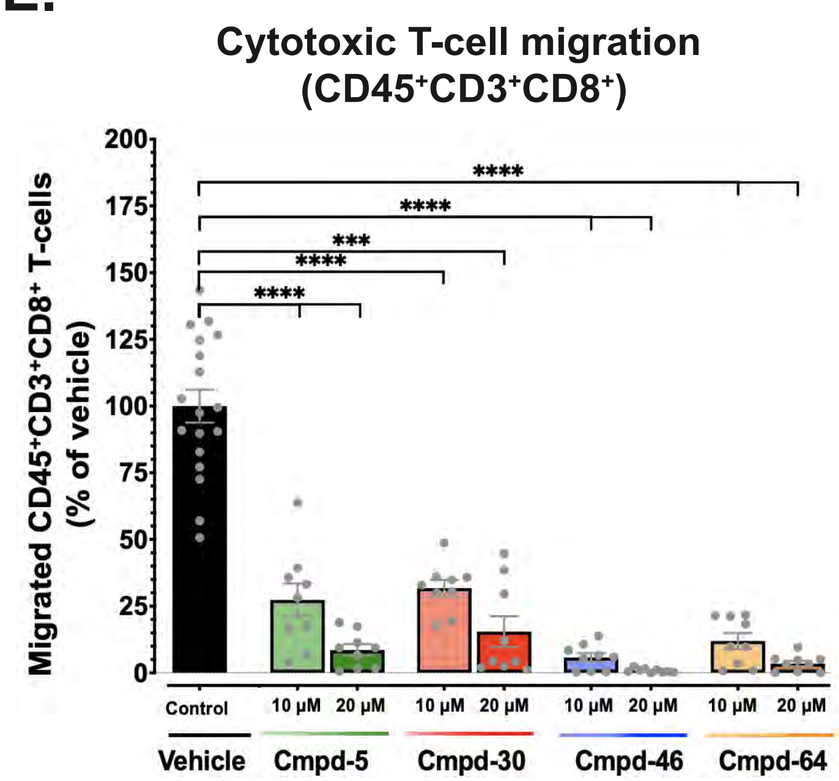

Figure 6

A.

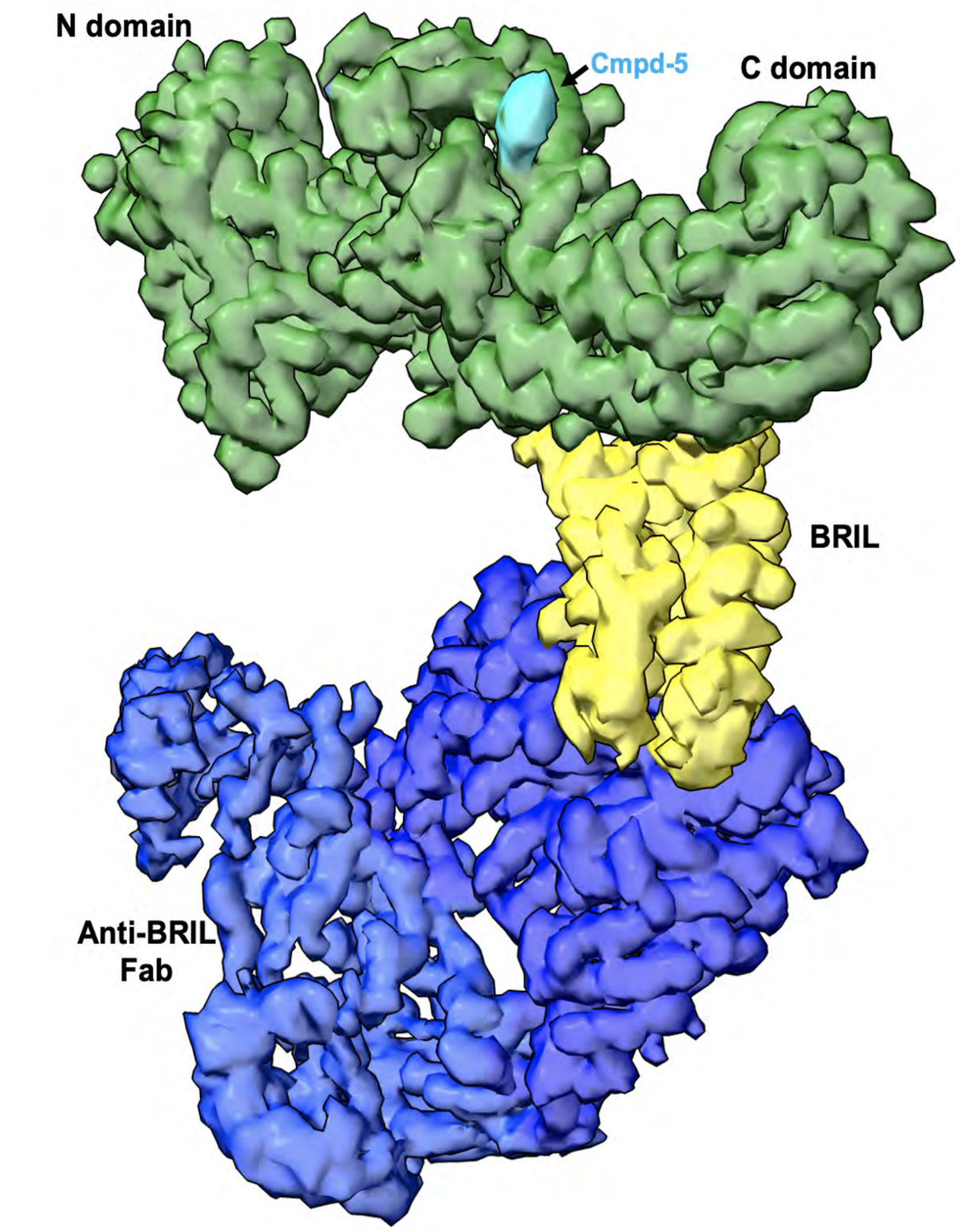

B.

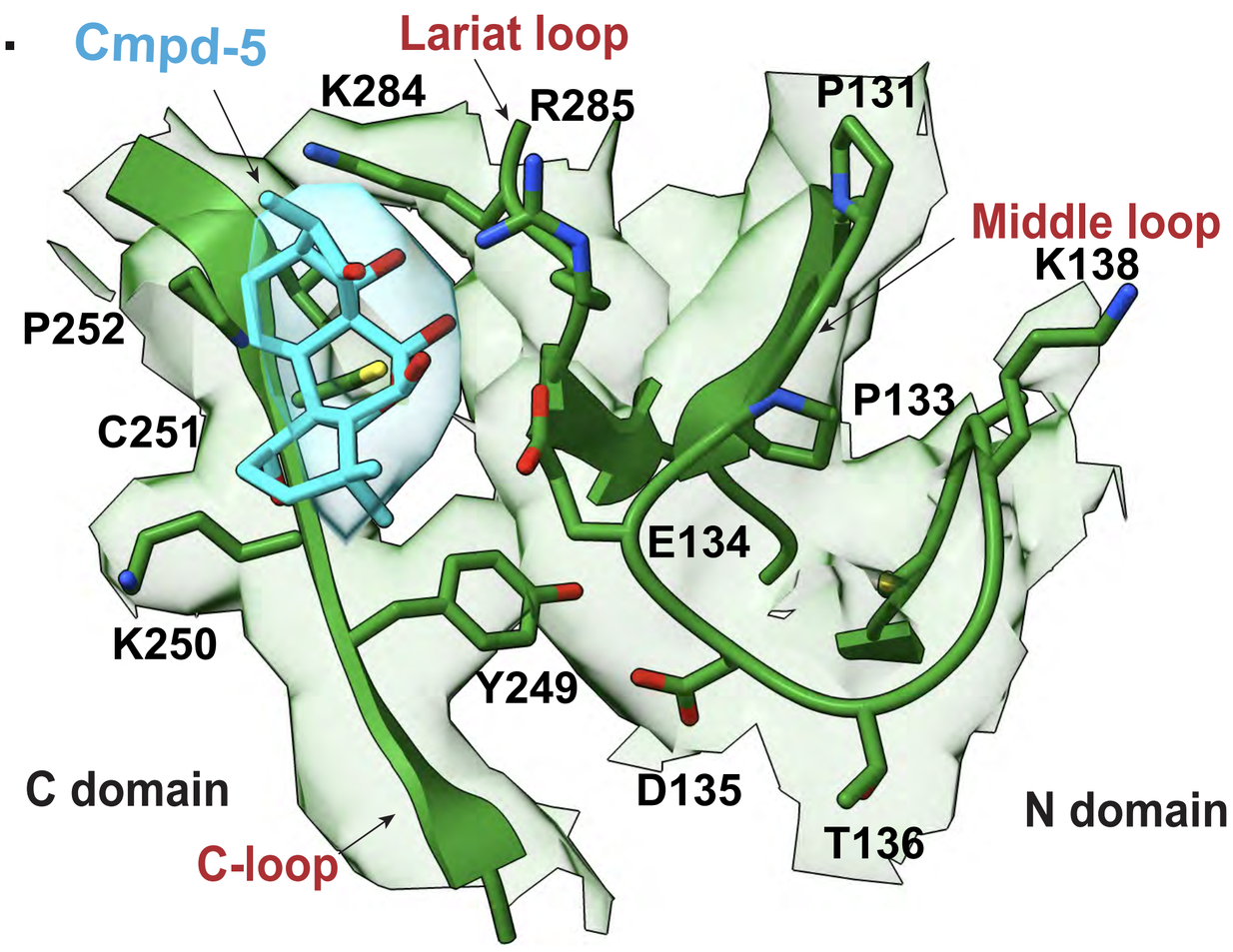

C.

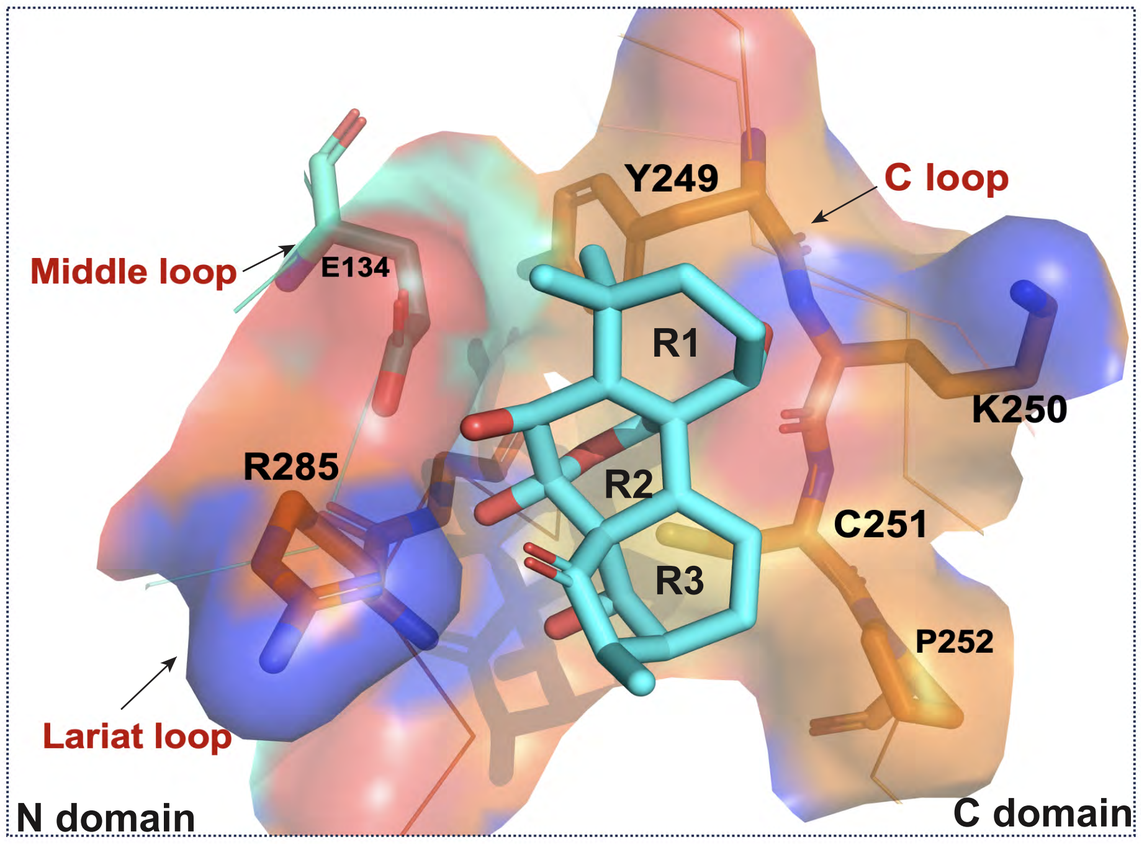

D.

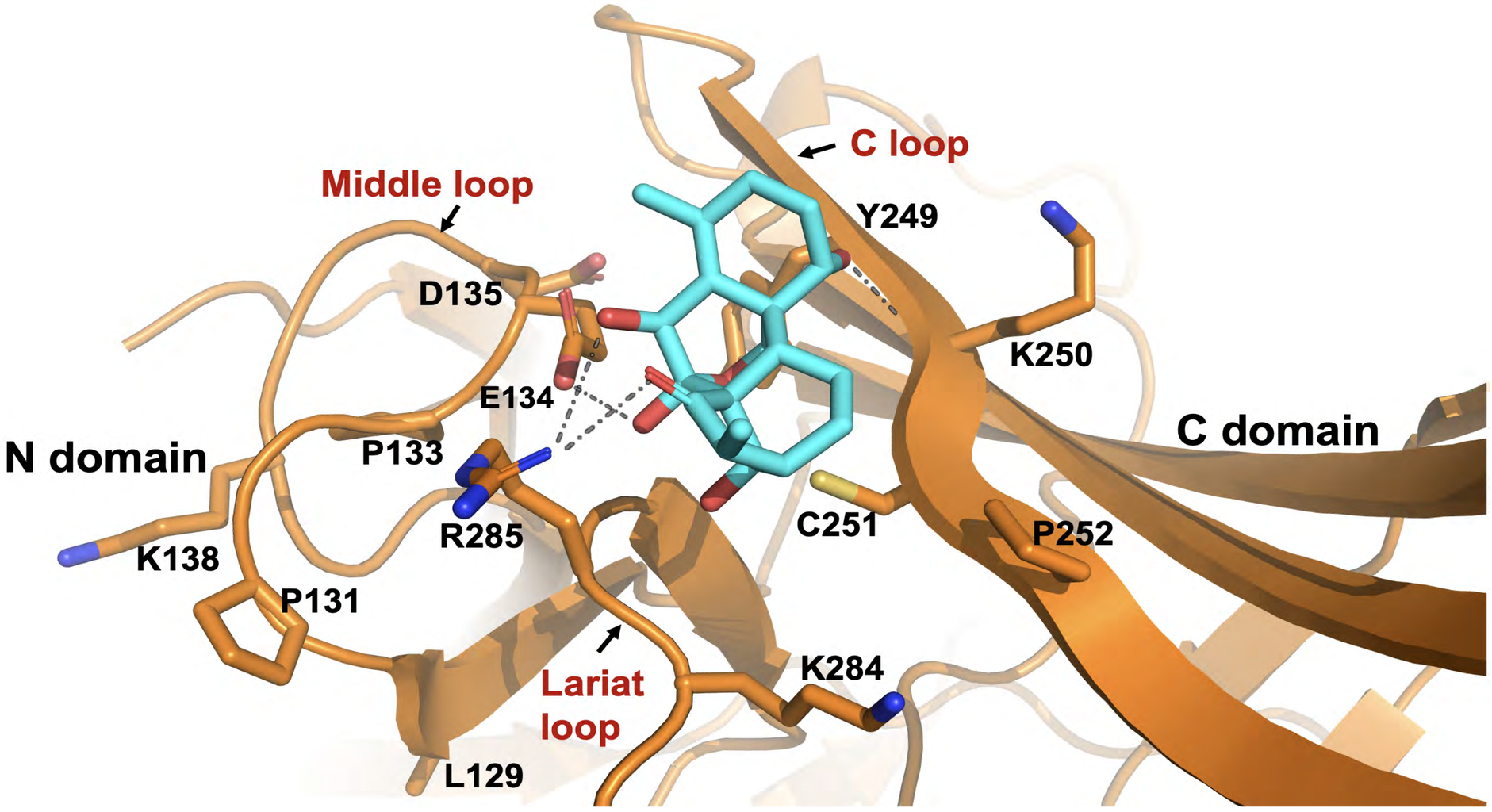

Figure 6

E.

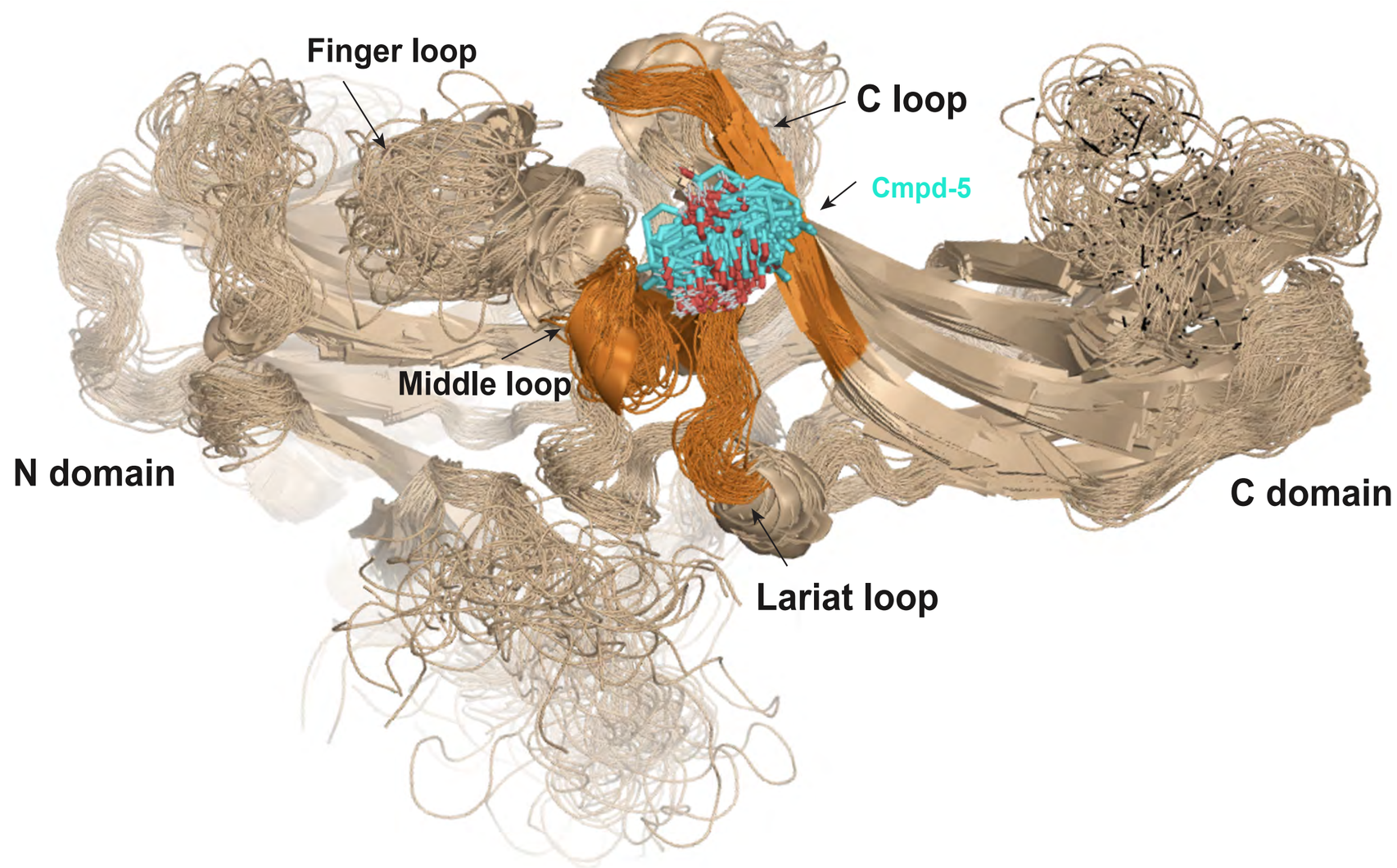

F.

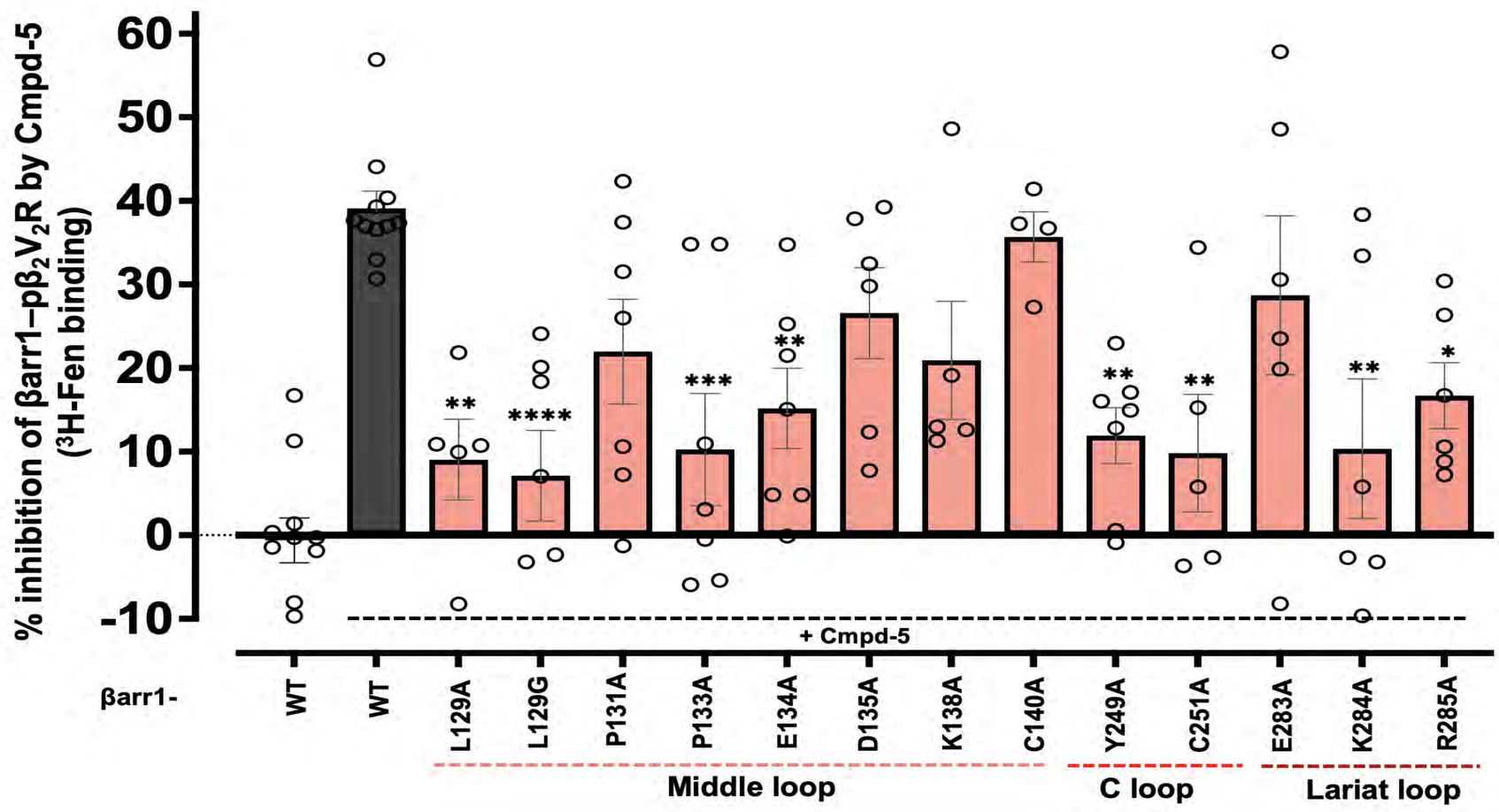

G.

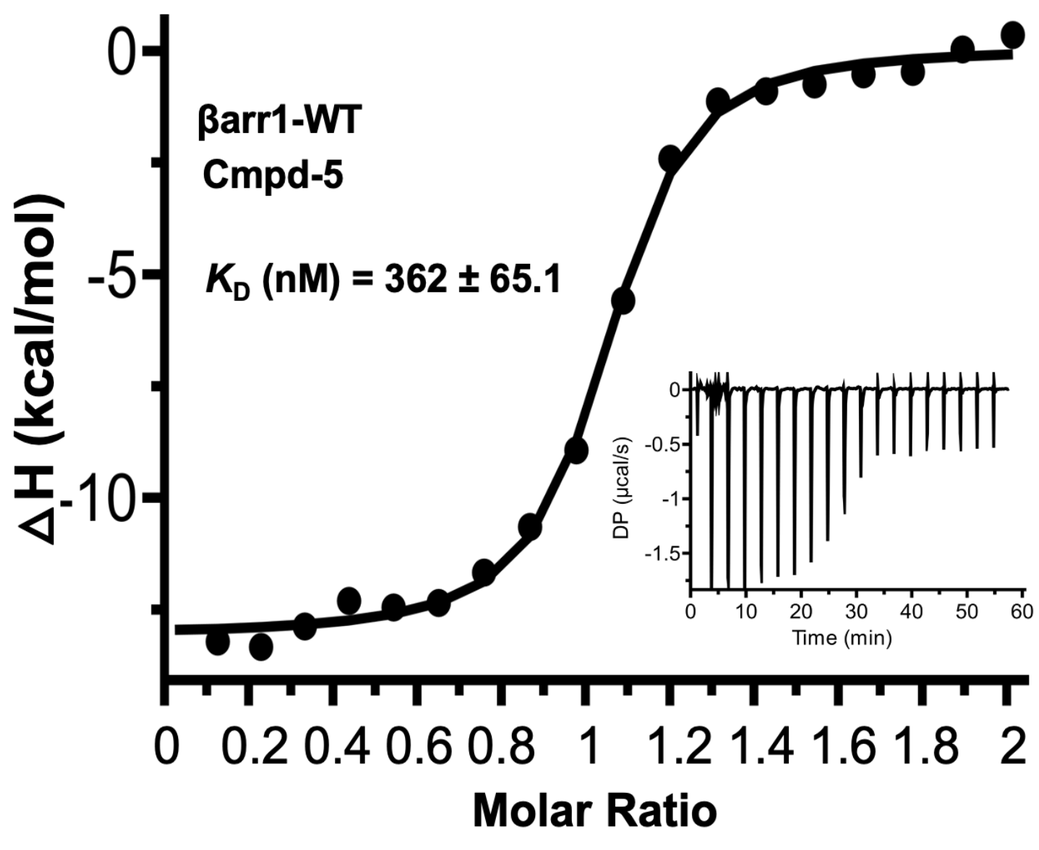

βarr1	K_d (μM)	Fold over WT
WT	0.362 ± 0.065	-
L129G	2 ± 0.7	5.5
P133A	1 ± 0.4	2.8
E134A	2.2 ± 0.5	7.3
K138A	1 ± 0.3	2.7
Y249A	3.8 ± 0.9	10.6
C251A	3 ± 1.0	8.3
R285A	16.8 ± 8	46.5

H.

Figure 7

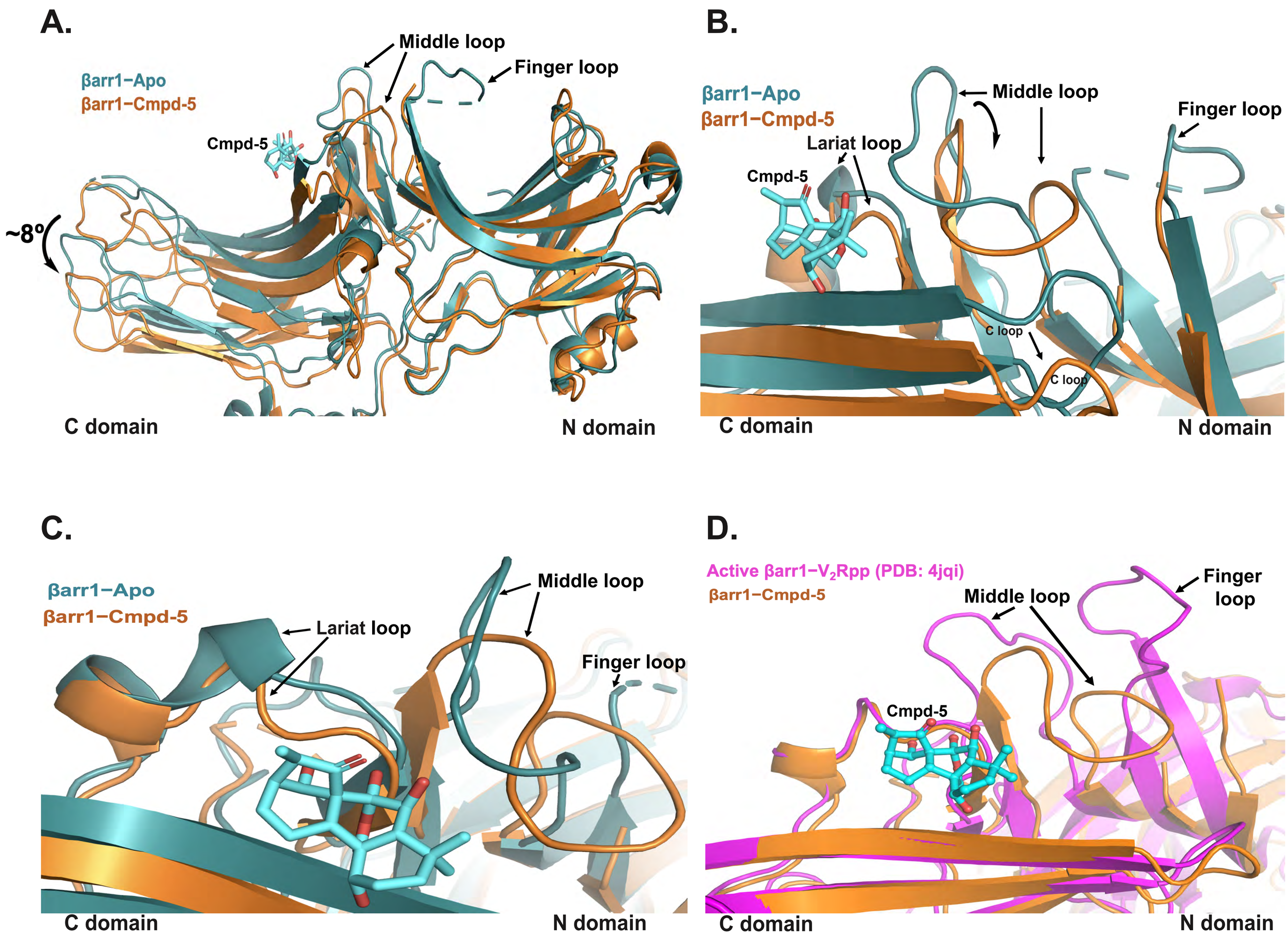
A.
βarr1−Apo
βarr1−Cmpd-5
Middle loop
Finger loop
Cmpd-5
~8º
C domain
N domain
B.
βarr1−Apo
βarr1−Cmpd-5
Middle loop
Finger loop
Lariat loop
Cmpd-5
C loop
C loop
C domain
N domain
C.
βarr1−Apo
βarr1−Cmpd-5
Middle loop
Lariat loop
Finger loop
C domain
N domain
D.
Active βarr1−V2Rpp (PDB: 4jqi)
βarr1−Cmpd-5
Middle loop
Finger loop
Cmpd-5
C domain
N domain